NSEL Report Series
Report No. NSEL-033
January 2014

Smart Wireless Control of Civil Structures

Lauren E. Linderman

and

Billie F. Spencer, Jr.

Department of Civil and Environmental Engineering
University of Illinois at Urbana-Champaign

UILU-ENG-2014-1801

ISSN: 1940-9826

The Newmark Structural Engineering Laboratory (NSEL) of the Department of Civil and Environmental Engineering at the University of Illinois at Urbana-Champaign has a long history of excellence in research and education that has contributed greatly to the state-of-the-art in civil engineering. Completed in 1967 and extended in 1971, the structural testing area of the laboratory has a versatile strong-floor/wall and a three-story clear height that can be used to carry out a wide range of tests of building materials, models, and structural systems. The laboratory is named for Dr. Nathan M. Newmark, an internationally known educator and engineer, who was the Head of the Department of Civil Engineering at the University of Illinois [1956-73] and the Chair of the Digital Computing Laboratory [1947-57]. He developed simple, yet powerful and widely used, methods for analyzing complex structures and assemblages subjected to a variety of static, dynamic, blast, and earthquake loadings. Dr. Newmark received numerous honors and awards for his achievements, including the prestigious National Medal of Science awarded in 1968 by President Lyndon B. Johnson. He was also one of the founding members of the National Academy of Engineering.

Contact:
Prof. B.F. Spencer, Jr.
Director, Newmark Structural Engineering Laboratory
2213 NCEL, MC-250
205 North Mathews Ave.
Urbana, IL 61801
Telephone (217) 333-8630
E-mail: bfs@illinois.edu

This technical report is based on the first author's doctoral dissertation of the same title, which was completed in August 2013. The second author served as the dissertation advisor for this work.

Financial support for this research was provided in part by the National Science Foundation under NSF Grants No. CMS- 0600433, CMMI-0928886, and CNS-1035773. The first author was supported by the National Science Foundation Graduate Fellows Program, Illinois Distinguished Fellowship, and Carver Trust Fellowship. Finally, we would like to thank the numerous collaborators on this work, including Gul Agha, Andrew Alleyne, Daniel Work, Kirill Mechitov, Hongki Jo, Chia-Ming Chang, Robin Kim, and Shirley Dyke.

The cover photographs are used with permission. The Trans-Alaska Pipeline photograph was provided by Terra Galleria Photography (http://www.terragalleria.com/).

ABSTRACT

Structural control techniques are an alternative approach to protect structures from natural hazards that continue to plague our nation's infrastructure. Due to their onboard sensing, communication, and computational capabilities, wireless smart sensors, which have become popular for structural health monitoring applications, are an attractive option for implementing structural control systems. However, wireless smart sensors pose unique challenges, such as communication latency and unreliable communication, which make common centralized control systems over wireless networks less feasible. Previous research has implemented wireless structural control using decentralized approaches on semi-active control systems; however, these implementations are less sensitive to the challenges related to wireless structural control, because semi-active control systems are inherently stable. On the other hand, wireless active control systems require the entire control system, from hardware selection to control design, to deal with these challenges to limit delays and error and to ensure a stable system. Therefore, this research addresses all the elements of wireless active control design to overcome these challenges. Low-latency data acquisition and actuation hardware tailored for control limits any inherent delay due to the sensing and control components. Real-time wireless data acquisition and control strategies are implemented within the existing software framework. The approach for digital control design preserves stability and control performance in the presence of delays and at slow sampling rates. The wireless control system is validated on an actively controlled multi-story, small-scale test structure suitable for different levels of control decentralization. The result of this research is the realization of a decentralized wireless active structural control system that overcomes the challenges posed by wireless smart sensors to realize their potential for structural control.

TABLE OF CONTENTS

Chapter 1

INTRODUCTION

1.1 Motivation

Natural hazards, such as earthquakes and hurricanes, pose a serious risk to a nation's civil infrastructure. Ensuring adequate performance of civil infrastructure, e.g., buildings and bridges, during these events is essential for improving life-safety and limiting the economic costs to society. Limiting structural response to natural hazards, particularly wind and seismic response, has been a long standing goal of building codes and academic research. One approach that is typical of building codes is to limit the response by altering the stiffness or mass distribution in the original structural design. A second approach is to limit the response through an auxiliary structural control technique that can introduce damping or alter the stiffness of the structure.

Structural control offers an appealing approach to protect structures from natural hazards by adding supplemental damping devices. These supplemental damping devices can be divided into four main categories: passive, active, hybrid, and semi-active. While passive devices, which include base-isolation and viscous dampers, have seen widespread use, particularly in California, they lack the ability to adapt to changes in the structure and loading. On the other hand, active, hybrid, and semi-active control techniques use measured responses from the structure to alter the supplemental damping device in real-time. Active techniques, such as active mass drivers (AMD), which are more common in Japan, use the feedback of the response to appropriately input energy into and remove energy from the system to alter the properties of the system and limit the structural response. Semi-active techniques, which have been the recent focus of much research, use feedback to alter the properties of the damping device (i.e., magnetorheological (MR) dampers), which then limits the structural response; thus, no additional energy is input into the system.

Until recently, modern control systems that utilize feedback are based on a centralized control design. In centralized control, sensors distributed throughout the structure are connected to a central controller node. Thus, all the sensor data feeds back to one control point. While these systems can provide good performance due to their knowledge of the complete structural response, they also provide a control system with a single point of failure and can be costly to install. As sensor systems become more densely distributed throughout structures, decentralized control systems, which only use local structural response, have become an attractive approach. By providing multiple localized controllers, they offer robustness to the control system and lower the installation costs with a tradeoff in the ease of design and possible performance.

Sensors distributed throughout a structure are becoming more common due to ongoing research in structural health monitoring (SHM). In SHM, the health of a structure is evaluated after a natural hazard event based on the measured structural response. Changes are detected in the structure using algorithms that use the structural response as input. In traditional wired systems, the structural response is gathered from various sensors back to a central base station. However, these systems, while becoming more common in new structures for SHM, can be expensive to install and operate; because damage is a highly local phenomenon, numerous sensors are needed, thus increasing the cost of the system.

The relatively high cost of wired systems has made wireless sensor systems an appealing alternative for structural health monitoring applications. The advances in wireless technology

decrease the deployment cost by simplifying and limiting the implementation time. This relative ease in implementation and lower cost encourages dense sensor deployments, which is ideal for identifying structural changes. In addition, wireless smart sensors, which combine onboard processing, memory, and sensing with wireless communication on a single node, have leveraged these capabilities to process the data locally to extract important information in a decentralized fashion. Thus, the data sent back to the base station, or user, is limited to reduce the possibility of inundating the network with data and encourage dense deployments.

Due to their onboard sensing and computational capabilities, these wireless smart sensor networks are an attractive option for implementing structural control systems. However, wireless smart sensor networks pose unique challenges for application of structural control. Wireless smart sensors have unique hardware limitations that make the common centralized control approaches used over tethered networks less feasible. Wireless communication introduces communication latency and the possibility of data loss. These challenges can reduce the possible sampling rate and introduce significant time delay and error into the system. Furthermore, the processing time required for handling the large amount of data from a dense network of sensors at a single node can be prohibitive. To limit these factors in the design, decentralized control techniques are used.

Given the proliferation of wireless smart sensors in the research community, decentralized structural control has become an area of interest. Although a large body of work in decentralized control exists, it had not been applied to structural control until recently. Decentralized control offers several advantages to wireless structural control, including limiting the wireless communication required and the associated slow sampling rate and time delays and adding robustness to the control system. However, less knowledge of the system is available at each controller node. Thus, in wireless structural control, a tradeoff exists between system knowledge and limiting hardware-related challenges.

Previous research has explored this tradeoff by implementing wireless structural control using decentralized optimal control approaches on semi-active systems. Wang et al. (2006a) successfully implemented a wireless semi-active control system on a three-story structure. The faster sampling rate of the decentralized control approaches compensated for the reduced information about the structural response available to the controller. Since this initial test, experimental research has focused on semi-active structural control systems using various decentralized control techniques that account for time delay and data loss. However, semi-active control systems are less sensitive to the challenges related to wireless structural control, because they are inherently stable systems.

Active control systems do not guarantee a stable response, as they have the potential to input energy into the structure; thus, they are more sensitive to the hardware-related challenges inherently posed by wireless smart sensors. Modern structural control research has illustrated that practical considerations, such as sampling rate, time delay, and microprocessor speed, need to be considered to ensure performance. However, the previous work in wireless control has not needed to directly address these challenges, because stability is guaranteed for the semi-active systems. Similarly, the only application of wireless structural control to active control systems found in the literature does not present a scalable approach that accounts for the time delays and processing demands as the number of nodes in the network increase. In contrast, effective wireless active structural control requires the entire control system, from the hardware selection to the control design, to be addressed to account for these factors, limit delays and error, and reduce the possibility of instability.

1.2 Overview of Research

The objective of this research is to design, produce, and implement a decentralized wireless active structural control system. In particular, this work will address all the elements of wireless control design including: (1) the hardware and software support, (2) digital control design at slow sampling rates, (3) implementation of decentralized control strategies on the wireless control system, and (4) experimental validation on a small-scale structure appropriate for decentralized approaches. The result of this research will be the realization of a wireless active structural control system that overcomes the challenges posed by wireless smart sensors to realize their potential for structural control.

Chapter 2 provides background on structural control and, in particular, research that seeks to account for and overcome practical challenges such as time-delay, low sampling rates, and sensor failure. Experimental applications of wireless smart sensor networks to semi-active control systems present a promising first-step to addressing these challenges, since they are inherently stable. The limitations in current hardware, software, and wireless control designs that address practical considerations are identified.

Chapter 3 presents technical background relevant to this research that is outside a traditional civil engineering experience. Analog-to-digital converter architectures relevant to this work are outlined and their application limitations are addressed. Modern control theory is presented and both continuous and discrete-time systems are discussed. In addition, the wireless smart sensor platform and software framework used in this research are presented in detail.

Chapter 4 illustrates the limitations of current hardware tailored to SHM and presents low-latency data acquisition and actuation hardware for control applications. The development of a data acquisition board and corresponding software to address these limitations for control operation are outlined in detail. The actuation interface completes the hardware necessary for wireless control. The resulting performance of the hardware highlights the latency improvements and informs the control designs presented in Chapter 7 and Chapter 8.

Chapter 5 presents the framework for wireless data acquisition for real-time state knowledge. The inherent challenges of embedded software and the smart sensor platform, including communication time and the single-threaded operating system, are outlined and addressed in the framework development. The application performance highlights the sampling rate limitations for centralized wireless control. The framework is extended for high-throughput applications, which are less sensitive to delays.

Chapter 6 builds on the framework and insights from Chapter 5 to implement centralized and fully decentralized control strategies on the wireless smart sensor platform fitted with the low-latency hardware. The fully decentralized implementation leverages the on-board processing power to offer very high sampling rate performance while maintaining accurate control calculations. The centralized control implementation maintains an adequate sample rate for control and preserves computational accuracy while limiting data loss.

Chapter 7 presents the control of a small-scale, single-degree-of-freedom structure with an active mass driver using both wired and wireless smart sensor systems. An approach for discrete-time control design at slow sampling rates is used for the smart sensor control designs. The smart sensor control system provides comparable performance to the tethered system, which illustrates the feasibility of wireless active structural control. In addition, the low-latency data acquisition hardware is experimentally validated and outperforms the previous hardware tailored for SHM applications.

Chapter 8 compares wired, fully decentralized wireless, and centralized wireless control systems on a four-story structure fitted with two active mass drivers for control. A high fidelity model of the multi-input multi-output system is used for the control designs. The control design approaches for all three systems are presented in detail. The sampling rate performance of the wireless control implementations in Chapter 6 guide the fully decentralized and centralized control designs. The experimental control performance is evaluated in both the frequency and time domain using band-limited white-noise and earthquake ground motions applied at the base of the structure. In addition, the robustness of the fully decentralized control system is assessed by forcing node failures during closed-loop control of the structure when subjected to earthquake ground motions.

Chapter 9 summarizes the research presented in this dissertation and discusses future research directions in regard to decentralized control designs and wireless smart sensors for structural control.

LITERATURE REVIEW

This chapter presents a review of structural control and the necessary practical considerations, the requirements of wireless structural control, including the hardware, decentralized control schemes, and embedded software, and experimental wireless control applications.

2.1 Structural Control

The strength of civil infrastructure used to be the predominant focus of structural design; however, the dynamic response due to wind and earthquakes has become a significant concern due to tighter serviceability and life-safety requirements. To limit vibration response, control concepts common in mechanical systems were proposed for civil systems by Yao (1972). Structural control limits the vibration response due to wind and earthquakes by altering the stiffness, mass, damping, or including counter forces. Civil infrastructure systems pose unique challenges, such as requiring large control forces, limited measurements, and uncertainty in loading; and thus, structural control has become its own area of research (Housner et al. 1997).

Typically, these control systems are broken into two main categories: (1) passive control systems, (2) active, hybrid, and semi-active control. Passive control systems impart forces to alter the stiffness or damping of the system based on the structure's own motion; and therefore, do not require an external energy source (Housner et al. 1997). In the latter category, forces are applied to the structure based on sensor measurements and real-time processing and usually require an external energy source (Chu et al. 2005). This research will focus on the second category of control systems, because they offer adaptability and can be effective over a broader frequency range (Soong 1990).

Active, hybrid, and semi-active structural control systems consist of three main components: sensors, control computers, and control actuators. A generic control system is illustrated in Figure 2.1. The combination of the excitation, structure, and response elements at the bottom of the schematic are often referred to as the open-loop response, as it represents the system without any control. On the other hand, the inclusion of the control in the system response is referred to as closed-loop control. Within the control system, sensors are used to either measure the excitation, the structural response, or both; the controller calculates the appropriate forces based on the measurements; and, the actuators apply the desired forces to the system.

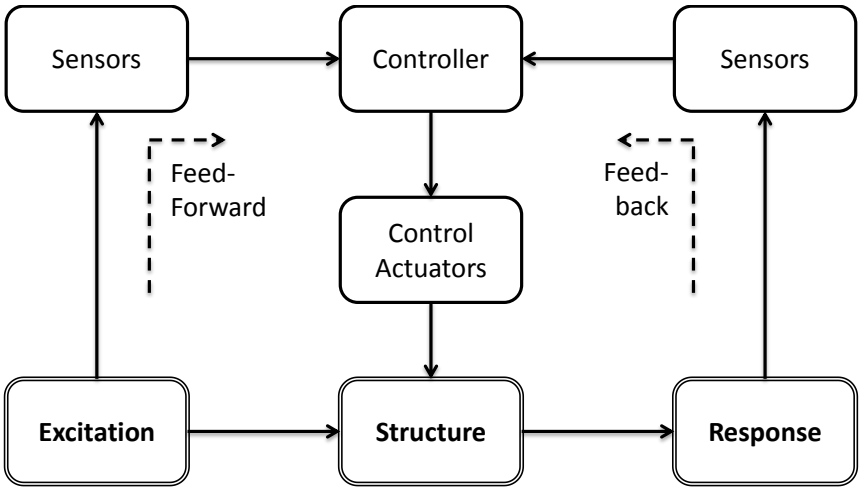

Figure 2.1: Generic Control Schematic (Spencer and Sain 1997).

The control systems are categorized based on how the measurements are included in the control calculations. . When measurements of the response are used in the controller, the system is referred to as feedback control. The response is continually fed back to the controller to alter the control force applied to the system. On the other hand, a feedforward control system uses measurements of the excitation in the control calculations. Because feedback systems compare the actual response to the desired, they are able to operate under disturbances to the system and variations in the plant (Kwakernaak and Sivan 1972).

The approach used to achieve the desired control action differentiates between the types of control: active, semi-active, and hybrid. Active control systems use externally powered actuators placed strategically throughout the structure to apply the desired forces. The forces can add to as well as dissipate energy in the system (Housner et al. 1997). Some examples include active mass driver and tendon systems. In hybrid systems, an active system is used in combination with a passive control device to achieve the control goals. Because these systems use passive devices to achieve a portion of the control effort, they can be more efficient than purely active systems and offer some protection if the external power source required for active control fails (Chu et al. 2005). One example of hybrid control is an active base isolation system, in which actuators are used to limit the displacements of the base isolated structure. Semi-active control systems achieve their control effort through a passive energy dissipation device in which the properties of the device are changed in real-time; they are often referred to as controllable passive devices (Housner et al. 1997). As a result, only a limited external power supply is required. Some common examples of semi-active systems are magnetorheological (MR) and variable orifice dampers. The categorization of how the control forces are applied to the structure has implications on the efficiency of the system and power requirements.

In addition, the difference between active and semi-active systems has significant implications on the design requirements. Semi-active systems do not have the potential to add mechanical energy to the system like active systems. Therefore, because civil systems are typically inherently stable, bounded-input-bounded-output stability holds (Housner et al. 1997). On the other hand, stability is not guaranteed in active systems; thus, particular attention must be paid to practical considerations in control design, such as time delay, modeling errors, etc.

Numerous reviews of the structural control literature have been published, providing overviews of the control categories discussed in this section, as well as the technologies/devices used, control algorithms, industry implementations, and experimental testing. Soong (1990)

discusses the early experimental studies of active control and the practical considerations in design. Housner et al. (1997) provides a thorough review of the devices developed for passive and semi-active control as well as the control algorithms used in active control. Spencer and Sain (1997) and Spencer and Nagarajaiah (2003) focus on the developments of semi-active control strategies. In addition, they both provide a summary list of the controlled buildings and towers, in which a majority are in Japan and use a hybrid mass damper. Given the existing literature reviews, this section will focus on the practical challenges in active control and related active control experiments.

2.1.1 Practical Considerations in Active Control

Within the components of the active closed-loop control system, several hardware elements can impact the control implementation. These large-scale structural systems need to be reasonably modeled for the control design. In addition, the location, type of sensors and actuators, and the associated delays need to be considered. Furthermore, as pictured in Figure 2.2, a digital control system is usually used for the controller computer, and as such the performance of the relative components needs to be considered. These components can impact the resolution of the data, accuracy of the control calculations, and sampling rate of the controller system. Thus, several common practical issues must be considered, including: modeling errors, time delay, sampling rate, limited number of sensors and controllers, and quantization issues (Chu et al. 2005).

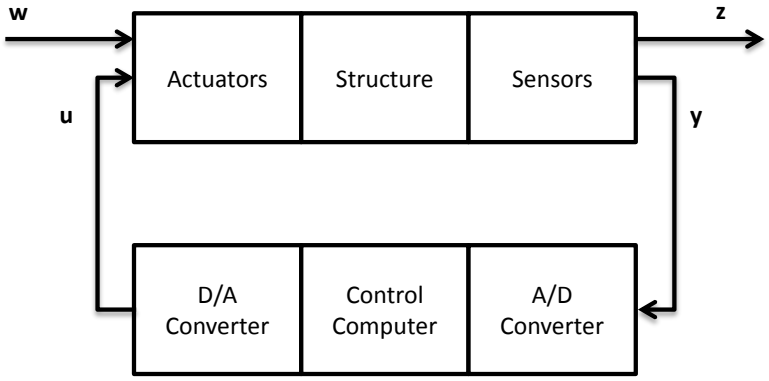

Figure 2.2: Schematic of Active Control Problem (Housner et al. 1997).

Civil engineering systems are typically large, distributed parameter systems, for which a reduced, finite-order model must be developed for control design. Significant research into modeling for control system design can be found in the literature (Soong 1990; Housner et al. 1997). One key contribution to the modeling of systems for control was by Dyke et al. (1995). Dyke et al. (1995) highlighted the importance of considering the control actuators directly in the model of the system, because control-structure interaction can significantly impact the performance of the resulting control design. If significant dynamics are neglected in the modeling of the system, unexpected performance of the closed-loop control, including destabilization, may result.

Because digital control systems are used for active control calculations, the sample period, T, must also be considered. In general, the performance of the control system improves with faster sampling rates; however, a tradeoff is usually found between the time allowed for computation, cost of the digital system, and the performance of the digital controller (Franklin et al. 1998). For approximation of the discrete control system as continuous, the sample rate should be about thirty to fifty times the highest mode of interest, or bandwidth of the system (Hirata and

Powell 1990; Franklin et al. 1998). Otherwise, the discrete sample time should be considered in the modeling, because lower sampling rates can lead to poor disturbance rejection and challenges in control (Hirata and Powell 1990). An absolute minimum is to sample at a rate which is at least twice the system bandwidth to avoid aliasing of the higher dynamics, which could result in an unstable closed loop response (Franklin et al. 1998; Chu et al. 2005). In addition, a slow sampling period due to computation may result in a large time delay between the measurement time and the control application, which may result in poorer control performance.

Time delays and lags due to sensor delays, processing time, or actuator dynamics may lead to instability and poorer control performance when not accounted for in the controller design. Chu et al. (2002) illustrate that a system fitted with an AMD is sensitive to time delays and that, by accounting for the delay, the system can achieve the same performance as a system with no delay. Various time delay approaches are used both within continuous time and discrete time systems that offer varying degrees of robustness to delay. Agrawal and Yang (2000) compare continuous time compensation techniques on an active tendon control system including: the recursive response method, the state-augmented compensation method, the controllability based stabilization method, the Smith predictor method, and the Padé approximation method. The Padé approximation compensation approach developed by Sain et al. (1995) offered stability and good performance under long time delays. In discrete time, the most common approaches involve state augmentation, where an additional delayed state is used in the model; within this augmentation approach, different techniques are used to solve for the controller based on the augmented state model (Chung et al. 1995; Franklin et al. 1998; Chu et al. 2002). Thus, the destabilizing effect of time delay can be overcome with appropriate compensation techniques.

Due to cost and the scale of civil systems, often the number of sensors and controllers available will be limited. The minimum number of sensors required is restricted by the number of modes that are to be controlled (Soong 1990). However, as sensors systems have become cheaper, the availability and scale of sensor networks has increased. The implications of these large sensor networks and large-scale civil systems will be addressed in the discussion of decentralized control in the next section.

Within these sensors, the analog-to-digital converter (ADC) hardware used for representing the analog measurement of the response can lead to error and noise. Quantization is used to divide the amplitude of a signal into discrete ranges. If the signal is very low amplitude in comparison to the voltage range of the sensor input, the variation of the signal may not be appropriately captured. This phenomenon is called quantization error and can lead to poor control feedback (Dyke et al. 1996). As the cost of high-resolution hardware has decreased, the effects of quantization error have been limited; however, when addressing the ADC selection of a wireless sensor board, the resolution should be considered.

2.1.2 Active Control Experiments to Examine Practical Considerations

To highlight and overcome the practical challenges discussed previously, two benchmark problems were proposed for analytical analysis of structural control algorithms based on an experimental setup. These benchmark problems allowed investigators to address issues with measurement availability, sensor resolution, delay, and modeling, including model-order and control structure interaction (Spencer et al. 1998a). The first benchmark is an evaluation model of a three-story building fitted with an AMD at the top story and more detail can be found in Spencer et al. (1998a). The second benchmark is based on an experimental setup of a three-story structure fitted with an active tendon system on the first story (Spencer et al. 1998b). These two

benchmark problems emphasize the significance of including various practical considerations when evaluating control performance.

One other consideration addressed in the benchmark problems is the measurements used for feedback, because often only acceleration measurements are available; therefore, another area of research has compared the performance of control algorithms given the feedback used and weighted in the controller. Many of the time delay compensation algorithms or analytical studies assume full-state or static output feedback, which is often not available (Chung et al. 1995; Agrawal and Yang 200). Dyke et al. (1996) investigates the performance of acceleration feedback on a three-story structure fitted with an AMD. The results indicate that acceleration feedback can achieve good control performance in all three modes of the system. The comparison between different feedback measurements and weightings are still often addressed in the literature both for wired and wireless control, as will be shown in the following sections.

2.2 Decentralized Control

The structural control studies discussed previously usually assume centrality, in which all the information from the system and the related calculations occur at a single location; however, as systems increase in size, either in dimensionality or physical scale, this assumption of centrality often fails due to constraints on the information flow to a single node or the existence of multiple communication and control locations (Sandell et al. 1978; Lunze 1992). Furthermore, in these large-scale systems, the economics of scale and reliability of the communication links often encourages a decentralized scheme (Sandell et al. 1978).

Decentralized control methods are not a new area of research in control; however, its application to civil systems is more recent. Sandell et al. (1978) survey techniques for decentralized control systems, including model descriptions, procedures for testing stability, and decentralized control schemes. Some examples of large systems in other fields include power networks, manufacturing networks, digital communication networks, and economic systems (Sandell et al. 1978).

The control approaches for large-scale systems can be separated into two types: decentralized and distributed. Decentralized control applies to the information structure used for making decisions within the control algorithm (Lunze 1992). Thus, although the information structure is decentralized, the control algorithm can be designed in a centralized way. The degree to which the decision units are independent is the measure of decentralization in the decision process. In distributed control, the control problem is reformulated as a set of interdependent sub-problems, which is often informed by the internal structure of the system to be controlled (Lunze 1992). A common example of distributed control is a hierarchical structure or multilevel system. Often these two types (decentralized and distributed) are lumped into the concept of decentralized control.

In decentralized control, two main information structures are considered: totally decentralized and partially decentralized. The level of decentralization corresponds to the amount of access the controller has to the global information. In totally decentralized, as shown in Figure 2.3(a), only local knowledge is available to the controller. The impact of the control effort on the global response of the system in not known. On the other hand, in partially decentralized (Figure 2.3(b)), some sharing of local knowledge between the controllers is considered. Therefore, some information about the global response is available. However, the level of information sharing is well below that of centralized control, in which complete knowledge of the system is available to the controller.

In distributed control, the most common structure is hierarchical control. Often this structure is considered as a third information structure in decentralized control (Lynch and Law 2002a). An additional layer of controllers, or supervisors, is above the local controllers as seen in Figure 2.3(c); thus, hierarchical control is commonly also referred to as multilayer control (Sandell et al 1978). The goal of the higher level of controllers is to maintain concordant behavior among the local controllers to achieve the desired global response of the system.

2.2.1 Decentralized Control for Civil Structures

Although decentralized control algorithms have been studied for a number of years, the extension of these algorithms to civil structures is more recent. Typically these algorithms are an extension of the popular H_∞ or H_2/LQG optimal control algorithms used for structural control. As Sandell et al. (1978) pointed out, often the decentralized information structure is enforced in a heuristic or ad-hoc manner to a controller designed in a centralized way.

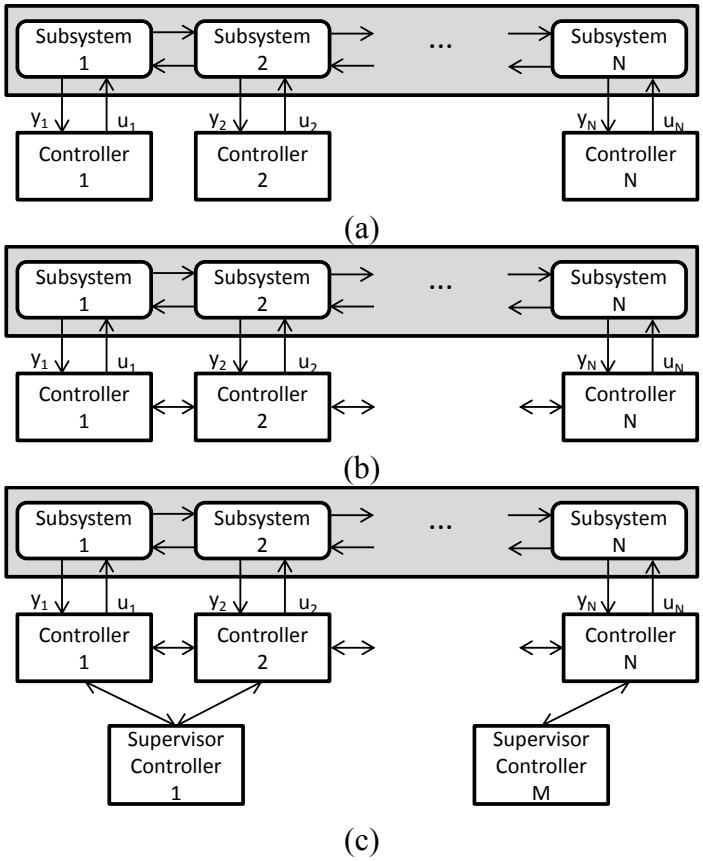

Figure 2.3: (a) Completely Decentralized, (b) Partially Decentralized, (c) Hierarchically Decentralized Information Structures (Lynch and Law 2002a).

The linear quadratic regulator (LQR) design assumes full state feedback, and thus represents a centralized control design. However, in systems where the actuators and sensors are collocated, the diagonal terms typically dominate the resulting gain matrix (Lynch and Law 2002a). Therefore, the information structure is naturally decentralized. The off-diagonal terms can be zeroed based on the desired information structure in a more ad-hoc manner. The resulting controller will be sub-optimal but will closely approximate the optimal design. As the off-

diagonal terms increase, this approximation will deteriorate. Lynch and Law's (2002a) application to the twenty-story benchmark problem (Spencer et al. 1999) reflects the good but sub-optimal performance of the decentralized extension of the LQR solution; the decentralized extension results in irregular behavior between stories. Thus, the off-diagonal terms, although small, contribute to the reduction of the response.

On the other hand, Lunze (1992) presents a heuristic approach to optimal decentralized LQR control. In this approach, an information structure is enforced when solving for the controller gain. Therefore, the controller gain matrix has the desired decentralized structure. An iterative search procedure, which ensures closed-loop stability and an improving solution, is used to solve the optimal control problem. Lynch and Law (2002a) applied this optimal decentralized control solution to the twenty-story benchmark and achieve comparable performance to the centralized LQR controller. The centralized control performs slightly better due to the information sharing about the complete state of the system, but the optimal decentralized controller performs better than the ad-hoc decentralized extension previously discussed.

While the optimal LQR decentralized control solution is attractive for civil systems, the algorithm does not account for the time delay common in wireless structural control. Wang et al. (2007a) combine the approaches of Chung et al. (1995) and Lunze (1992) to create an optimal discrete decentralized control solution that considers time delay. The control design uses an augmented system that accounts for time delay within Lunze's (1992) heuristic optimal decentralized control approach, where the decentralized architecture is enforced on the gain matrix. They investigate the design of both fully and partially decentralized control solutions for a three-story experimental test structure. However, one limitation of the design algorithm is that it is highly dependent on the initial gain matrix and search step size.

Similarly, Wang et al. (2009) extend the optimal H_∞ control algorithm to decentralized architectures, both completely and partially decentralized, using linear matrix inequalities (LMI). Again, the decentralized control design is heuristic, because it enforces an information structure on the gain matrix. They analytically investigate both fully and partially decentralized control structures on three-story and twenty-story structures. As expected, the decentralized LQR control architecture is better at minimizing the H_2-norm and it reduces the response with less control effort than the decentralized H_∞ control designs. In general, however, the partially and centralized control designs outperform the fully decentralized designs when the sampling rate is held constant. For the twenty-story structure, Wang et al. (2009) start to address decentralized algorithms for wireless structural control by considering different sampling rates and communication channels for the control subsystems. Although the sampling rates are not based on any specific wireless smart sensor platform, they find a tradeoff between the degree of decentralization, sampling rate, and performance.

The decentralized H_∞ algorithm is another attractive option for wireless structural control of civil systems; however, the algorithm does not account for time delay, which is common with this type of hardware setup. Wang (2011) extends the algorithm to account for this limitation by including time delay in the system model; the algorithm then can be applied to varying decentralized architectures through homotopic transformation. The decentralized control designs are heuristic, because the decentralized structures are enforced on the gain matrix as well as LMI constraints at each iteration step. The algorithm is applied analytically to a five-story model similar to the Kajima-Shizuoka Building (Kurata et al. 1999). For different decentralization structures, the time delay is increased based on the amount of information required for each controller, as might happen in a wireless system; however, no specific wireless smart sensor

hardware is used as a basis for the time delays used in the analysis and the corresponding sampling rate variations are not considered. Due to the longer time delays required for more information feedback, the structures with more information feedback can actually lead to poorer performance. Thus, despite less global information, lower requirements on the communication network (or smaller time delays) can be preferable for implementation. Furthermore, when compared to time-delayed decentralized controllers based on LQR optimization, the H_∞ approach is better at reducing maximum responses, while the LQR (H_2-norm) approach reduces the root-mean-square (RMS) response with less control effort, as expected.

Unlike previous decentralized optimal control algorithms, an algorithm extended to civil systems by Ma et al. (2008) does not ensure global and local stability through an iterative approach, but rather the control signal is calculated using a linear feedback component, which ensures local stability, and a nonlinear feedback component, which guarantees global stability in the face of uncertainties. The structure is broken up into artificially independent subsystems and the interactions among the subsystems are treated as unknown disturbances to the individual systems. The algorithm, originally developed for decentralized robotic control, which is based on sliding mode control, is extended to building systems, and the conditions for guaranteeing stability and ensuring good performance are outlined. The algorithm is analytically applied to linear and nonlinear shear-type building structures. When compared to decentralized and centralized LQR control designs, the control algorithm is found to offer at most comparable performance; but, the algorithm is significantly more robust to actuator failure than the centralized design and capable of limiting the structural response in the presence of major modeling uncertainties. While these results are promising, the analysis does not account for practical considerations of sensing and actuator dynamics.

Algorithms based on control of systems that are naturally decentralized have been extended to structural systems and compared with classic centralized control techniques. Market based control (MBC), initially used in microelectromechanical (MEMs) systems and computer architectures, mimics the free markets, in which control power is the scarce system resource that is optimally distributed similar to goods and services (Lynch and Law 2002b). The idea is that the free market is naturally decentralized and can perform as well or better than a centrally controlled system. Lynch and Law (2004) extend MBC to a more rational formulation based on the energy balance of the system called energy market-based control (EMBC). The market demand and supply functions of the buyers and sellers are based on the dynamic energy of the structural system in addition to the wealth considerations of the buyers and sellers. In both cases, stability of the systems is not guaranteed, however, because semi-active control actuators are used, bounded-input, bounded-output stability can be assumed. When analytically applied to the five-story Kajima-Shizuoka building and the twenty-story SAC building fitted with semi-active hydraulic dampers, the MBC-based formulations achieve the same performance as centralized LQR designs with the same or additional accumulated control force. This algorithm could be expanded to include other costs, such as wireless communication, and should also consider other practical considerations such as computational requirements, time delays, and effects of actuator failure, plant changes, or failures in the monitoring system.

Other non-classical control approaches, including multi-layer neural networks, have gained attention for system identification and control due to their ease of decentralization. Xu et al. (2003) numerically investigated neural networks for the decentralized control of a cable-stayed bridge. The cable-stayed bridge uses active tendons to provide control forces through actuators. Each actuator is controlled by a neurocontroller that uses only local state information.

The controller, which is trained on a decentralized system identification, achieves good performance for both its trained input and other earthquake excitations. However, the control design is less successful when the original structure used for training is altered. The authors recommend online training to counteract this limitation. Given these active control results, decentralized neurocontrol may be an attractive option for large-scale active structural control applications; however, the impact of practical considerations on the performance, such as sampling rate, measurement availability, and actuator performance is not addressed in the simulation.

The previous decentralized control techniques assume full-state feedback; however, typically only limited measurements are available to the controller and estimation must be used within the decentralized control framework. Loh and Chang (2008) investigate several decentralized Linear Quadratic Gaussian (LQG) control algorithms utilizing acceleration measurement feedback. Three general types of decentralization are considered: half centralized, fully decentralized, and partially decentralized subsystems are considered, in which the control gain for each subsystem is designed separately and the corresponding measurement structures are used for the design of the Kalman filter. Within partially decentralized control, different coupling structures are considered based on the degree of coupling among the subsystems. The controllers are analytically investigated on the twenty-story SAC II building; and, the decentralized controllers are found to have comparable performance to the centralized control system but are more robust to control system failure. In addition, an acceleration threshold system, in which two decentralized control systems are used alternately depending on the acceleration level, is successful at limiting the system response. The threshold system illustrates that a different control system can be used in parallel in case communication failure occurs among the controllers.

Similarly, Lei et al. (2012) divide the system into smaller substructures each controlled by its own local LQG control scheme using acceleration feedback; however, in this work, the interconnections between the adjacent subsystems are treated as disturbances. These unknown disturbances are estimated using a recursive technique. When measurements of the unknown disturbances are unavailable, the states are shared among neighboring substructures for estimating the disturbances; thus, the system approaches partially decentralized rather than a fully decentralized architecture. When measurements of the disturbances are available, the full disturbance influence can be estimated locally; thus, the subsystem controllers are fully decentralized. The two cases achieved comparable performance analytically to the centralized LQG control of the twenty-story SAC building. Similar to other analytical studies, practical considerations relating to sensor and actuator dynamics were not included in this work.

Using a novel redundant Kalman estimation technique, Seth et al. (2005) more directly address the concerns associated with wirelessly networked distributed control. The authors hope to limit wireless communication by locally estimating the full state of the system. The local state estimates are compared to what is measured, and when this differs by more than a specified error tolerance, the measurements of the system are transmitted wirelessly to neighboring controllers. As the error tolerance is lowered, the system approaches a centralized controller. When analyzing the partially decentralized control system, they consider the error threshold that should be used to balance communication performance and system performance. All control designs analytically implemented on the Kajima-Shizuoka building improve performance when compared to no control. Although the system does directly consider issues related to wireless

smart sensors, including the probability of data loss and time delay, the analysis does not consider a varied sampling rate based on the communication required.

2.2.2 Hierarchical Control for Non-Civil Systems

Although completely decentralized and partially decentralized control systems have been implemented on civil systems, hierarchically decentralized control systems have yet to be implemented for structural control. On the other hand, hierarchical control has been successfully applied in robotic, automotive, industrial, and MEMs systems (Sandell 1978; Antsaklis and Passino 1993; Guenther et al. 1997). In these applications, the authors typically find that hierarchical control is a good compromise between local response with simple architectures and the inclusion of global knowledge for better global performance.

In robotic and automotive systems, hierarchical control structures are often considered as autonomous systems, in which the controller is divided into multiple levels. For example, Antsaklis and Passino (1993) break a hierarchical autonomous controller for a space vehicle into three levels: Management and Coordination Level → Coordination Level → Execution Level. The lower levels incorporate conventional control techniques, while macro techniques are used for control decisions at higher levels. The higher levels essentially act as managers to ensure global performance and robustness to failures or model changes.

On a different physical scale, hierarchical controllers have been shown to be effective in MEMs systems, where the success of conventional control algorithms is limited due to physical distribution, delays, possible element failure, and difficulty in effective modeling. One particular concept of interest in large networks of MEMs sensors is a multihierarchy control organization, in which hierarchies centered on each 'agent', or controller, are interleaved to overcome mismatches between the organizational and physical distance among agents (Hogg and Huberman 1998). Guenther et al. (1997) found a multihierarchy based on market-based control was able to achieve comparable performance to a centralized controller with less power required. In addition, Hogg and Huberman (1998) found that the multihierarchical organization slightly outperformed the hierarchical organization in maintaining stability in the presence of modeling errors and time delay. However, these ideas do not directly transfer to civil systems, because often these MEMs systems are considered to be 'smart matter', in which the mechanical time scale is slow in comparison to sensor, communication, and computation speeds and the physical interconnections between agents are considered to be small or negligible (Guenther et al. 1997; Hogg and Huberman 1998).

2.3 Wireless Structural Control

Wireless smart sensors have become an exciting alternative to tethered systems for structural health monitoring (SHM). As smart sensors become cheaper and research in the area continues, dense deployments have been encouraged; for example, the most recent large-scale deployment on the Jindo Bridge in South Korea included 113 sensor nodes (Jo et al. 2011). These dense wireless smart sensor networks, which include onboard communication and processing capabilities, are an attractive alternative to tethered networks for control due to their ease of implementation and lower costs (Lynch and Loh 2006). However, smart sensors face numerous challenges when applied to wireless control, including both hardware and software. To highlight these challenges, this section will address the hardware used, implementations of real-time data acquisition, and previous experimental investigations of wireless control.

2.3.1 Wireless Control Hardware

Typically, a wireless control sensor unit consists of a sensing interface, computing core, wireless radio, and an actuation interface. Lynch and Law (2006) and Rice and Spencer (2009) provide a summary of academic and commercial wireless smart sensor platforms. Of the sensor node elements, two essential hardware components that should be addressed specifically for wireless control include the analog-to-digital converter (ADC) for sensing and the digital-to-analog converter (DAC) for issuing control commands. Chapter 3 will provide more theoretical background on the types of converters, while this section will present the hardware used in the literature.

The most important qualities of the sensor interface are the resolution and sampling rate (Lynch and Loh 2006). One additional concern for wireless control is the latency of the ADC architecture. However, for SHM applications, the latency present in the ADC is less of a concern; so often, improved resolution is traded for an ADC architecture that has higher latency. Because latency is not often considered, most sensor node specifications only provide the maximum sampling rate, ADC resolution, and the number of channels.

In wireless control, the most common ADC architecture used in the literature is a successive-approximation-register (SAR) type (Wang et al. 2006b; Lynch et al. 2008; Swartz and Lynch 2009; Wang and Law 2011). An SAR type ADC has minimal latency and is appropriate for high-resolution, medium throughput applications (Maxim Integrated Products 2001); thus, they are a good choice for wireless structural control. However, little rationale is provided in the literature for their selection besides the high maximum sampling rate; on the other hand, the literature on the hardware for wireless control often presents the actuation interface in detail.

Although additional components are used within the actuation interface to alter and amplify the output voltage range, the most important component is the DAC. This actuation interface is present in a broad category of sensors called 'Wireless Active Sensors', which includes both systems that are used for active sensing popular in non-destructive evaluation methods and structural control (Lynch and Loh 2006). As a result, the type of DAC selected is often tailored to the application requirements.

In wireless control, the main concerns are the resolution and speed of the DAC. The goal is that both the sensing and actuation interfaces are capable of comparable high-speeds and resolution. Casciati and Rossi (2003) present a wireless controller unit that has a 12-bit DAC that is equivalent to the sensor resolution capable of 0 to 10 V or bipolar 5V output. The initial unit employed by Lynch et al. (2004a) uses a 12-bit TI-DAC7642 DAC with zero-order-hold (ZOH) analog output and a low settling time for each conversion, which allows for high-speed operation. The next generation of the unit (WiSSCon, Wang et al. 2006a) used in several wireless control implementations upgrades to a 16-bit Analog Devices AD5542 DAC to output a stable zero-order-hold analog signal. The very low settling time of the DAC allows for very high sampling rates (1 MHz maximum). The Narada unit uses a two-channel 12-bit TI-DAC7612 DAC to provide steady analog outputs (Swartz et al. 2005; Swartz and Lynch 2009). In all these cases, the overall goal is to provide a zero-order-hold analog output signal with comparable resolution and speed to the sensing interface.

2.3.2 Real-time Data Acquisition

In SHM, two approaches to data acquisition in large sensor networks are used commonly to limit the impact of scarce power and bandwidth resources: data logging and decentralized data

aggregation. In the first, data is acquired locally on sensor nodes prior to sending the measured data individually back to the base station. The collected time histories can then be analyzed. This data logging approach better utilizes the transmission bandwidth when compared to real-time acquisition; however, the process can take a significant amount of time. In the second approach, data is acquired locally and then processed, typically in small communities of neighboring sensor nodes; the aggregated data is then returned to the gateway node (Rice et al. 2010). This approach leverages the onboard computational power to reduce transmission size and power consumption (Lynch et al. 2004b); however, complete time histories of the measured data are no longer available. On the other hand, real-time data acquisition allows wireless sensor systems to emulate tethered networks when real-time visualization of the response is desired or real-time state knowledge is necessary for systems that include actuation capabilities.

Therefore, the first step to achieving wireless structural control is real-time data acquisition, in which the data is transmitted to the gateway node with minimal latency. Despite the onboard processing and communication capabilities, real-time data acquisition on wireless smart sensors is challenging due to operating system limitations, tight timing requirements, sharing of transmission bandwidth, and unreliable wireless radio communication. As a result, recent sensor systems have implemented real-time data acquisition by limiting network size, channels acquired, and/or sampling rates.

The most common approach initially to achieve wireless real-time data acquisition was to decrease the sampling rate and the number of nodes communicating to limit the demands on the wireless bandwidth. Galbreath et al. (2003) achieve continuous streaming on their own prototype sensor by acquiring 3-channels of 12-bit sensor data sampled at 1 kHz on a single sensor node. In this monitoring approach, multiple nodes were not required to communicate with the gateway node. Similarly, Paek et al. (2006) limit the size of their networks and sampling rate to achieve sampling of 12 channels of acceleration across four nodes at 20 Hz using a TENET network composed of Stargate and MicaZ sensor nodes. Limited low-level software modifications or scheduling were required in these approaches.

On the other hand, Wang et al. (2007b) improve their possible data throughput by addressing low-level programming issues in the operating system. One major limitation of common wireless sensor operating systems is that they are single-threaded, thus sampling and sending cannot occur at exactly the same time. Wang et al. (2007b) use a multi-threaded operating system with multiple memory buffers that does not require sending within one sample period; and thus, they can use a retry and acknowledgement protocol to ensure reliable communication. As a result, they achieve reliable near-real-time transmission of 24 wireless sensors with 16-bit data at sampling rates up to 50 Hz on their own prototype sensor node. However, the reliable communication scheme and use of multiple memory buffers may introduce latency.

Another possible solution to improve throughput is to use a scheduled communication and sensing approach. Scheduling communication reduces contention on the wireless channel, which limits data loss due to collisions and delays due to clear-channel-assessments (CCA). One common approach is the time-division multiple access (TDMA) protocol that allows multiple leaf (remote) nodes to communicate with a single receiver, or gateway node, by transmitting in different time slots. Niu et al. (2009) achieve reliable near-real-time communication of 34 channels of 10-bit data across 17 nodes at up to 50 Hz on the IRIS sensor node by using a TDMA protocol with a buffer of multiple samples. The buffering of samples improves the throughput, but can introduce latency into the system. Furthermore, the TDMA communication

interval used is independent of the sampling rate or number of nodes and can result in buffer overflow at higher sampling rates and additional latency.

Whelan and Janoyan (2009) combine scheduling with low-level operating system modifications to achieve high-throughput real-time data acquisition. A throughput of 40 channels of 12-bit data over 20 nodes at a sampling rate of 128 Hz is achieved on the TmoteSky sensor node through low-level modification of TinyOS-1.x handling of events. These modifications include interrupt-driven handling of events rather than just a first-in-first-out (FIFO) scheme, which allows for prioritizing of critical events. To achieve reliable communication, they retransmit lost data, which can introduce some latency. While the Whelan and Janoyan (2009) system exhibits impressive performance, the time synchronization among nodes is only viable for several minutes, which limits the possible sensing interval.

Therefore, high-throughput real-time data acquisition that is viable over an extended interval has yet to be realized. A solution will require tightly scheduled communication and sampling along with time synchronization that is viable over an extended interval. For SHM applications, only near-real-time acquisition is required; and thus, some latency in the approach, such as buffering of samples, is practical. However, structural control applications require minimal latency; and thus, approaches with memory buffers of samples are impractical.

The overall goal of real-time acquisition for wireless structural control is to limit the total communication time; thus, real-time communication approaches for structural control typically use a scheduling method to limit contention delays and data loss. Lynch et al. (2008) outlines a TDMA-based communication scheme that ensures that no two nodes communicate with the controller, or gateway, node at the same time. The protocol used assumes three nodes are communicating with the controller node and uses predefined wait times for each node. The communication scheme is initiated when a beacon is sent to the remote sensor nodes. When implemented on their prototype sensor fitted with a 24XStream radio, the total data exchange takes about 74 ms, which results in a sampling rate of about 12.5 Hz. The resulting sampling rate is slow and highlights the challenges wireless communication presents in structural control; however, the general ideas of this scheduled approach can be applied to more powerful sensor nodes to improve real-time data acquisition for wireless control.

2.3.3 Wireless Structural Control Experimental Implementations

Several wireless structural control experiments have been conducted on semi-active systems to explore the challenges of using wireless smart sensor nodes and implement newly developed decentralized control algorithms. Semi-active control systems have the advantage that they are inherently stable, so they are well suited to the new area of wireless structural control, which can have data loss, slow sampling rates, and time delays. In these experiments, the wireless control hardware, real-time data acquisition protocol techniques, and decentralized control algorithms discussed previously are combined to achieve wireless structural control.

Wang et al. (2006a) were the first to experimentally explore the tradeoffs of control sampling rate and the decentralization of sensor feedback present in wireless structural control. They implemented centralized, partially decentralized, and decentralized control schemes on a three story steel structure with MR dampers located at each story and fitted with a WiSSCon wireless system. The decentralized wireless systems use the iterative procedure developed by Lunze (1992) to determine the control gains when considering LQR with velocity feedback. The resulting centralized wired system, fully decentralized wireless system, partially decentralized wireless system, and centralized wireless system operate at 200 Hz, 50 Hz, 16.67 Hz, and 12.5

Hz, respectively. The slower sampling rates, when more data is fed back to the controller, were due to the time required for wireless radio communication. The fully decentralized system was able to achieve comparable performance to the centralized wired LQR design. Among the wireless cases, the superior performance of the fully decentralized system highlights that the lack of complete sensor data is overcome by the higher sampling rate (or lower communication latency).

Lynch et al. (2008) explore the effect of slow sampling rates and the information feedback on the performance of the wireless structural control system. Centralized wired and wireless systems are implemented on a three-story, single-bay steel structure fitted with an MR damper on the first story and using WiSSCon wireless sensor nodes. An in-depth discussion of the wireless sensor implementation is provided, including an outline of the TDMA communication scheme used and psuedocode of the controller software. The resulting wired and wireless systems operate at 200 Hz and 12.5 Hz, respectively. In comparison to the passive-on and passive-off cases, the wireless system using velocity feedback was more successful at mitigating the response of far-field earthquakes. The wireless system performed worse than the wired system for the near-field Chi-Chi and Kobe earthquakes. This poor performance is attributed to the state truncation when using velocity state feedback and the slower sampling rate. Utilizing acceleration feedback, the system performed as well or better than the other control systems (passive and wired). In addition, the work highlights the idea that decentralized control and an improved communication protocol could further enhance performance by increasing the wireless sampling rate.

Loh et al. (2007) investigate the application of fully decentralized control to a system using acceleration feedback. They compare wireless (WiSSCon) and wired control systems on a three-story steel structure with an MR Damper on each story. Both centralized and fully decentralized discrete LQG control designs are presented; as discussed previously in Loh and Chang (2008), the fully decentralized algorithm is based on individual subsystem design rather than an ad-hoc decentralization of the centralized solution or solving for the optimal overall decentralized design. The TDMA communication protocol requires a significant amount of time for each send and computation, which results in a centralized wireless system sampling rate of 10 Hz. On the other hand, the fully decentralized system, which only requires computation, operates at 50 Hz. In their analysis of the system, the performance of the wireless system is discussed, including the accuracy of the wireless LQG calculations, MR Damper calculations, and data loss, as well as the actual control performance when compared to a wired system. The wireless systems, both centralized and decentralized using acceleration feedback, have almost the same control effectiveness as the wired system; and, the closed-loop wireless controllers typically outperform the passive-on and –off cases.

Swartz and Lynch (2009) use a partially decentralized control architecture, where the level of communication between nodes depends on the error between the true states and estimate, to improve the performance of wireless structural control systems using acceleration feedback. Based on the work by Swartz et al. (2005) discussed previously, they investigate different error thresholds, performance, and the communication required. The wireless control system is applied to a six-story single-bay, scaled, steel structure fitted with an MR damper at each story. By using an acknowledged TDMA scheme on the Narada node, which has a multithreaded operating system, the TDMA communication protocol results in an operating sampling rate of 33 Hz. The results showed that an optimal error threshold that maximized the improved performance of partially decentralized control while limiting the communication required; however, when they

compare the results with essentially centralized or fully decentralized solutions, they don't consider that these approaches might use different sampling rates, i.e. a fully decentralized architecture would offer a faster sampling rate.

To improve the performance of wireless control systems using velocity feedback, time delay is considered in the control algorithm development by Wang et al. (2007a). The time-delayed LQR algorithm initially discussed in section 2.2.1 is applied to a three story, single bay, steel structure fitted with an MR damper at each story. The Narada unit is utilized for the wireless system, where the centralized system operates at 12.5 Hz, partially decentralized at 16.67 Hz, and fully decentralized at 50 Hz. The wired system used for comparison operates at 200 Hz. The simulation and experimental results highlight the importance of considering sampling rate and decentralized control architecture in the control design; the decentralized wireless strategies provide equivalent or better performance than centralized approaches due to the higher sampling rate. Although the paper does not directly compare the time-delay compensation approach with a non-compensated approach, the good performance of the wireless system using velocity feedback suggests that the approach is advantageous.

Wang and Law (2011) next apply several partially decentralized time-delayed control designs, which use multiple communication subnets to improve performance. The control designs are based on the time-delayed H_∞ decentralized control algorithm discussed by Wang (2011) and addressed previously in section 2.2.1. The experiment consists of a six-story, scaled, steel structure fitted with an MR-damper between each story and a Narada control unit at each device interfaced with two velocity meters. Four levels of decentralization are considered, ranging from centralized to completely decentralized, with the corresponding sampling intervals: 47, 18, 12, and 7ms; the communication is assumed to take 2ms each with computation requiring the majority of the interval. This result is the first reported experiment to utilize different communication channels for each subnet. In general, the results were not as good as in simulation, which is attributed to possible modeling errors of the structure and MR Damper. Looking at both the RMS and peak responses, the centralized system performed the best and next was two subnets of three nodes. While all feedback systems outperformed passive-off, the more decentralized schemes did not improve on passive-on. Although the idea of multiple subnets is promising, the poorer than expected performance in this case might be overcome through the use of overlapping subnets.

These experimental investigations of wireless structural control highlight the tradeoff between degree of decentralization, sampling rate, and performance. In addition, the application of algorithms that include time delay and approaches to limit communication offer practical examples that can be used in future work. However, in all these cases, the main objective was to improve control performance. Although the stability of semi-active systems is guaranteed due to BIBO stability, the feasibility and performance of these approaches on active control systems is not guaranteed, because they are likely more sensitive to sampling rate, delays, and data loss.

2.3.4 Wireless Active Control

To date, the only reported use of wireless sensors for active structural control system has been by Casciati and Chen (2012), who examined control of a three-story, steel structure fitted with an active mass driver (AMD). The wireless sensor uses a CC1110 transceiver that includes an onboard microprocessor. The sensor measurements are transmitted using a frequency division multiplexing (FDM) technique in which each of the remote sensors uses a different frequency band and the structural controller is fitted with multiple wireless transceivers. The wireless

measurements are then fed into the microcontroller for control calculations, and the desired control displacement is output to a board designed by the authors for PID control of the AMD. The wireless system is able to achieve comparable performance to the wired system when the building is subjected to a sinusoidal excitation at its natural frequency. Although the performance of the system is promising, the time required for this FDM technique and the resulting sampling rate for the system is not provided. In addition, the scalability of this centralized system is limited because the number of communication channels and wireless transceivers required at the controller node will increase linearly as the number of remote sensors increases.

Although only one experimental investigation of wireless active structural control has been completed, some investigations of wireless control have been considered for active mechanical systems. Such systems typically use controllers linked through a wireless network rather than wireless smart sensors. In addition, stability is often addressed and considered alongside performance. Wireless control also has been investigated for other systems, such as industrial processes; however, the time scales for these problems are typically much longer than found for structural systems and thus, are not considered.

A fundamental mechanical system addressed in wireless control is stabilization of an inverted pendulum; thus, stability is directly addressed when considering delays, data loss, and sampling rate. Initially, Eker et al. (2001) investigate the tradeoff between time delays and reliable transmission when two nodes connected over Bluetooth are used to control the inverted pendulum. They consider two approaches: a varying delay with reliable transmission and unreliable transmission with a stable delay. The variable delay LQR control design is found to be successful at stabilizing the system, while assuming a constant delay or non-compensation when reliable transmission is used results in instability. An estimation approach to correct bit errors combined with static delay compensation effectively stabilized the system; however, when incorrect data is used in the controller, instability resulted. Since the tradeoff between reliable communication and data loss is a concern with wireless systems, the approaches presented offer some insight for wireless active structural control.

One other approach to network contention and data loss is to use a varying sampling rate. Poplys et al. (2004) maintain stability of the inverted pendulum at the upright position with a control system comprised of two nodes connected over an 802.11 network. They use an event-driven control approach, where sensing is based on the clock and actuation is based on receipt of a control command; thus, time synchronization among individual nodes is not required. A discrete LQR control design operating at 200 Hz is used to maintain stability in the presence of a one-step time delay. Furthermore, the system is shown to be robust for various sampling rates and packet loss rates until ultimately instability occurs. As a result, a slowly adjusting sample rate approach is considered to maintain a target packet loss rate and reliability for various sampling rates (100-250Hz are considered). Finally, the system is extended to a multi-input multi-output system with light tracking to investigate the improvement in performance using coordinated control. The coordinated control proves successful and does not seem to hinder the performance of the individual control loops, but rather improves the performance of the total system. Although the sampling rates used are higher than what is typically possible with a wireless smart sensor, the consideration of stability with delays and the idea of adjusting the sampling rate to balance performance and data loss could be applied to active control structural systems.

Kawka and Alleyne (2005) further investigate the stability of the wirelessly controlled inverted pendulum and the performance improvement offered by varying the sampling rate over

time. They examine the control of the inverted pendulum by framing the problem as a 2-state Markov model, which can be used along with H_∞ norms to identify stability regions and expected performance. Ultimately, these results inform a decentralized control approach that adjusts the sampling rate (i.e., required rate of communication) based on communication performance in the network. The two states used in the model are based on network performance; when communication fails, the control command is set to zero, such that the system is open loop. Otherwise, the system operates in a closed-loop state. The probability of closed-loop to open loop is used as a feedback parameter, within a set of bounds, to vary the sampling period. The strategy, examined experimentally, improves controller performance as measured by tracking error and successful transmission when communication disturbances are present. Again the sampling intervals used here are likely faster than what is currently possible with a wireless smart sensor, but the idea of adjusting the sampling rate in real-time is promising.

2.4 Summary

The literature review in this chapter shows the progression of structural control research, focusing on studies that have sought to overcome and account for practical considerations, including time delay, sampling rate, etc. Wireless structural control is particularly susceptible to these inherent hardware and software related challenges due in part to communication and data loss. Experimental application of wireless structural control to semi-active control systems is a promising first step towards investigating wireless control, because the systems are inherently stable. These implementations have highlighted the tradeoffs between decentralization, sampling rate, and performance. This research will focus on addressing the hardware and software limitations, in addition to the previously considered tradeoffs, to enable successful implementation of wireless active structural control.

BACKGROUND

To lay the foundation for the research presented herein, this chapter provides technical background on both the wireless sensing and control elements, including the wireless smart sensor platform, the existing software architecture, and optimal control techniques.

3.1 Wireless Smart Sensor Platform

3.1.1 Imote2

While numerous wireless smart sensing platforms, both commercially and academically available, have been developed for SHM applications (Lynch and Loh, 2006), the Imote2 was selected for this work. The Imote2, shown in Figure 3.1, is well suited for high data-throughput applications due to its high and variable processing speed, large onboard memory, and low-power radio. The XScale PXA271 processor allows for variable processing speeds, including 13, 104, 208, and 416 MHz, that can be selected based on tradeoffs between performance and power consumption. In addition, the higher processing speed allows control computations to be completed quickly to limit latency. The onboard memory consists of 32 MB of flash, 256 KB SRAM, and 32 MB of SDRAM. The Imote2 utilizes the popular CC2420 low-power radio that can be combined with an onboard or external antenna for wireless communication over the 2.4 GHz wireless band using the IEEE 802.15.4 protocol. The radio offers a theoretical maximum transfer speed of 250 Kbits/sec.

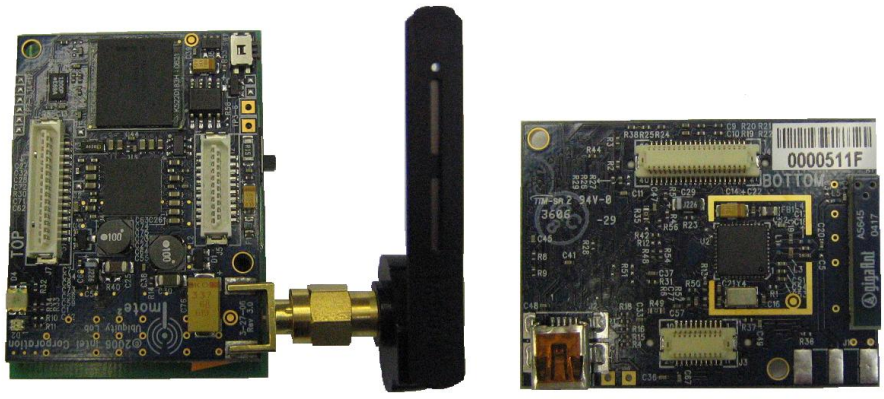

Figure 3.1: Imote Smart Sensor Platform: Top View (left), Bottom View (right).

3.1.2 SHM-A Sensorboard

The Imote2 platform does not provide an onboard ADC, instead allowing it to interface with a user-selected sensor board over its basic connectors. The SHM-A sensor board, designed for SHM applications, was initially selected for this work among the commercially available sensor boards for the Imote2 due to its high-sensitivity accelerometers and high-resolution analog-to-

digital converter with user-selectable sensing parameters (Rice and Spencer 2009). The sensor board, shown in Figure 3.2, consists of a three-axis accelerometer (ST Microelectronics LIS344ALH), temperature and humidity sensor (Sensirion SHT11), light sensor (TAOS 2561), and an external 16-bit analog input. The four analog signals interface with a 16-bit analog-to-digital converter (QF4A512), which offers user-selectable anti-aliasing filters and sampling rates.

Figure 3.2: Imote2 fitted with SHM-A sensor board and external antenna.

The Quickfilter QF4A512 is an oversampling, pipeline type analog-to-digital converter that oversamples and digitally applies filters and decimation to achieve high-resolution, anti-aliased data (Quickfilter 2007). The general architecture is shown in Figure 3.3. The analog portion consists of a pre-gain amplifier (PGA) and a high-cutoff anti-aliasing filter. The analog-to-digital converter (ADC) is 12-bits in hardware but oversamples and averages the resulting conversions to achieve up to a 13.1 ENOB resolution. The digital signal is then passed to the Finite Impulse Response (FIR) Filter for user-defined filtering. The FIR filters can accommodate up to 512 taps each.

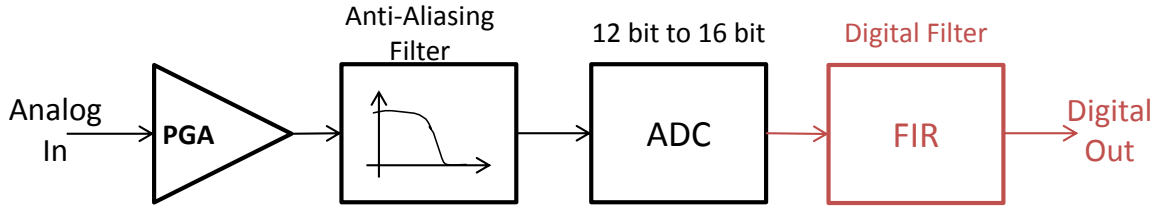

Figure 3.3: Quickfilter architecture (Quickfilter 2007).

3.2 Analog-to-Digital Converter Hardware

The analog-to-digital converter (ADC) architecture should be selected based on the application. Two main types of analog to digital converters exist: those that complete the conversion within one sampling interval and those that have an inherent latency until the data is available. The first, which includes Flash and Successive Approximation Register (SAR) ADCs, is best suited for low latency applications such as control. The second type, which includes Pipeline and Sigma-Delta ADCs, is suited for high-resolution applications where latency is less of a concern, such as SHM. This section will discuss the two main ADC architectures that are used in this work: the SAR and Pipeline ADCs.

3.2.1 Successive Approximation Registers

A successive approximation converter is well-suited for medium to high-resolution applications with moderate throughput. Typical SAR converters range from 8 to 16 bits and have speeds up to 5 megasamples per second (Msps) (Maxim 2001). The architecture implements a binary search

algorithm to determine the N-bit register value for the corresponding analog input (Pelgrom 2010). A schematic of an SAR converter is shown in Figure a and a 4-bit example of the search algorithm is provided in Figure b. As illustrated, the analog input is held initially with the sample and hold. The binary search algorithm starts with V_{DAC} held to midscale, which is compared with the voltage input. If V_{IN} is higher than $V_{REF}/2$, the bit is held high, otherwise it is flipped to zero. The SAR logic then moves to the next bit in the register and flips it high. This voltage is output through the digital-to-analog converter (DAC) and then compared with V_{IN} as before. The process continues until all N-bits of the register are addressed. In the 4-bit example (Figure a), V_{DAC} used for comparison is shown in bold.

The throughput and accuracy of the converter is a function of the components, mainly the DAC and comparator. Due to the algorithm, *N* clock samples are required for conversion. As a result, although the internal hardware is running at the higher clock rate, the available ADC sample rate is a fraction of that rate. The maximum sampling rate is limited by the DAC settling time for the V_{DAC} to stabilize prior to comparison and the speed of the comparator itself. Similarly, the accuracy of the converter is limited by the DAC and the comparator.

3.2.2 Pipeline Converter

The pipeline architecture is well-suited for high-throughput, high-resolution applications where some latency is not a concern. The converter is a multiple-stage analog-to-digital converter, which typically consists of *N* similar stages that account for a bit of resolution (Pelgrom 2010). Once a stage completes processing a sample and passes it on to the next stage, the stage can start processing the next sample received. This pipeline architecture increases the throughput, but introduces latency. Thus, for an *N*-stage pipeline at least *N* sample delays exist; plus, there is additional delay due to the digital reconstruction and error correction. Therefore, the delay between the initial sampling and the digital output can be significant.

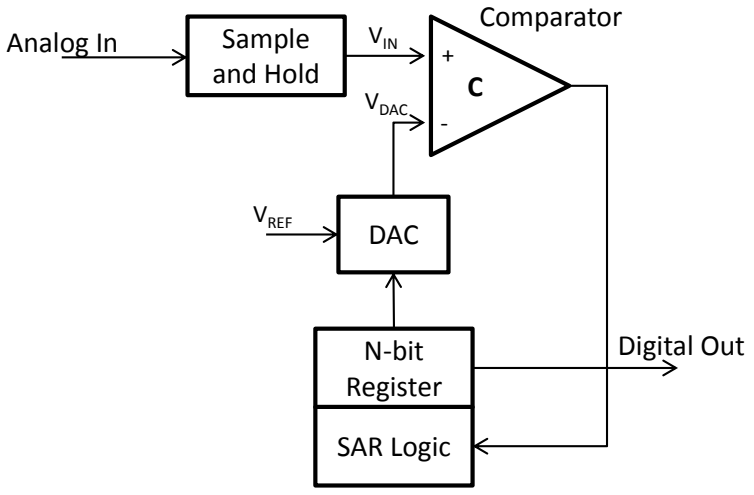

Figure 3.4: (a) Schematic of successive approximation architecture (Maxim 2001) (b) 4-bit example of binary search algorithm.

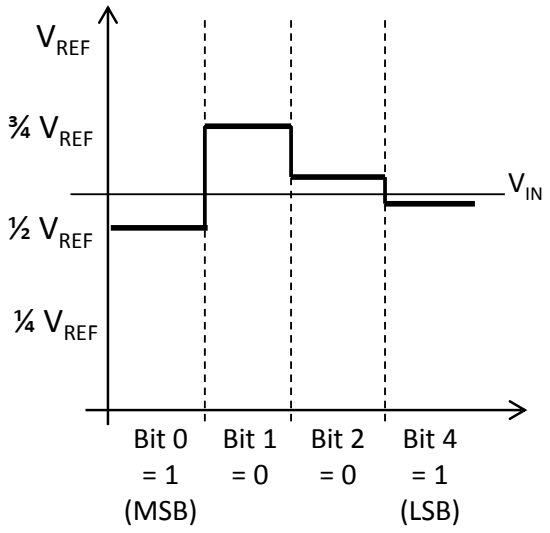

(b)

Figure 3.4 continued.

3.3 Essential Embedded Software Components

Embedded software is an essential component in the design of real-time wireless data acquisition, which is required for structural control. This section will discuss four main components of the software for application development. First, the operating system and overall software architecture; and then, more specifically, time synchronization and the sensing approach.

3.3.1 Operating System

The operating system popular with numerous embedded wireless sensor networks, TinyOS, is used on the Imote2 (Lynch and Loh 2006). TinyOS (www.tinyos.net) is a component-based operating system written in the NesC language, a version of C for embedded systems, which has limited memory requirements. The open-source software supports an event-driven concurrency model, in which tasks are completed in a first-in-first-out (FIFO) manner along with interrupts (Levis et al. 2005). The inclusion of asynchronous interrupts allows the system to interact with real-time hardware. Thus, two main execution methods are possible: a task posted to a queue and an asynchronous interrupt handler.

3.3.2 Software Architecture

Similar to a component-based operating system, the Illinois Structural Health Monitoring (ISHMP) Services Toolsuite (http://shm.cs.uiuc.edu/software.html) employed in this work utilizes a modular service-oriented architecture. The framework consists of three main elements: foundation services, application (domain-specific) services, and tools and utilities (Rice et al. 2010). A typical application would combine several foundation and application services. Several of the key foundation services to support real-time sensing include reliable communication and synchronized sensing. The reliable communication service allows reliable sends of different message types, including commands and long data sets. The synchronized sensing service

combines time synchronization, which provides global timestamps, and resampling to account for sampling offset and variation of sampling rates (Nagayama et al. 2009).

3.3.3 Time Synchronization

Precise time synchronization serves two key purposes in applications that require tight event scheduling and sensing, such as real-time sensing: (i) providing consistent global timestamps for synchronizing the data acquired from different sensor nodes, and (ii) scheduling communication. Time synchronization errors in sensor data can introduce phase errors in SHM applications (Nagayama et al. 2007). Thus, while approximately 1 ms precision typically suffices for communication scheduling, much tighter precision is needed for acquiring high-quality synchronized data.

Each individual sensor node has its own local clock, which is not initially synchronized with the other nodes. In addition, each clock ticks at a slightly different rate. Through communication between nearby nodes, the sensors can assess and correct for the relative difference in their local clocks. Several well-known time synchronization algorithms exist including the Flooding Time Synchronization Protocol (FTSP, Maróti et al. 2004).

A custom time synchronization protocol for SHM applications on the Imote2 has been implemented (Nagayama et al. 2009). By extending the Flooding Time Synchronization Protocol with clock drift estimation and compensation features, the protocol maintains synchronization error within 80 μs over a period of several minutes without resynchronization.

Li et al. (2012) has transformed the time synchronization protocol to be viable over a longer sampling interval and limit the initial latency due to clock drift estimation. The system aligns clocks initially and then synchronizes the data post-sensing. This approach is not currently viable for applications that require tight scheduling and real-time sensing; however, the approach could be combined with the original protocol to extend the synchronization over a longer sampling interval.

3.3.4 Sensing Approach

In general, the sensing application on the Imote2 interfaces with the sensor board through driver commands. The user first specifies the desired channels, sampling rate, and number of samples. The application relays this information to the driver when posting a sensing task. When the driver is initialized, sensing begins and the data is passed to the application through a buffer. Sensing continues until the desired amount of data has been acquired.

3.4 Optimal Control Techniques

The controllers used in this work consist of an estimator and control gain designed separately based on the separation principle. Although numerous design techniques and algorithms exist for selecting control and estimator gains, common optimal control algorithms are used in this work: linear quadratic regulator and Kalman filter. Initially, the state-space representation of the equations of motion, on which these methods are based, is presented in this section followed by the two optimal design techniques.

3.4.1 State-Space Representation of the Equations of Motion

The optimal control techniques outlined in this section are based on the state-space formulation of the dynamic equations of motion. The state-space formulation offers a different way to represent the same equation of motion. These state-space based methods are particularly advantageous when designing controllers for multi-input, multi-output (MIMO) systems and systems with time delays.

The state variables $\mathbf{z_1}$ and $\mathbf{z_2}$ are defined as the displacement and velocity vectors; therefore, the state vector can be represented as

$$\mathbf{z} = \begin{bmatrix} \mathbf{z}_1 \\ \mathbf{z}_2 \end{bmatrix} = \begin{bmatrix} \mathbf{x} \\ \dot{\mathbf{x}} \end{bmatrix} \tag{3.1}$$

Thus, a system with a second order equation of motion

$$\mathbf{M}\ddot{\mathbf{x}} + \mathbf{C}\dot{\mathbf{x}} + \mathbf{K}\mathbf{x} = \mathbf{u}(t) \tag{3.2}$$

where **M** is the mass matrix, **C** is the damping matrix, **K** is the stiffness matrix, **F(t)** is the excitation, and **x** is the degree of freedom, can be represented using Eq. (3.1) as a set of two first order differential equations known as the state equation:

$$\begin{bmatrix} \dot{\mathbf{z}}_1 \\ \dot{\mathbf{z}}_2 \end{bmatrix} = \begin{bmatrix} \mathbf{0} & \mathbf{I} \\ -\mathbf{M}^{-1}\mathbf{K} & -\mathbf{M}^{-1}\mathbf{C} \end{bmatrix} \begin{bmatrix} \mathbf{z}_1 \\ \mathbf{z}_2 \end{bmatrix} + \begin{bmatrix} \mathbf{0} \\ \mathbf{M}^{-1} \end{bmatrix} \mathbf{F}(t) \tag{3.3}$$

The state equation is commonly represented in compact matrix form as

$$\dot{\mathbf{z}} = \mathbf{A}\mathbf{z} + \mathbf{B}\mathbf{u} \tag{3.4}$$

where **A** and **B** are the system matrices and **u** is the system input, defined as

$$\mathbf{A} = \begin{bmatrix} \mathbf{0} & \mathbf{I} \\ -\mathbf{M}^{-1}\mathbf{K} & -\mathbf{M}^{-1}\mathbf{C} \end{bmatrix}, \mathbf{B} = \begin{bmatrix} \mathbf{0} \\ \mathbf{M}^{-1} \end{bmatrix}, \text{ and } \mathbf{u} = \mathbf{F}(t) \tag{3.5}$$

The measurements of the system, **y**, is given by the measurement equation

$$\mathbf{y} = \mathbf{C}\mathbf{z} + \mathbf{D}\mathbf{u} \tag{3.6}$$

where **C** and **D** are functions of the state variables selected to represent the measurements of the system desired or available. For example, if the velocity measurements are the only output of the system, the **C** and **D** matrix would be given by

$$\mathbf{C} = \begin{bmatrix} \mathbf{0} & \mathbf{I} \end{bmatrix} \text{ and } \mathbf{D} = \begin{bmatrix} \mathbf{0} \end{bmatrix} \tag{3.7}$$

In this work, we assume a linear time invariant (LTI) system in which the stiffness, damping, and mass matrices do not change. Therefore, **A**, **B**, **C**, and **D** are assumed to be constant.

For systems sampled at a slower rate, a discrete time representation of the system is advantageous for control design (Franklin et al. 1998). If we assume the control is applied from the computer using a zero-order hold (ZOH), then we can obtain the discrete state-space representation of the system

$$\begin{aligned}\mathbf{z}[k+1] &= \Phi\mathbf{z}[k] + \Gamma\mathbf{u}[k] \\ \mathbf{y}[k] &= \mathbf{C}\mathbf{z}[k] + \mathbf{D}\mathbf{u}[k]\end{aligned} \tag{3.8}$$

where

$$\Phi = e^{\mathbf{A}T},\ \Gamma = \int_0^T e^{\mathbf{A}\eta} d\eta \mathbf{B} \tag{3.9}$$

and T is the sampling period.

3.4.2 Linear Quadratic Regulator Control

Given a feedback control system, linear quadratic regulator (LQR) control design provides a balance between good system response and the control effort required (Franklin et al. 1998). The control design gets its name because it applies to linear systems, has a quadratic cost function, and regulates (controls) the state of the system. Initially the continuous-time representation will be presented followed by the discrete time formulation.

In continuous time, the method calculates a feedback gain **K** that minimizes the following cost function

$$J = \int_0^\infty \left[\mathbf{z}^\mathbf{T}\mathbf{Q}\mathbf{z} + \mathbf{u}^\mathbf{T}\mathbf{R}\mathbf{u}\right] dt \tag{3.10}$$

where **Q** is a positive semi-definite state weighting matrix and **R** is a positive definite control weighting matrix. The values of **Q** and **R** are selected by the designer to achieve a desired closed-loop response. The resulting gain, **K**, yields the optimal closed-loop controller to achieve this balance of control effort and system response.

The solution for the steady-state optimal control

$$\mathbf{u} = -\mathbf{K}\mathbf{z} \tag{3.11}$$

that minimizes Eq. (3.10) is

$$\mathbf{K} = \mathbf{R}^{-1}\mathbf{B}^\mathbf{T}\mathbf{P} \tag{3.12}$$

where **P** is the positive definite solution of the algebraic Riccati equation, given by

$$\mathbf{A}^\mathbf{T}\mathbf{P} + \mathbf{P}\mathbf{A} + \mathbf{Q} - \mathbf{P}\mathbf{B}\mathbf{R}^{-1}\mathbf{B}^\mathbf{T}\mathbf{P} = \mathbf{0} \tag{3.13}$$

The algebraic Riccati equation has well-known solution techniques.

In discrete time, the linear quadratic regulator design serves the same function, but has a slightly different representation. The cost function minimized in discrete time is

$$J = \frac{1}{2}\sum_{k=0}^{\infty} [\mathbf{z}^T(k)\mathbf{Q}\mathbf{z}(k) + \mathbf{u}^T(k)\mathbf{R}\mathbf{u}(k)] \tag{3.14}$$

where **Q** and **R** have the same properties as in continuous time. The states and input are now a function of the sample, k.

Similarly, the solution for the steady-state optimal control

$$\mathbf{u}(k) = -\mathbf{K}\mathbf{z}(k) \tag{3.15}$$

that minimizes Eq. (3.14) is

$$\mathbf{K} = \left(\Gamma^T \mathbf{S}\Gamma + \mathbf{R}\right)^{-1} \Gamma^T \mathbf{S}\Phi \tag{3.16}$$

where **S** is the positive definite solution of the discrete algebraic Riccati equation, given by

$$\mathbf{S} = \Phi^T [\mathbf{S} - \mathbf{S}\Gamma \mathbf{R}^{-1} \Gamma^T \mathbf{S}]\Phi + \mathbf{Q} \tag{3.17}$$

Thus, the solution has a similar procedure, but each equation has a slightly different form.

3.4.3 Kalman Filter

The LQR control design assumes full-state feedback; however, rarely is the full state information available to the controller. Typically, only a few measurements are available, e.g., accelerations. Thus, an estimator is used to reconstruct the state elements used for the control law as shown in Figure 3.5. The Kalman filter is an optimal model-based predictor-corrector type estimator in that it minimizes the variance of the estimated error covariance in the presence of Gaussian type process and measurement noise (Stengel 1986). Although the Kalman filter was originally derived in discrete-time, the continuous-time Kalman filter will be initially presented and followed by the discrete-time implementation (Stengel 1986).

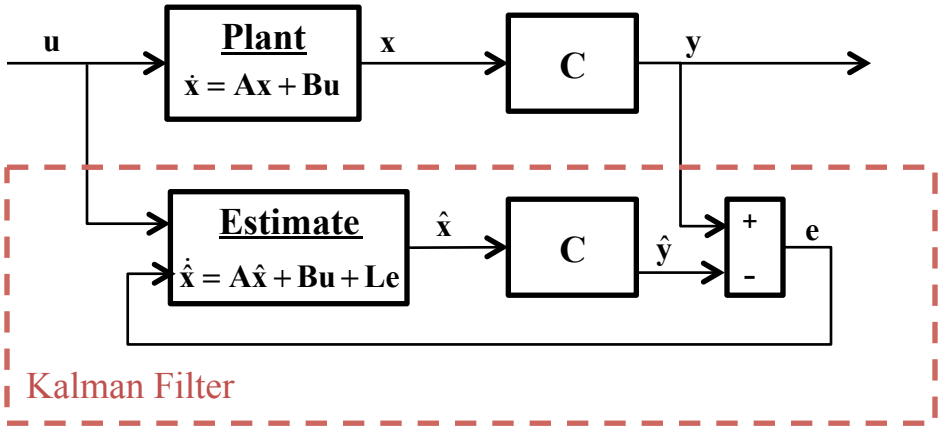

Figure 3.5: Block diagram of Kalman Filter.

In continuous-time, the typical state-space plant model is represented as

$$\begin{aligned} \dot{\mathbf{z}} &= \mathbf{A}\mathbf{x} + \mathbf{B}\mathbf{u} + \mathbf{G}\mathbf{w} \\ \mathbf{y} &= \mathbf{C}\mathbf{x} + \mathbf{v} \end{aligned} \tag{3.18}$$

where the previous state-space model is augmented with the process noise, **w**, and measurement noise, **v**. The noise variables are assumed to be white noise processes uncorrelated with each other and with covariances defined by

$$\mathrm{E}\left[\mathbf{w}(t)\mathbf{w}(t+\tau)\right] = \mathbf{S}_w \delta(t), \quad \mathrm{E}\left[\mathbf{v}(t)\mathbf{v}(t+\tau)\right] = \mathbf{S}_v \delta(t) \tag{3.19}$$

The measurement noise can be determined experimentally; however, the process noise is harder to evaluate. In general, the relative noise weighting of $\mathbf{S_w}$ and $\mathbf{S_v}$ can be tuned by the designer to balance the speed and accuracy of the resulting estimator.

An estimate of the state, $\hat{\mathbf{x}}$ is obtained from the resulting estimator given by

$$\dot{\hat{\mathbf{x}}} = \mathbf{A}\hat{\mathbf{x}} + \mathbf{B}\mathbf{u} + \mathbf{L}(\mathbf{y} - \mathbf{C}\hat{\mathbf{x}}) \tag{3.20}$$

where the open-loop estimate accounting for system dynamics, or time update, is corrected using the measurement weighted by the Kalman gain, **L**, as shown in Figure 3.5. If the estimated state, $\hat{\mathbf{x}}$, is subtracted from the true state **x**, the dynamics of the error in the estimate, $\tilde{\mathbf{x}}$, is represented by

$$\dot{\tilde{\mathbf{x}}} = (\mathbf{A} - \mathbf{L}\mathbf{C})\mathbf{x} \tag{3.21}$$

and should go to zero if the estimator gain is selected properly and the system is observable. Note that **D** is assumed to be zero, since in our applications the input does not directly feed through to the measurements.

The steady-state Kalman gain, **L**, is given by

$$\mathbf{L} = \mathbf{P}\mathbf{C}^T\mathbf{S}_v^{-1} \tag{3.22}$$

where **P** is the error covariance. Similar to the LQR solution, the error covariance, **P**, is the positive definite solution to the algebraic Riccati equation

$$\mathbf{A}\mathbf{P} + \mathbf{P}\mathbf{A}^T - \mathbf{P}\mathbf{C}^T\mathbf{S}_v^{-1}\mathbf{C}\mathbf{P} + \mathbf{G}\mathbf{S}_w\mathbf{G}^T = 0 \tag{3.23}$$

While the solution is similar in discrete time, the estimator is typically implemented predicator-corrector form. The state-space model of the plant is similarly represented as

$$\begin{aligned} \mathbf{z}[k+1] &= \Phi\mathbf{z}[k] + \Gamma\mathbf{u}[k] + \mathbf{G}\mathbf{w}[k] \\ \mathbf{y}[k] &= \mathbf{C}\mathbf{z}[k] + \mathbf{v}[k] \end{aligned} \tag{3.24}$$

where the measurement and process noise have the same properties as before. The first stage is the time update, in which the state estimate, $\hat{\mathbf{z}}_{k+1}$ is predicted based on the previous estimate and the system dynamics. This estimate is then corrected using a measurement update that accounts for the effect of the measurement $\mathbf{y}_k$. The steps are outlined below (Lewis 1986).

For each *k = 1,2,…*

Step 1: Time Update (between measurements)

$$\hat{\mathbf{z}}_{k+1}^- = \Phi\hat{\mathbf{z}}_k + \Gamma\mathbf{u}_k \tag{3.25}$$

Step 2: Measurement Update (at measurement time)

$$\hat{\mathbf{z}}_{k+1} = \hat{\mathbf{z}}_{k+1}^- + \mathbf{L}(\mathbf{y}_{k+1} - \mathbf{C}\hat{\mathbf{z}}_{k+1}^-) \tag{3.26}$$

The steady-state Kalman gain used in the measurement update is given by

$$\mathbf{L} = \mathbf{P}\mathbf{C}^T(\mathbf{C}\mathbf{P}\mathbf{C}^T + \mathbf{S}_v)^{-1} \tag{3.27}$$

where **P** is the steady-state error covariance. The error covariance, **P**, is the positive definite solution of the discrete algebraic Ricatti equation

$$\mathbf{P} = \Phi\left[\mathbf{P} - \mathbf{P}\mathbf{C}^T\left(\mathbf{C}\mathbf{P}\mathbf{C}^T + \mathbf{S}_v\right)^{-1}\mathbf{C}\mathbf{P}\right]\Phi^T + \mathbf{G}\mathbf{S}_w\mathbf{G}^T \tag{3.28}$$

3.5 Summary

This chapter provides an overview of the wireless smart sensor platform and control algorithms used in this work. The wireless sensor hardware, specifically the ADC used, has inherent implications on the latency in the system. Thus, the architecture should be considered. In addition, the operating system and software framework will inform the solution used in wireless control. The control algorithms presented, both centralized and decentralized representations, need to be considered due to the slower sampling rates possible in wireless systems, as discussed in Chapter 2. Utilizing the hardware, software, and control algorithm background outlined in this chapter, will contribute to the successful implementation of wireless structural control.

Chapter 4

LOW-LATENCY SENSING AND ACTUATION HARDWARE

The time-domain performance requirements of wireless sensor hardware are unique for control applications, as compared to health monitoring, due to the real-time feedback required. Sensing hardware tailored to monitoring applications often uses digital filtering, which may result in significant latency. As a result, careful evaluation should be carried out to assess the applicability of such hardware for structural control purposes. Similarly, actuation hardware that complements the data acquisition performance is required to complete the control loop. By developing low-latency sensing and actuation hardware, the high-performance processing of the Imote2 can be leveraged for structural control applications.

4.1 Evaluation of SHM-A Sensor Board

The performance of the SHM-A has been evaluated to establish to assess its applicability for structural control. As discussed in Chapter 3, the analog to digital converter (ADC) used on the SHM-A is tailored for structural health monitoring applications; therefore, the sensor board may have limitations in terms of control applications. The major focus of the evaluation is latency introduced by the pipeline architecture and an approach to limit this latency.

The oversampling, pipeline style of the Quickfilter ADC requires the use of digital FIR (Finite Impulse Response) filters for downsampling and filtering, which can introduce significant latency. The filters used in structural health monitoring to limit aliasing and improve noise rejection require a significant number of taps. The total number of latency samples is a combination of the delay within the ADC architecture and the taps in the FIR filter. For example, 89 sample delays are required for a good 50 Hz filter design, which results in a delay of 1.78 seconds due to the Quickfilter chip alone. This delay is significant and not suitable for most structural control applications. Because an FIR filter is required for this ADC, alternative solutions with filters requiring fewer taps and utilizing higher sampling rates are necessary.

The proposed solution to limit the latency with the SHM-A is to maximize the possible sampling rate on the sensor board and minimize the taps used in the filter. The latency is a function of the number of taps and the sampling rate as shown in equation (4.1). The minimum number of samples, even when an all-pass filter is used, is 26, which is substantially lower than the previous filter design. In addition, a higher sampling rate results in a smaller latency for the same number of taps. The highest reliable sampling rate with continuous sensing of the SHM-A is 1,000 Hz. This results in a latency of 26 milliseconds for a maximum control system rate of 38 Hz. Thus, data is oversampled on the Quickfilter chip at 1,000 Hz and decimated on the Imote2 to the rate desired.

$$Latency = \#_{samples} \times 1/f_s \tag{4.1}$$

Note that decimation on the Imote2 without digital filtering will result in aliasing. Selecting an appropriate sampling rate given the system bandwidth can reduce aliasing at frequencies of interest; however, the noise floor will significantly increase by noise aliasing back into the range of interest. Thus, including some digital filtering might be advantageous, despite the associated delay. A low-pass filter with a cutoff frequency of 150 Hz and a slow roll-off is

used to reduce the noise present in the decimated system; the extra taps of the filter only results in an additional delay of three samples, yielding a total latency of 29 ms. Table 4.1 compares the root-mean-square value of the noise level in milli-g for the following filtering configurations: original 25 Hz filter (Rice and Spencer 2009), 1 kHz all-pass filter, 1 kHz filter with slow roll-off, and the 1 kHz configurations decimated to 25 Hz. A higher noise level results when no filter is used (all-pass); yet, this is significantly reduced with the use of even minor filtering. Furthermore, the filter reduces considerably the noise aliased back during decimation. Thus, the tradeoff between additional latency and noise filtering is worthwhile.

Table 4.1: RMS Value of Noise Level in mg for Different Filter Configurations.

Sampling Rate	**25 Hz**	**1 kHz**		**25 Hz Decimated**	
Filter Configuration	QF Filtered	All-Pass	Filtered	All-Pass	Filtered
x-axis	0.26	1.29	0.40	1.81	0.71
y-axis	0.29	1.42	0.31	1.74	0.53
z-axis	0.69	1.85	0.76	2.23	1.37

4.2 SHM-SAR: Data Acquisition Hardware Tailored For Control

Although modifications were made to improve the performance of the SHM-A for control, the solution still results in significant latency and only a small interval available for processing due to the high overall sampling rate. Therefore, a new sensing architecture tailored for wireless control applications is necessary. This section will discuss the analog-to-digital converter (ADC) architecture and component selected, evolution of the board layout, and the driver development. The board design, layout, and fabrication discussed in the section were completed with the help of Hongki Jo in the Smart Structures Technology Laboratory at the University of Illinois.

To reduce the latency associated with data conversion, an architecture that can complete the conversion within one sampling interval is selected. As described in Chapter 3, a Successive Approximation Register (SAR) type converter is an ADC of this type and suited for high-resolution applications with medium throughput. Thus, an SAR-type ADC is selected for the data acquisition board tailored for control, which is further referred to as SHM-SAR.

The SAR component selected is the Analog Devices AD7682 (Analog Devices 2008). The AD6782 is a 4-channel, 16-bit charge redistribution successive approximation register ADC that is capable of 250,000 samples per second. Some advantages of the component include: internal low drift reference, selectable one-pole filter, and channel sequencer. The signal-to-(noise + distortion) ratio (SINAD) is relatively high in comparison to equivalent components, which results in a theoretical effective number of bits (ENOB) of 14.16. In addition, the power draw is relatively low, because the device powers down between conversions. Finally, for easier driver development, the AD7682 interfaces with the Imote2 over the SPI bus, which already has timing configurations developed for the Imote2.

4.2.1 SHM-SAR Revision 1.0

The low-latency data acquisition board (SHM-SAR) that interfaces with the Imote2 over the two connectors has been designed around the AD7682. In the initial version of the SHM-SAR, four analog inputs connect to the AD7682 directly or through analog amplifiers depending on a switch, as shown in the block diagram (Figure 4.1). The AD7682 is powered by the Imote2 and digitally interfaces with Imote2 over the SPI interface. The top and bottom of the SHM-SAR is pictured in Figure 4.2.

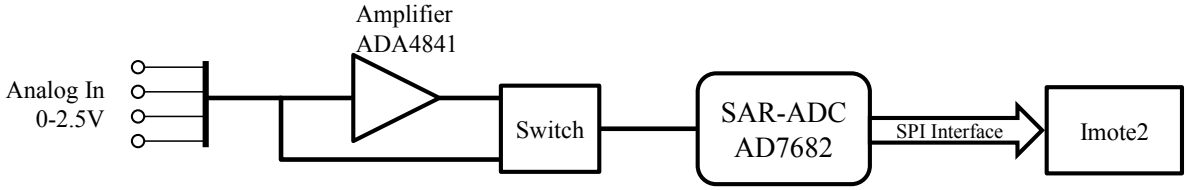

Figure 4.1: Block Diagram of SHM-SAR.

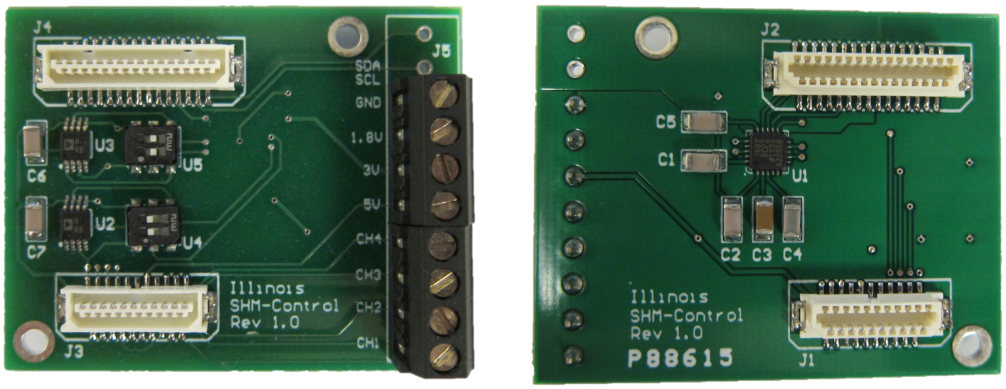

Figure 4.2: SHM-SAR: (left) top (right) bottom.

The signal amplifiers are used to minimize any signal attenuation during conversion; however, because there is a possibility that they can introduce some additional delay, they are user-selectable in the initial revision. In addition, the amplifier can be used in combination with resistors for analog filtering of the data. The amplifiers did not introduce any appreciable delay into the system and improved the performance of the data-acquisition by limiting any signal attenuation prior to conversion.

In addition to component selection, the board layout uses best practices to limit any additional signal noise from the digital channels. As shown in Figure 4.3, a split ground plane is used to isolate the digital and analog components. This division limits any noise that might arise from the quickly alternating digital signals for data transfer over the SPI bus. Through careful board layout, the performance of the AD7482 can be preserved.

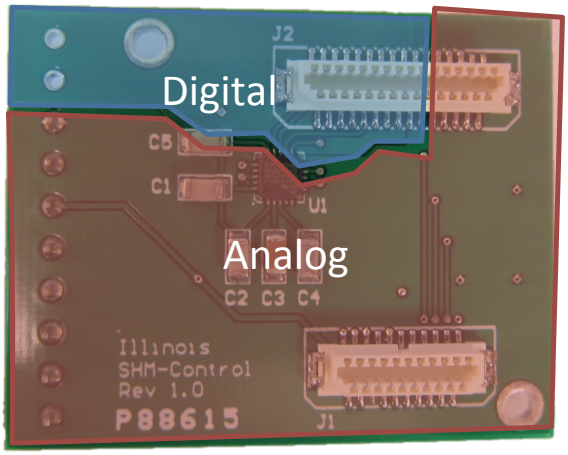

Figure 4.3: SHM-SAR: Split Ground Plane.

4.2.2 SHM-SAR Revision 2.0

To simplify deployment in control systems that use acceleration feedback, a MEMS accelerometer is added to the SHM-SAR for revision 2.0. Either the accelerometer output or external analog signals can be selected using the physical switches placed prior to the ADC (Figure 4.4). Both sets of signals feed through an op-amp to limit any signal attenuation prior to conversion similar to revision 1.0. The main components are highlighted in the top and bottom view of the SHM-SAR rev 2.0 pictured in Figure 4.5.

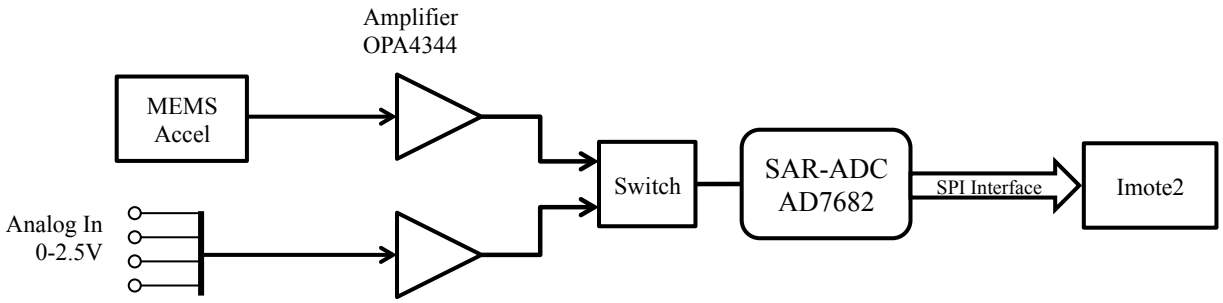

Figure 4.4: Block Diagram of SHM-SAR Revision 2.0.

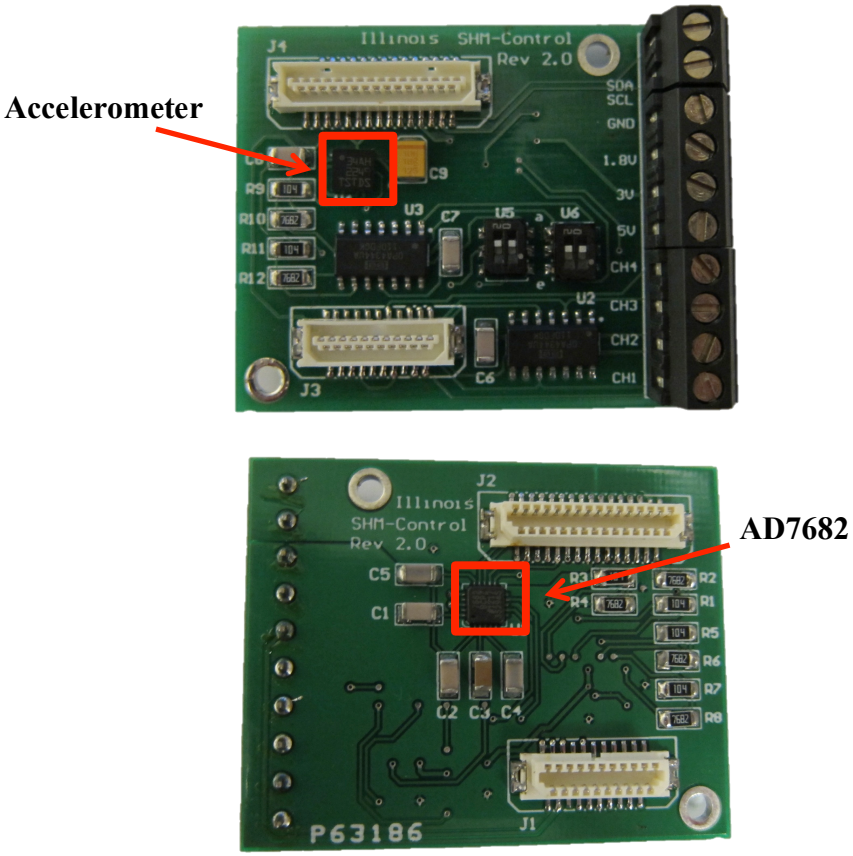

Figure 4.5: Top and Bottom View of SHM-SAR Revision 2.0.

The MEMs accelerometer used is a 3-axis, low power LIS344ALH by ST Microelectronics with a ± 2g range (ST Microelectronics 2008). The properties of the accelerometer are listed in Table 4.2. Given the DC measurement, the z-axis will measure +1g when the board sits level and parallel to the ground. Since the 0g offset is 0.4V above the midrange of AD7682, the acceleration range of the accelerometer on the SHM-SAR revision 2.0 is truncated to -2g to 1.03g. The accelerometer signal could be scaled in future revisions to within the AD7682 input range.

Table 4.2: Accelerometer Properties (ST Microelectronics 2008).

Parameter	Value
Measurement Range	±2g
Sensitivity	0.66V/g
0g Offset	1.65 V
Frequency Range	0 – 1.8 kHz
Noise Density	50 µg/√Hz

4.2.3 Driver Development

Once the DAQ board hardware was developed, the initial driver for sampling using the SHM-SAR was implemented; the goal of the driver is to provide consistent sampling with minimal latency at the user specified rate. The architecture of the driver is presented in Figure 4.6. When sampling is initiated, the ADC outputs at its native sampling rate, which is significantly higher than desired; thus, an alarm time interrupt is fired at the desired sampling interval to initiate sampling and transfer the sample. Sampling is initiated by sending/writing the configuration register, and sampling is completed with the buffer transfer done event. To obtain the most consistent sampling interval, the time for the next alarm is determined when the current alarm fires, as shown in equation (4.2). The alarm is then set when the transfer is complete to ensure that sampling is occurring properly. The approach maintains a consistent sampling interval; but, if there is any shift in time between the alarm firing and the SPI transfer due to other tasks running on the processor, only one off mean sample results due to this architecture. Furthermore, because the SPI interface transfers and receives a buffer simultaneously, two buffers are received until the sample acquired is received across the buffer on the Imote2. To limit the latency, the samples are received in succession at the native sampling rate of the ADC. Thus, the sampling interval is slightly longer than specified, on the order of microseconds, but still consistent.

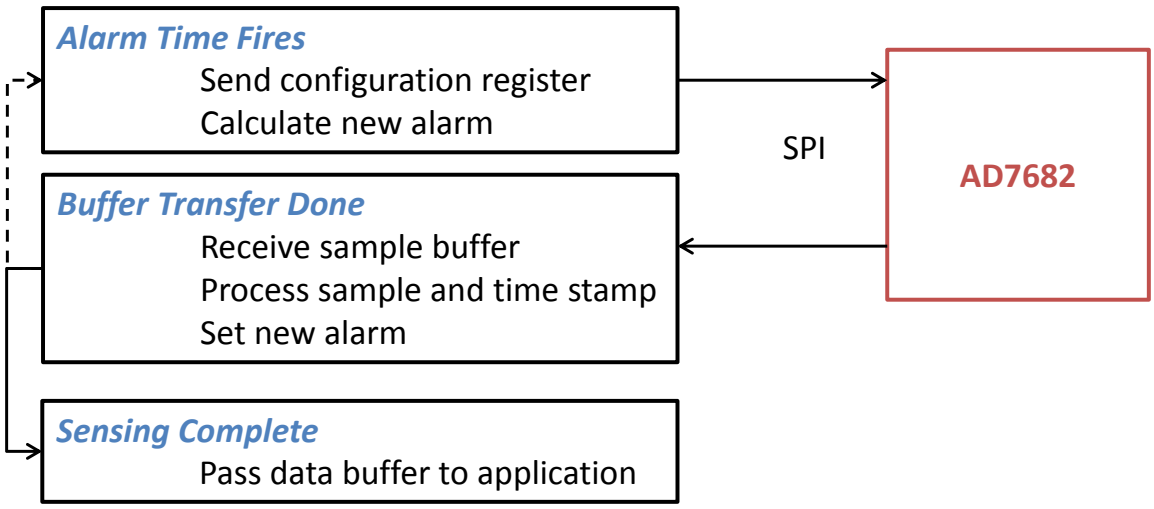

Figure 4.6: SHM-SAR Driver Architecture.

$$t_{alarm} = t_{now} + \Delta_s \text{ , where } \Delta_s \text{ is the sampling interval} \quad (4.2)$$

With this driver architecture, the processing speed of the Imote2 can be increased to provide a more consistent sampling interval and reduce the overshoot of the desired sampling interval that is due to the several samples taken in succession. Figure 4.7 shows the sampling interval in milliseconds over several hundred samples for different processing speeds. The specified sampling rate was 10 Hz, so the sampling interval should be 100 milliseconds. Significant variation in the sampling rate results when operating at 13 MHz, but this variation decreases with the increase in processing speed. In addition, the sampling interval approaches the desired rate as the processing speed increases. However, when the processing speed is increased from 208 MHz to 416 MHz, the performance does not significantly improve, because the bus speed does not increase and relatively little processing is required within the driver. Although

running the processor at 416 MHz provides the sampling rate closest to the desired, any speed above 104 MHz offers good performance; so, ultimately the choice of processor speed depends on the application because the power consumption increases with processor speed (Moinzadeh et al. 2012).

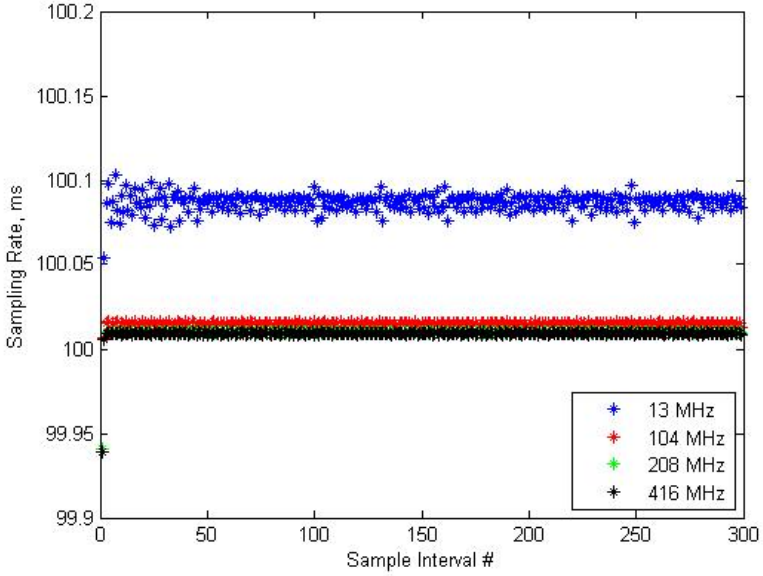

Figure 4.7: Sampling Rate Comparison for Different Processing Speeds.

When sampling multiple channels, the AD7682 uses a multiplexer to sample multiple channels in succession rather than simultaneously sample and hold. If multiple channels are desired, the sequencer will sample each channel in succession and then only the desired channels are saved by the driver and transferred to the application. The SPI transfer continues until all channels are sampled and then a new alarm is set when the final buffer transfer is complete (Figure 4.6). Due to the multiplexer, there is a small sampling delay between channels. The time delay between two neighboring channels is consistently 33 µs. The total delay from channel 1 to channel 4 is 99 µs. This delay is due to both the multiplexer and the multiple transfers across the SPI bus. Since the time offset between channels is consistent, the sampling rate performance for each channel is the same as for a single channel. However, as a result of the delay between channels, the maximum sampling rate for single-channel sampling and multiple-channel sampling are different.

To verify the performance of the driver a known analog signal was input to the SHM-SAR acquisition board and recorded on the Imote2 as shown in Figure 4.8. A 0.5 Hz, 1 volt sine wave centered at 1.25 volts was output from Siglab Spectrum Analyzer and input into the first channel of the SHM-SAR data acquisition board (Spectral Dynamics 2007). The recorded signal is plotted in Figure 4.9. The data acquisition board was able to capture the analog signal accurately. The sampling rate is visibly not exactly 10 Hz, which is a multiple of the sine wave frequency, because the location of the sample points along the signal shift slightly over time. However, the sampling interval is consistent. The slight difference in sampling rate from specified is common; for example, the true sampling of the Quickfilter chip is slightly different due to the filter design.

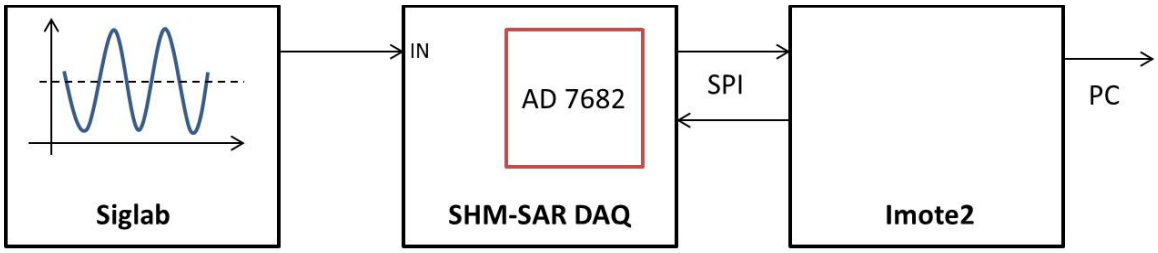

Figure 4.8: SHM-SAR Verification Experimental Schematic.

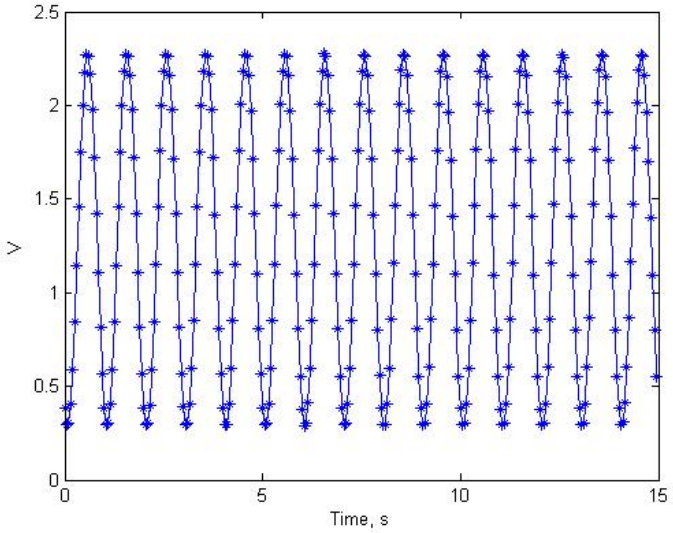

Figure 4.9: SHM-SAR Recorded Signal for Verification Testing.

4.3 SHM-SAR Performance

4.3.1 Maximum Sampling Rate

The maximum sampling rate of the SHM-SAR on the Imote2 is a function of the AD7682, the driver architecture, and the processor and bus speed. The limiting factor in this case is the time for each sample cycle after the alarm has fired (Figure 4.6). The processor and particularly the bus speed will have a significant impact on this interval. At a processor speed of 416 MHz and a bus speed of 208 MHz, the maximum rate when sampling a single channel is 3700 Hz. If multiple channels are sampled, the maximum sampling rate at 416 MHz is 2700 Hz. This difference in the maximum sampling rate is due to the total multiplexer delay of about 100 microseconds. The sampling rate performance of the SHM-SAR should be adequate for most civil engineering applications.

4.3.2 Latency

The central goal of the SHM-SAR board is to reduce the latency due to the data acquisition hardware for control applications. To verify the latency of the two ADC configurations, an experiment similar to the previous verification test was conducted, except the recorded signal was issued as an analog output back to Siglab through the SHM-D2A, which will be discussed in the next section (Figure 4.10). A band-limited white noise was input to the system through

Siglab and the phase between the output and resulting input was used to calculate the time delay. The delay calculated accounts for both the latency of the ADC architecture and the other hardware components in the system.

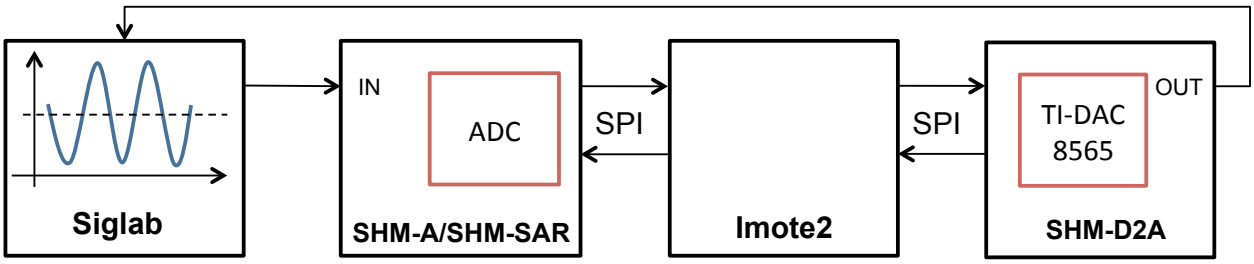

Figure 4.10: DAQ Hardware Latency Experimental Schematic.

The latency of the SHM-SAR acquisition board is significantly lower than the SHM-A, which is essential for wireless control. The time delay for the SHM-A and SHM-SAR acquisition boards are plotted in Figure 4.11 and Figure 4.12, respectively. The plots show the time delay over frequency for various sampling rates. For both cases, the time delay is independent of the sampling rate on the ADC. This result is expected on the SHM-SAR but only results on the SHM-A due to the oversampling/decimating modifications discussed in the previous section. The time delay on the SHM-A is about 30 milliseconds; the majority of this delay is due to the latency of the Quickfilter ADC architecture. On the other hand, the time delay on the SHM-SAR is about 200 microseconds, which is significantly lower and can be neglected in future control design. In this case, the other hardware components including the SPI transfers and processing contribute to a larger proportion of the delay. Overall, due to the selection of the ADC architecture, the SHM-SAR is successfully tailored to control applications.

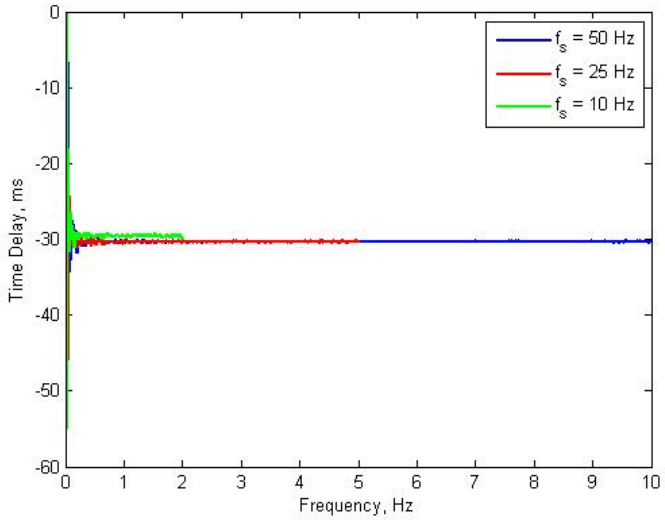

Figure 4.11: Time Delay Experimentally Determined for SHM-A.

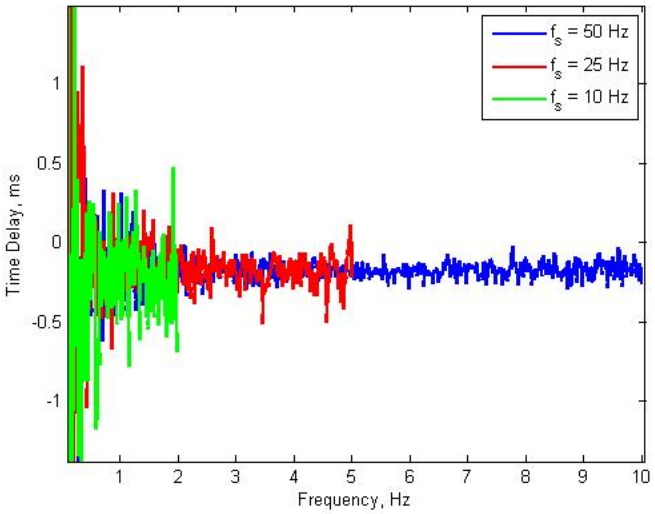

Figure 4.12: Time Delay Experimentally Determined for SHM-SAR.

4.3.3 Resolution

The effective resolution of the as-built SHM-SAR board indicates any additional noise in the hardware due to the layout or driver architecture when compared with the specification. The equivalent number of bits is calculated using the signal-to-(noise + distortion) ratio (SINAD). However, because ensuring the input signal lies on a spectral line is a challenge, spectral leakage in the power spectrum makes this result highly variable. As a result, the calculated signal-to-noise ratio is used to determine the effective resolution according to:

$$SNR = 20\log\left(\frac{FSR}{N_{rms}}\right)$$
$$ER = \frac{SNR - 1.76}{6.02} \tag{4.3}$$

where FSR corresponds to the full-scale range in volts, N_{rms} is the rms noise value in volts, and ER is the effective resolution in bits.

To determine the signal-to-noise ratio, a zero volt signal is applied to the SHM-SAR external input. The zero volt input is generated by dSpace (Model RT1103). The external input is sampled by the SHM-SAR mounted on an Imote2 at four different sampling rates: 40, 100, 1000, and 2000 Hz. The rms noise value calculated at 2000 Hz is 7.9 x 10^{-4} V and the resulting effective resolution is 11.4 bits. This resolution is lower than the specified 14.16 bits in the data sheet (Analog Devices 2008). The difference in resolution is likely due to aliasing on the SHM-SAR, since no filtering is used. Figure 4.13 compares the PSD of the sampled signal for each sampling rate. The noise floor rises as the sampling rate lowers, whereas the noise floor would remain constant if anti-aliasing filters were utilized. Similarly the rms noise levels for each sampling rate are the same, so the energy in the signal is constant (Table 4.3). If filtering is used, the effective resolution will increase for lower sampling rates.

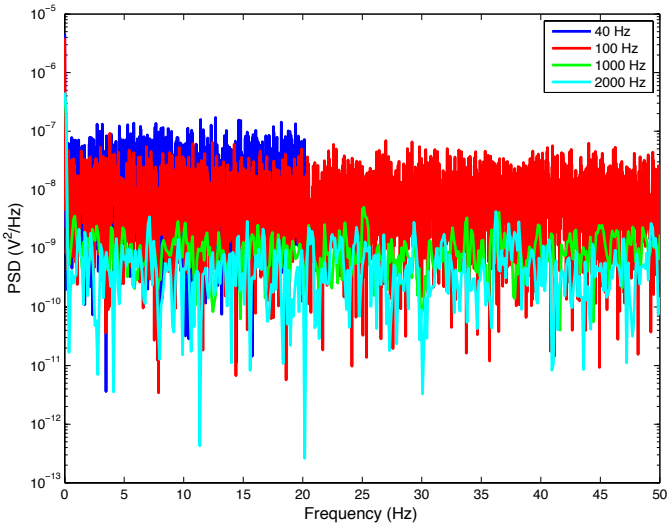

Figure 4.13: Comparison of the Noise PSD for the SHM-SAR at Different Sampling Rates.

Table 4.3: RMS Noise Level for the SHM-SAR at Different Sampling Rates.

Sampling Rate (Hz)	RMS Noise Level (V)
40	7.4×10^{-4}
100	7.5×10^{-4}
1000	7.6×10^{-4}
2000	7.9×10^{-4}

4.3.4 Accelerometer Performance

The initial tests of the onboard accelerometer compared dynamic measurements with a wired accelerometer and evaluated the static calibration of the sensor. The accelerometer offset and sensitivity were determined using the static calibration method outlined in Jang and Rice (2009). The 0g offset value is initially measured and then the +1g and -1g values are measured to determine the sensitivity in LSB/g. The SHM-SAR board was then mounted on the Imote2 and affixed to the second story of the flexible structure addressed in Chapter 8. The structure was then excited by a band-limited white noise. The SHM-SAR acceleration measurement was compared with a reference capacitive accelerometer both sampled at 725 Hz (PCB Model 3701G3FA3G, PCB Piezotronics 2013). The time domain response comparison is plotted in Figure 4.14. The two signals match closely; so, the static calibration technique is adequate. However, the magnitude of the SHM-SAR signal is occasionally larger. This discrepancy in the signals is due to the higher noise density for the SHM-SAR board.

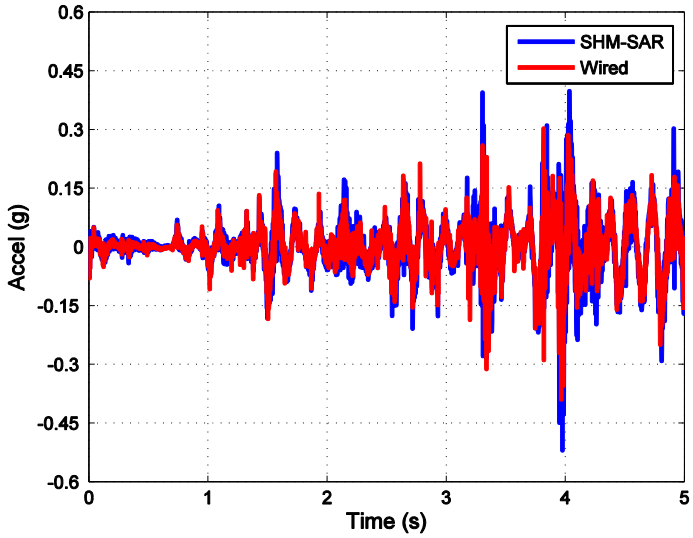

Figure 4.14: Time-domain Comparison of SHM-SAR and Wired Accelerometer Measurements.

To further evaluate the noise density and rms noise value for the SHM-SAR accelerometer configuration, a 0g signal is sampled at 1000 Hz. The PSD of the signal is plotted in Figure 4.15. The resulting rms noise floor is 2.9 mg, which is higher than the SHM-A configuration. Similar to the resolution analysis in section 4.3.3, the additional noise in the system is due to aliasing.

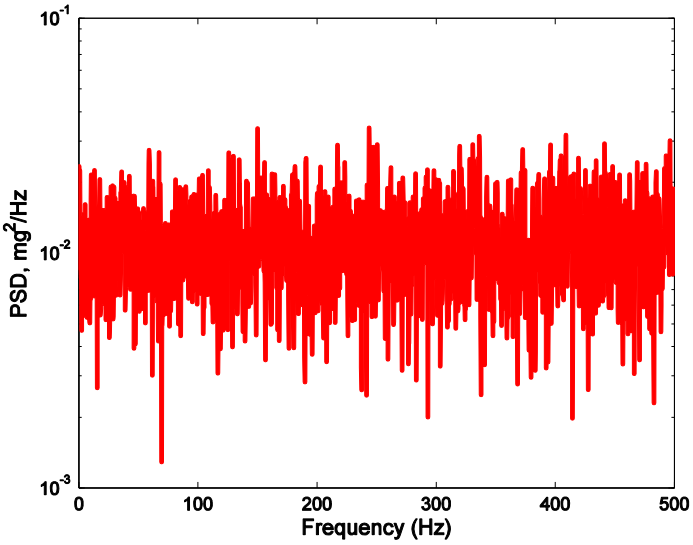

Figure 4.15: PSD of 0g Signal for SHM-SAR Onboard Accelerometer.

An analog filter is implemented to reduce the noise in the accelerometer measurements. The internal resistance of the accelerometer is used with a capacitor and the op-amp to produce a single-pole low-pass analog filter (Figure 4.16). The cutoff frequency filter is determined by

$$f_c = \frac{1}{2\pi \cdot R_{out} \cdot C_{load}} \tag{4.4}$$

The nominal internal resistance, R_{load}, is 110 kΩ. However, the internal resistance can vary by as much as ±20%. Therefore, there can be a significant phase mismatch between two different measured accelerometers' signals. In addition, a filter will introduce additional delay in the system and the roll-off of a single-pole filter is very slow. To balance these tradeoffs, a 3.3 nF capacitor is used for a cutoff frequency of about 438 Hz. Figure 4.17 shows the maximum phase mismatch and the time delay introduced by the filter. The rms noise determined for the filtered signal is 1.8 mg, which is about 38% less than the unfiltered value. Therefore, the reduction in noise outweighs the small delay introduced and the possible phase mismatch for this design. If a lower cutoff frequency was desired, the possible phase mismatch and time delay would be much larger. In that case, the on-board accelerometers should be used in any model development to account for the phase mismatch and additional delay in the system due to the filter.

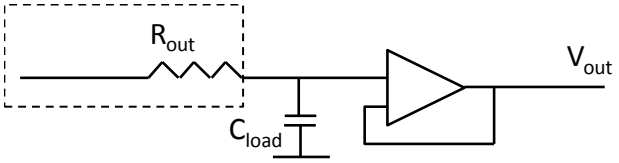

Figure 4.16: Analog Single-Pole Low-Pass Filter Using Internal Resistance of the Accelerometer.

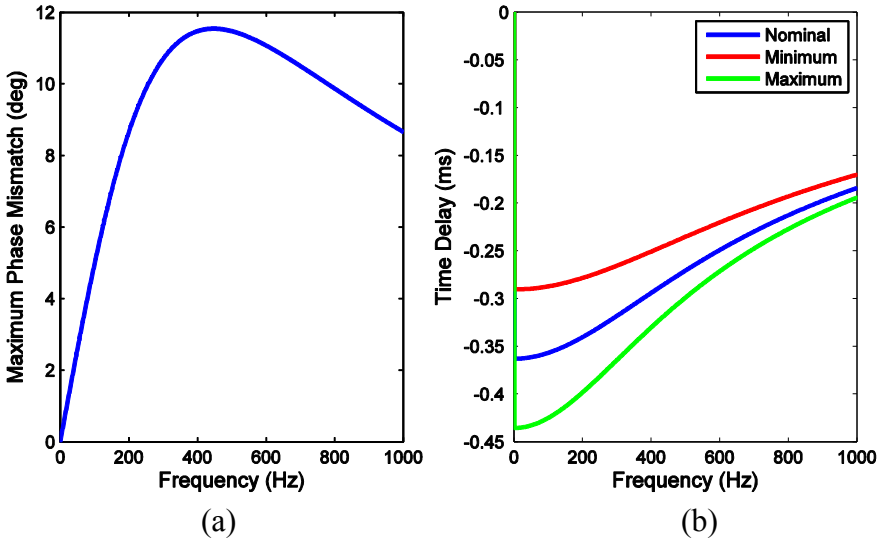

Figure 4.17: (a) Maximum Phase Mismatch and (b) Time Delay Introduced by RC Filter.

4.4 SHM-D2A: Actuation Interface for Imote2

The other essential hardware component for wireless control is an actuation interface. The SHM-D2A board converts a command calculated on the Imote2 to an analog output voltage. The main considerations for the actuation interface are the required voltage output, resolution of the output, and speed of conversion. Therefore, as described in Chapter 2, the most essential component is the digital-to-analog converter (DAC).

An SHM-D2A actuation board that interfaces with Imote2 over the two connectors is built around the TI-AD8565 (Texas Instruments Inc. 2007). The four-channel DAC has 16-bit resolution, which is equivalent to the data acquisition board; thus, no resolution is lost by the actuation interface. The component has a short settling time of 10 microseconds, which offers comparable performance to the SAR-type ADC for medium throughput applications. In addition,

the DAC offers a low-power stable internal voltage reference of 2.5V. This clean, stable voltage reference is an attractive alternative to the voltage supplies offered by the Imote2. Finally, the component can use an SPI interface for digital operation, which simplifies driver development.

Additional hardware to alter the voltage output range is not utilized on the SHM-D2A because the voltage output is considered adequate for a variety of applications and additional components will add to the current draw of the device. A block diagram and image of the actuation board is provided in Figure 4.18 and Figure 4.19, respectively. The desired output is transferred over the SPI interface to the TI-AD8565, which then outputs the corresponding analog voltage. The driver, originally developed by Ralph Kling and then modified, uses the standard SPI driver routines offered for the Imote2 in TinyOS. A desired voltage and corresponding channel is written over the SPI bus and then output as an analog signal. The voltage is held until changed or powered-down. At power-up the voltage on all channels is initialized to zero volts.

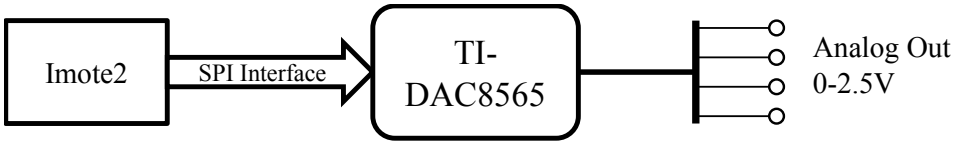

Figure 4.18: Block diagram of SHM-D2A.

Because the Imote2 offers two SPI interfaces, the actuation board can easily be combined with a data acquisition board by stacking them. Figure 4.19 illustrates the SHM-D2A stacked on the SHM-A and Imote2 for combined sensing and actuation, as would be used in wireless control.

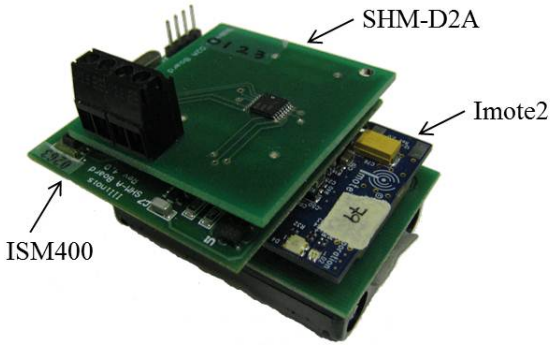

Figure 4.19: SHM-D2A stacked with Data Acquisition Board and Imote2.

4.5 Summary

Data acquisition hardware tailored for structural health monitoring can introduce significant latency due to oversampling and digital filtering; therefore, a low-latency data acquisition board for control applications is developed for the Imote2. The board, centered on a SAR-type ADC, significantly reduces the latency in the system due to the hardware from 30 ms to 200 μs. An on-board accelerometer offers easy application of acceleration feedback for control and simplified implementation of a single-pole RC filter to limit aliasing. The control loop is completed with an actuation interface. The SHM-D2A offers comparable specifications to the SHM-SAR. The combination of the two boards offers low-latency performance for control applications.

REAL-TIME WIRELESS DATA ACQUISITION

High-throughput, real-time wireless data acquisition is an essential software component for wireless control. In this chapter, the implications of hardware and software limitations on the implementation of real-time sensing are discussed and addressed in the communication protocol and application design for real-time data acquisition. The initial application framework is then expanded to provide high-throughput, near-real-time wireless data acquisition for applications requiring a larger network size. Two near-real-time approaches are considered and evaluated based on their resulting network size, sampling rate, and data delivery reliability. In near-real-time data acquisition, the samples are only available on the base station after a latency of several sampling intervals. Real-time data acquisition is required in applications such as wireless structural control. Structural health monitoring applications are less sensitive to latency for real-time visualization of the response and thus near-real-time data acquisition suffices.

5.1 Implications of Hardware and Embedded Software on Real-Time Data Acquisition

The TinyOS operating system design, while useful for embedded applications, makes the real-time scheduling and control required for real-time wireless data acquisition challenging. This section will outline how the event-driven concurrency model of TinyOS along with standard hardware limitations impacts real-time sensing.

5.1.1 Sampling Rate Limitation

The FIFO task queue and lack of priority-based scheduling limit the sampling rates possible for real-time data acquisition. Each data sample is passed through to the application from the driver in an event generated by an interrupt handler, which is similar to posting a task. Any processing tasks including, calculating the global time stamps, temperature correction, and sending must occur before the next data sample is passed. Otherwise, the task queue will slowly fill and the real-time nature is lost. Thus, the sample interval is limited by the total time required to process and send.

5.1.2 Communication Time

To improve communication reliability, the radio utilizes a clear channel assessment to ensure that the wireless channel is free prior to transmitting. Thus, multiple nodes transmitting at the same time can increase communication time. Furthermore, because the radio waits a random back-off time prior to reassessing the channel, the time required to send while multiple nodes are transmitting is not consistent. Therefore, predicting the sending time, which is important for determining the sampling rate, is challenging.

5.1.3 Sensing Offset

The sensing approach, as well as variation in hardware start-up times, introduces an offset between the desired and actual start of sensing. A desired sensing start time is specified when the sensing task is posted; however, sensing does not begin at this exact specified time. Nagayama et al. (2009) explains that while performing all sensing and time stamping within the interrupt context could be used to gain more accurate timing than posting a task, firing an interrupt with a computationally intensive interrupt handler (transferring data over the SPI bus, decoding and storing it, and adding a timestamp) at a high frequency is unreasonable in the TinyOS concurrency model. Furthermore, variation in hardware initialization times would result in a delay nonetheless.

As a result, the sensing approach, illustrated in Figure 5.1, accepts relative uncertainty in the start time for sensing. When the driver initializes, sensing begins; however, samples are not stored and passed to the application until they are within a sampling interval of the desired start time, t_{start}. This offset is non-trivial and, due to variation in processing of the sensing task and the hardware initialization time, is non-deterministic. In local data logging approaches, this sensing offset is recorded and accounted for during post-processing by resampling the data prior to transmission (TinyOS 2006).

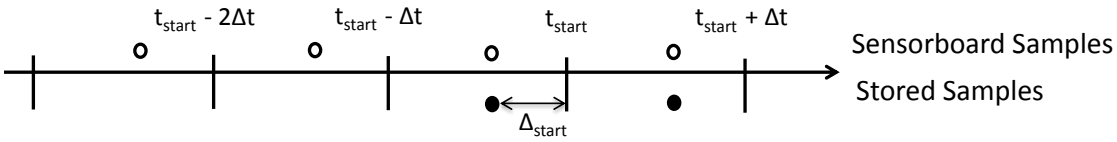

Figure 5.1: Sensing Approach

However, the strict timing of real-time transmission requires accounting for this offset during sensing in the application design. Although time synchronization aligns the global clocks among the nodes, the sampling times are not consistent due to this offset. Thus, any scheduling among nodes based on sample ready events will not be aligned. Furthermore, the time stamps of the data must be transmitted as well, so the offset can be accounted for later in resampling, if desired.

5.2 Real-time Data Acquisition for Real-Time State Knowledge

The sampling rate limit, sensing approach, and communication latency limitations due to the design of wireless sensor hardware and TinyOS described in the previous section must be addressed in the application design. Consequently, unlike wired systems, implementation of real-time wireless data acquisition requires addressing the tradeoff between performance, including network size and sampling rate, and reliability. The resulting wireless data-acquisition service, which could be applied to structural control or health monitoring applications, and its performance will be presented in this subsection.

5.2.1 Application Design

Given the FIFO scheduling of TinyOS, minimizing the time for each element of a sampling interval and providing a consistent time to send is necessary for determining the maximum sample rate possible. Due to the random communication latency when multiple nodes send at the

same time, a scheduled communication approach is utilized. Furthermore, within this framework, the amount of data returned to the gateway nodes is minimized to the 8-bit node ID, 4 channels of 16-bit data, and a 32-bit timestamp for accurate reconstruction of the data. Thus, the total packet payload is limited to a minimum of 14 bytes.

Communication Protocol

The common time-division multiple access (TDMA) protocol is implemented to allow multiple leaf nodes to communicate with a single receiver, or gateway node, by transmitting in different time slots. A TDMA protocol, illustrated in Figure 5.2, permits only one node to send at a time; thus, allowing the communication time to be more readily determined due to the absence of contention and back-off delays. The complete sensing interval is broken down into three components: processing on the leaf node (or remote processing), send time, and processing on the gateway node (or local processing). The processing on the leaf node includes any handling of the sensor data and time stamping. The send time consists of the time from calling send on the remote node until the completion of packet transmission. Finally, processing on the local node consists of extracting and decoding the data from the packet on the gateway node and transferring it to an internal buffer.

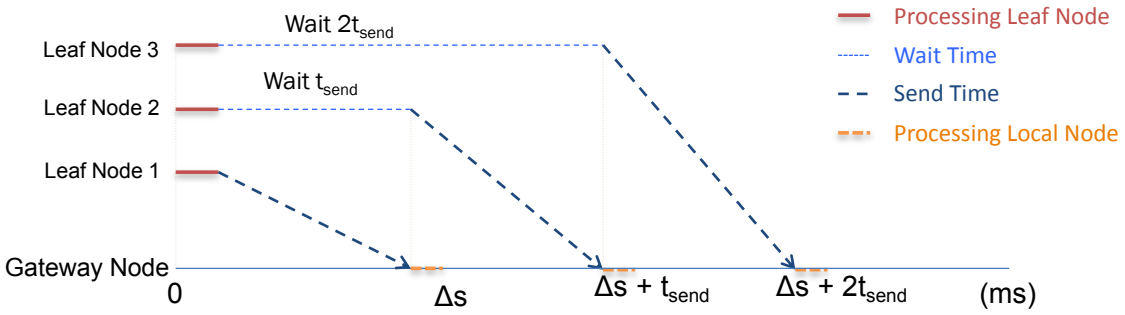

Figure 5.2: TDMA Communication Protocol

Because a reliable communication protocol involving acknowledgements and resends may take an undetermined amount of time, a generic, or unreliable, communication scheme with only a cyclic-redundancy check (CRC) for packet error detection is used. Thus, if bit errors are found within the packet, the data packet is dropped and no retransmission occurs. While this *GenericComm* scheme does not address packet loss, a relatively consistent send time is possible (TinyOS 2006). Furthermore, a TDMA protocol reduces the loss of packets due to collisions by limiting the likelihood of multiple nodes transmitting at the same time. While collisions are only one of numerous causes of packet loss, including path loss and antenna orientation, a TDMA protocol can help to improve reliability (Shankar 2002).

Due to hardware variations among Imote2s and the event driven nature of TinyOS, the time required for sending and processing will vary both among sensor nodes, as well as on an individual node. Thus, a timing analysis was conducted on several sensors nodes to assess the time required for each step in a single sampling interval; remote processing, send time, and processing on the gateway node are recorded for 500 samples over 4 trials for several nodes. A cumulative distribution function of the discrete results was calculated for each step, as shown in Figure 5.3, and the 97^{th} percentile values were selected to ensure that each step in the sampling interval typically occurred within the time allotted. The timing analysis results are given in Table 5.1. For the processing steps, the variation in time required to complete the tasks is small;

however, the variation in sending time is significant. Thus, while selecting the 97th percentile value decreases the maximum possible sampling rate, the larger send time will improve reliability by guaranteeing that most sends will occur within the time allotted. Ultimately, the combination of the processing and sending times on the leaf node are used to calculate the delay to be employed in the TDMA scheme.

Table 5.1: Timing Analysis for Steps in Wireless Data Acquisition.

	Processing Leaf (ms)	**Sending Leaf (ms)**	**Processing Gateway (ms)**	**Total Time (ms)**
97th Percentile	0.50	6.55	1.5	8.55
Mean	0.37	4.17	1.27	5.81
Standard Deviation	0.09	1.48	0.20	1.77

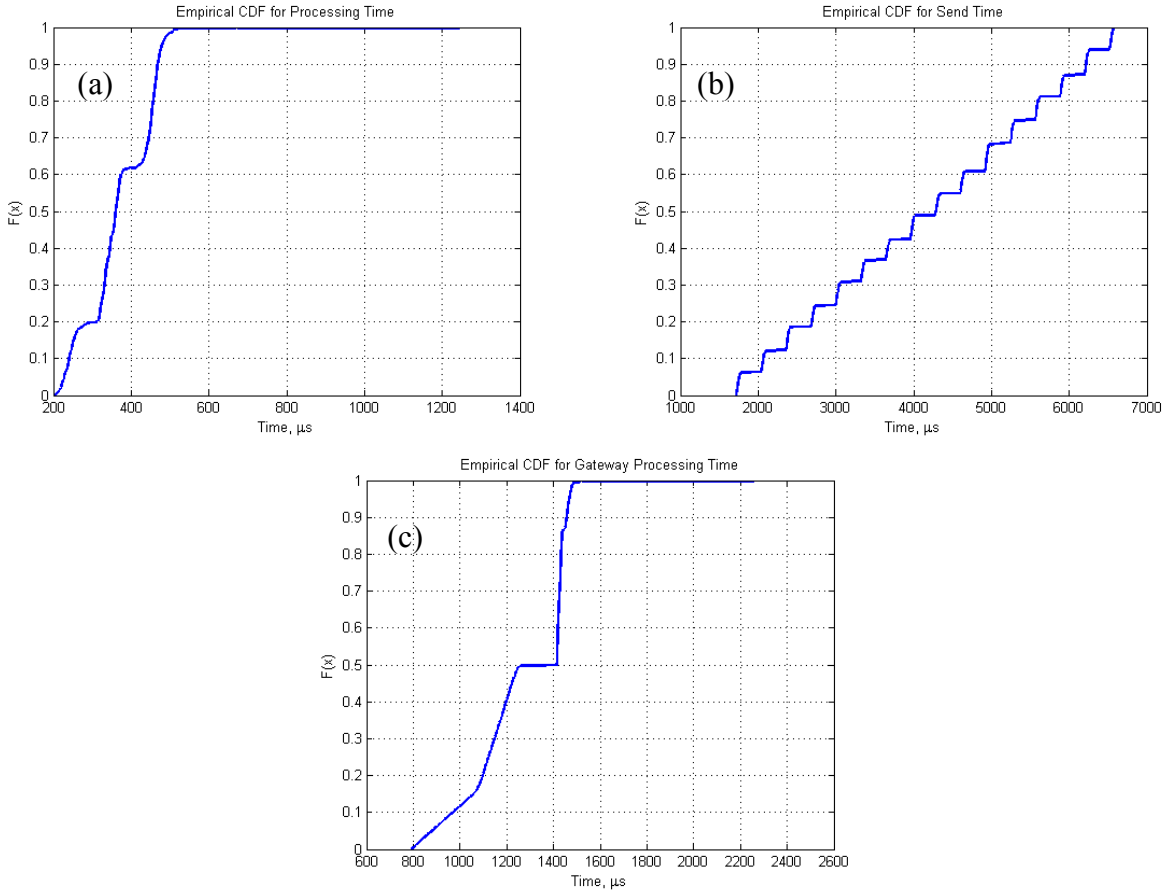

Figure 5.3: Empirical CDF for (a) Remote Processing Time, (b) Send Time, (c) Gateway Processing Time.

In addition, the variable processing speed of the Imote2 is utilized to reduce the time required for each step. The speed is increased from the normal operating speed of 13 MHz to 104 MHz to achieve this performance. Because the processing time given in Table 5.1 is so much smaller than the sending time, the processing speed is not increased to the maximum of 416 MHz due to the significantly greater power consumption at higher speeds (Miller et al. 2010; Moinzadeh et al. 2010).

The variations in the cumulative distribution functions (Figure 5.3) also highlight the effects of underlying processes on the sensor nodes. The staircase pattern of the empirical CDF of the send time can be attributed to the random back-off time in the wireless communication protocol to limit collisions and bandwidth contention. The discontinuities in the processing CDFs are likely due to background tasks executed prior to the completion of packet transmission by the non-preemptive FIFO scheduler used in TinyOS. Since both radio and memory management tasks are included in the gateway processing, the time variation is larger.

Sensing Offset

The TDMA communication protocol assumes that all nodes are sensing at the same time; however, as discussed in Section 5.1.3, the exact time of sensing for each node is offset. This offset, which is not known prior to the start of sampling, must be accounted for in the communication scheduling to ensure that sends do not overlap despite using a TDMA approach. Furthermore, the time stamp must be returned with the data to account for this offset in resampling, which increases the packet payload for each sample.

5.2.2 Application Flowchart

The complete application requires combining accurate time synchronization and reliably sent commands to start sensing with this scheduled communication approach. Figure 5.4 illustrates the combination of these services into the overall program flow. At the start of the application, the user inputs the sensing parameters including the channels, number of samples, sampling rate, and leaf nodes for which data is to be acquired. These parameters are sent to the leaf nodes reliably to initialize the application. Time synchronization then occurs to ensure the leaf node's clocks are aligned, which is necessary to provide reasonable alignment in sensing and allow the tight scheduling of sends in the TDMA protocol. After synchronization a message for calculating the appropriate delay in sending for the communication protocol is sent reliably to the responsive nodes. The two initialization messages are sent reliably, because they are essential to successful completion of the application and, as such, more time is allotted for these messages. Once sensing begins, the continuous sensing and sending protocol starts and continues until the leaf nodes have acquired and sent all the desired number of samples.

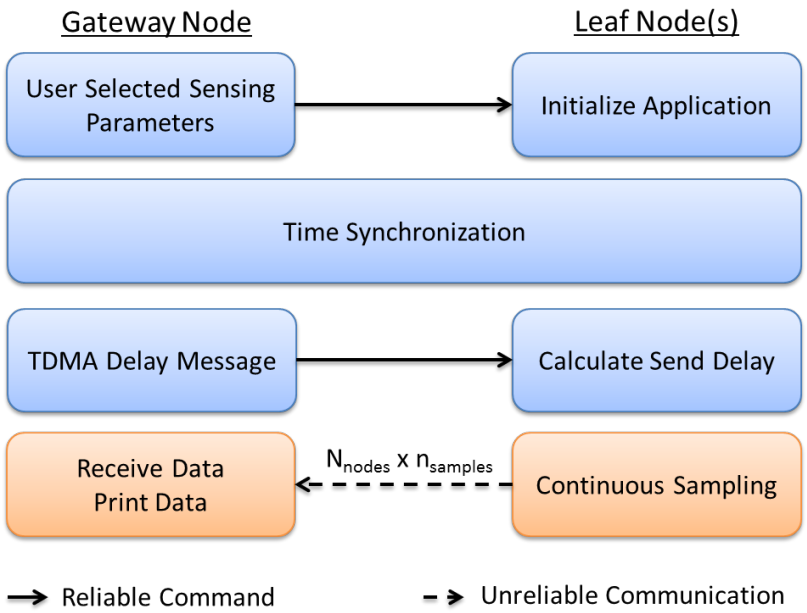

Figure 5.4: Overall Application Flowchart.

Because the continuous sampling component is the central part of real-time wireless data acquisition, it is presented in more detail in Figure 5.5. When a sample is passed from the sensor board driver to the application, a sample ready event is signaled. Next, the time for a send timer interrupt is calculated based on the time the sample is received, the start of sensing offset, and the sending delay determined for the TDMA scheme. If the time calculated is greater than one sampling interval due to the sensing offset, then it must be accounted for when setting the timer interrupt and determining the appropriate packet to send when the interrupt fires. A timer interrupt is used to signal the send rather than the default TinyOS timer that uses task posting, as accurate scheduling is required for the TDMA scheme. Once the interrupt is set, the sample is processed. The time stamp is calculated and temperature correction of the acceleration data is applied if necessary. After the interrupt is fired, the selected radio packet is sent unreliably to the gateway node.

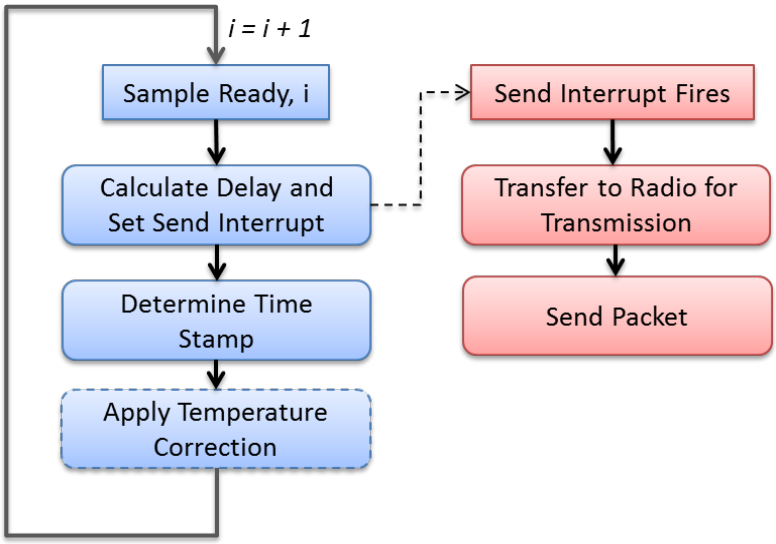

Figure 5.5: Continuous Sensing Flowchart for Leaf Node.

The interrupt time is calculated and set prior to processing the data, because the time required for processing has some variation, as mentioned previously; as such, the time for processing is encompassed in the delay for the TDMA scheme. Thus, the total sending delay determined for the TDMA scheme is based on how many nodes are in the system and the total time required to process and send the packet. Including the number of nodes and the sending/processing times in the TDMA approach makes this approach unique from of other MAC-layer protocols, which cannot account for these variables (van Hoesel and Havinga 2004; Gobriel et al. 2009).

5.2.3Application Performance

Given the application design and timing analysis, the resulting performance of real-time wireless data acquisition in terms of network size, sampling rate, and throughput, when only sensor data is considered, is provided in Table 5.2. Due to the TDMA scheme, the maximum sampling rate decreases as the number of sending nodes in the network increases. However, the maximum data throughput stays relatively unchanged due to the increase in network size.

Table 5.2: Performance of Real-time Wireless Data Acquisition.

Number of Nodes	Sampling Rate (Hz)	Max. Data Throughput (Kbps)
1	115	7.36
2	60	7.68
3	40	7.68

The maximum data throughput is lower than the theoretical maximum available on the radio band due to the TDMA approach and FIFO task scheduling of TinyOS. For example, if the entire radio packet is used during transmission, including the preamble, headers, maximum data size, and footer as shown in Figure 5.6, the maximum data throughput achievable using a timeslot length of 7.1 ms for this TDMA scheme is about 149 Kbps. However, if only the

maximum possible data payload is considered in the throughput calculations, the maximum data throughput possible further reduces to about 125 Kbps. In our specific application, due to the small payload size, the data throughput is significantly lowered from the maximum possible. Therefore, while the TDMA scheme and scheduling communication around sensing offers a solution, it is at the cost of significant performance.

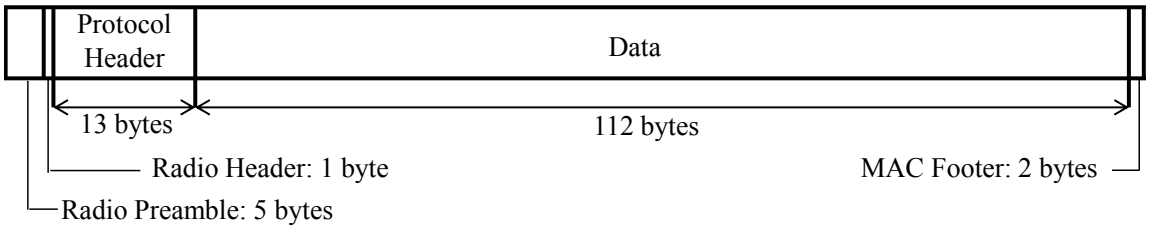

Figure 5.6: Packet Layout (TinyOS 2006).

5.3 High-Throughput Near-Real-Time Data Acquisition

For applications that only require near-real-time sensing, such as structural health monitoring, the performance of real-time wireless data acquisition discussed in Section 5.2 can be significantly improved by buffering samples. The performance improvement is seen in the network size and associated sampling rate and data throughput. However, a tradeoff results between the latency, network size, and sampling rate, because they are directly related to the number of samples buffered prior to sending. As such, the design and performance of two different buffering sizes are presented: 3-sample buffer and a 9-sample buffer.

5.3.1 Application Design

The application design for a buffered approach mirrors the design for real-time data acquisition presented previously. A scheduled communication approach is still used; however, it is expanded to utilize the advantage of buffering of multiple samples within one packet prior to sending. Within this framework, the data returned to the gateway includes the desired number of buffered samples, which is comprised of 4 channels of 16-bit sensor data, an associated 32-bit time stamp, and an 8-bit node ID. Thus, the payload when buffering three and nine samples is 38 and 110 bytes respectively. A maximum of nine buffered samples is considered, because the maximum data payload of one radio packet dictated by the IEEE 802.15.4 protocol and TinyOS 1.x standard MAC protocol is 112 bytes (see Figure 5.6). The three sample buffer offers an increase in network size over the previous approach with a relatively small increase in payload size, which will slightly decrease the maximum sampling rate as discussed later.

Communication Protocol

Similar to the previous design, a scheduled TDMA communication protocol is used to allow multiple leaf nodes to communicate with one gateway node in a consistent and more reliable manner. However, buffering of multiple samples prior to sending allows the number of nodes in the network to increase for a comparable sampling rate. As shown in Figure 5.7, a staggered TDMA approach is used based on the number of samples buffered. For example, when three samples are buffered, three sampling intervals can be used for sending. Thus, the TDMA approach illustrated in Figure 5.2 can be applied to all three sampling intervals.

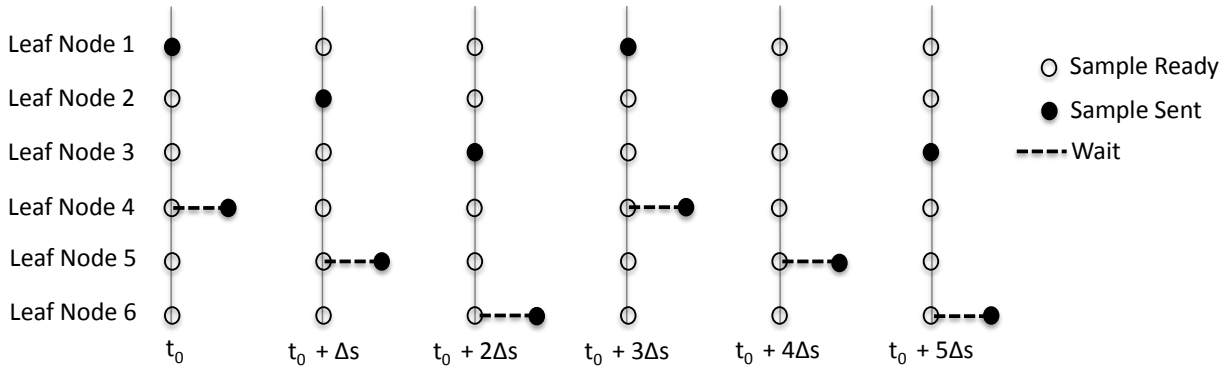

Figure 5.7: Staggered TDMA Protocol for 3-Sample Approach with 6 Leaf Nodes

As was done previously, a timing analysis was conducted on several sensor nodes, in which the time for each step was determined for 250 samples over 9 trials for several nodes. A cumulative distribution function of the discrete results was calculated for each step and the 97th percentile values were selected for reliability. The timing analysis results for both approaches are given in Table 5.3.

Table 5.3: Timing Analysis for TDMA Approach with Buffered Samples – 97th Percentile Values.

Approach	Processing Leaf (ms)	Sending Leaf (ms)	Processing Gateway (ms)	Total Time (ms)
3 – sample	0.4	7.7	2.3	10.4
9 – sample	0.4	10.1	2.0	12.5

While the buffered approach allows the size of the network to increase, the resulting sample rate will decrease due to the additional time required for each step of a sampling interval: remote processing, remote send, and local processing. The difference in processing time on the remote node is negligible for the different approaches, since the sample processing is the same. However, the sending time increased for the 3-sample buffer and again for the 9-sample buffer due to the larger packet payloads. This increase will have the most significant impact on the maximum sampling rates possible.

5.3.2 Application Framework

Similar to real-time data acquisition, the near-real-time approach requires tight time synchronization and reliable commands to start sensing in combination with the staggered communication protocol. Thus, the general application flowchart matches that presented in Figure 5.4. The main difference in the approaches is the calculation and setting of the send timer interrupt. Because samples are buffered, the send interrupt is only set every *n* samples when an *n*-sample buffer is used. Furthermore, while the interrupt is based on the same calculation of current time, sensing offset, and TDMA send delay, accounting for this calculated time being greater than one sample period is made simpler by the buffering of multiple samples.

5.3.3 Application Performance

Near-real-time wireless data acquisition can significantly improve performance in terms of network size and associated maximum sampling rate and throughput; however, a tradeoff results between the network size, sampling rate, and latency due to the number of samples buffered. Furthermore, an increase in the number of samples buffered, means a higher number of samples will be lost if a packet is dropped using unreliable communication. The resulting performance of the application in both sampling rate and reliability is presented in this section.

Sampling Rate and Throughput

Given the timing analysis presented in Table 5.3 and the application design, the resulting performance in terms of network size and associated maximum sampling rate and throughput is presented in Table 5.4 and Table 5.5. The resulting network size and data throughput is significantly improved over the previous approach by buffering samples. Furthermore, the drop in the maximum possible sampling rate for the network is not significant considering the large increase in network size. This large increase in network size and associated packet payload is the biggest contributor to the increase in data throughput.

Table 5.4: Application Performance for 3-Sample Buffer Approach.

Number of Nodes	Sampling Rate (Hz)	Max. Data Throughput (Kbps)
1 – 3	100	19.2
4 – 6	50	19.2
7 – 9	35	20

Table 5.5: Application Performance for 9-Sample Buffer Approach

Number of Nodes	Sampling Rate (Hz)	Max. Data Throughput (Kbps)
1 – 9	75	43.2
10 – 18	40	46
19 – 27	25	43.2

Data Delivery Performance

Because an unreliable communication protocol is used in combination with a timed communication scheme, some data loss is expected. However, the packet loss due to the application design and chosen sending delays is expected to be minimal. Because multiple samples are buffered into one packet, a lost packet corresponds to more lost data and thus is a greater concern and needs to be investigated.

To determine the data delivery performance of near-real-time data acquisition application, the application was evaluated in a near perfect communication environment. The sensor nodes with a mix of onboard and external antennas were placed evenly spaced in an open environment with a clear line-of-sight to the gateway node. The 3-sample approach was tested in an outdoor parking garage on the University of Illinois campus as pictured in Figure 5.8(a). Due

to inclement weather, the 9-sample approach was conducted in a classroom in the Newmark Civil Engineering building on the university campus as shown in Figure 5.8(b). Five trials of continuous data acquisition of several hundred samples at key sample rates for each approach and network size were conducted. Two different node configurations for each network size were considered. The complete testing matrix is provided in Table 5.6. Fewer samples were taken in each trial of the 3-sample approach in order to prolong battery life over the tests; whereas, the nodes in the 9-sample approach were powered with USB.

(a)

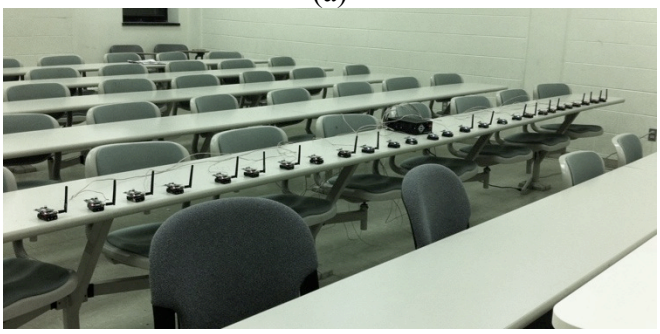

(b)

Figure 5.8: Test Set-up for (a) 3-Sample and (b) 9-Sample Approach.

Table 5.6: Testing Matrix for Data Delivery Performance.

	3-Sample Buffer	**9-Sample Buffer**
# of Samples	500	1000
Sampling Rates (Hz)	10, 25, 35, 50, 100	10, 25, 40 75
Network Sizes	3, 6, 9	9, 18, 27

The data delivery results for each approach are given in Figure 5.9 and Figure 5.10, respectively. The average reception rate gives an indication of data loss, because it accounts for data sample loss not packet loss. In general, minimal data loss was observed. The average reception rate for the 9-sample approach was slightly lower than the 3-sample approach, which is expected as each dropped packet contains more samples; however, the average reception rate is higher than 97%, which was the selection cutoff for timing parameters.

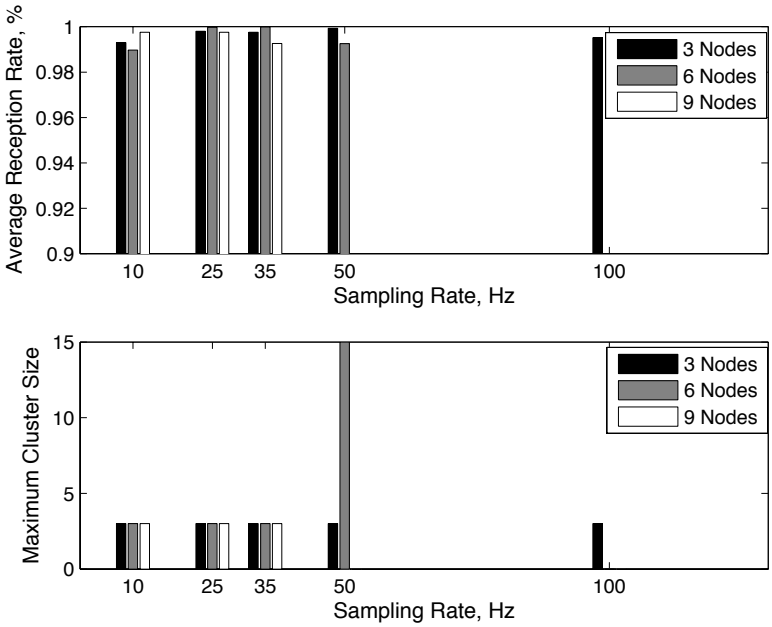

Figure 5.9: Data Delivery Performance Results for 3-Sample Approach.

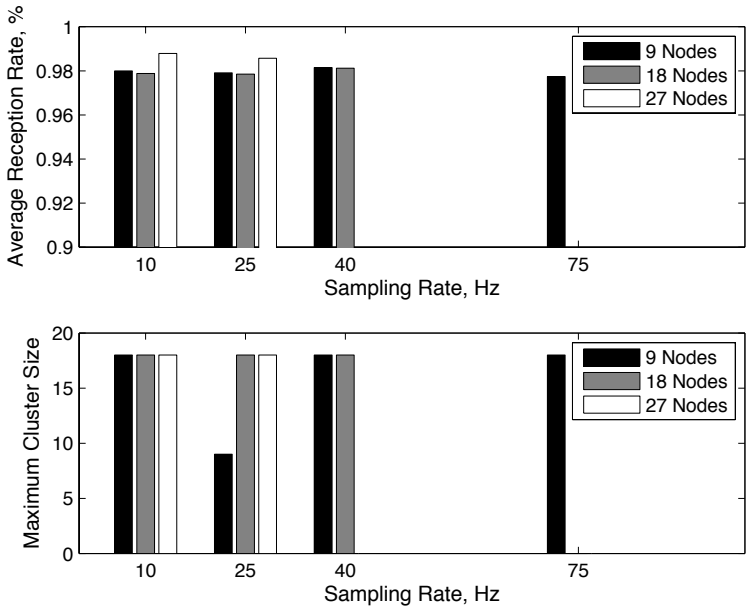

Figure 5.10: Data Delivery Performance Results for 9-Sample Approach.

In addition to average reception rate, the maximum cluster of samples dropped was calculated. The maximum cluster size gives an indication of burst loss, which is more of a concern when samples are buffered. Furthermore, a small cluster size illustrates that the application is able to recover if the timed scheme fails for a sample and that the transmission errors do not accumulate. For the 3-sample approach, typically only one packet is dropped. The maximum cluster size indicates about two packets are dropped for the 9-sample approach. The slightly poorer performance could be accounted for by the indoor testing environment, which has a higher likelihood of poor communication due to multi-path effects and other wireless networks

or devices operating locally on the 2.4 GHz band. In general, however, the maximum cluster size is small for both approaches.

Overall, these results highlight the tradeoff between the number of samples buffered, network size, maximum available sampling rate, and reliability. The 9-sample approach significantly increases the network size for a small increase in sampling interval; however, the average reception rate is lower, because a lost packet corresponds to more data loss. Thus, the real-time data acquisition application can be tailored based on the desired network performance, i.e. for minimum latency the un-buffered approach is used, for maximum network size with high sampling rates the 9-sample buffer is used, and for balanced throughput, latency, and reliability the 3-sample buffer is used.

5.4 Summary

This chapter presents the implementation of high-throughput real-time wireless data acquisition on the Imote2 platform. While this implementation is specific to the Imote2, the hardware and software challenges addressed are common to many available platforms. The resulting application framework for real-time data acquisition and its performance are presented. The application is expanded for high-throughput applications that require large network sizes and high sampling rates. Ultimately, the communication and processing protocols allow for near-real-time sensing of 108 channels across 27 nodes at up to 25 Hz with minimal data loss and require no low-level modifications to the operating system or large memory buffers.

IMPLEMENTATION OF CONTROL STRATEGIES ON WIRELESS SENSOR PLATFORM

Essential features for control implementation are consistent sampling and actuation times among nodes, accurate computation, and flexibility for a variety of systems. The tight scheduling, use of alarm interrupts, and communication protocol insights from the real-time wireless data acquisition framework described in the previous chapter are used to achieve these control implementation goals. Two control strategies are considered in this chapter: fully decentralized control and centralized control. The fully decentralized control strategy addresses both the SHM-A and SHM-SAR implementation. The control node approach developed for fully decentralized control is combined with real-time wireless data acquisition for a centralized control implementation. The performance of each control strategy implementation is evaluated to inform future control designs.

6.1 Fully Decentralized Control

A fully decentralized control framework was implemented on the Imote2 smart sensor platform that ensures consistent actuation times, accurate computation, and flexibility for future decentralized control implementations. An overall application flowchart is presented in Figure 6.1. In fully decentralized control, the sensing, computation, and commanding occur on each individual leaf node, or controller node. The gateway node conducts time synchronization on the network to ensure consistent start time and scheduling among the nodes. In experimental settings, when the decentralized control is complete, the gateway node retrieves the sensor data and computed control action for verification.

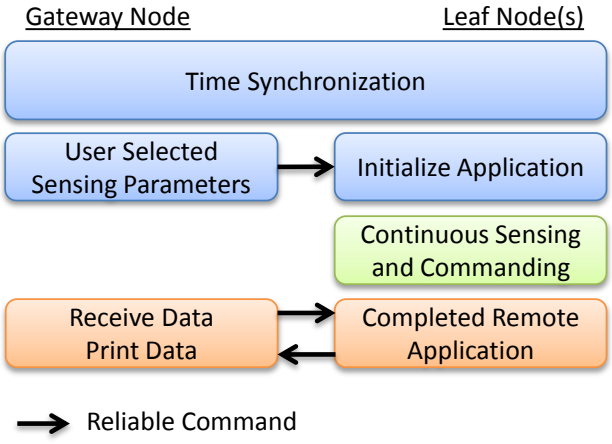

Figure 6.1: Application flowchart for Fully Decentralized Control.

6.1.1 Fully Decentralized Control with an SHM-A for Data Acquisition

Within the continuous sensing and commanding portion on the controller node, a tightly timed approach is used to maintain consistent actuation command intervals (Figure 6.2). Based on the approach used in continuous sensing, command alarms are set at a specified interval after the sensing event to maintain better scheduling of the actuation. The sensing events are a more consistent basis for setting the command alarm rather than using a timer, which can be preempted or delayed in the task queue, or setting repeated alarms based on the command interval, because delays in the alarm can accumulate. The one limitation of this approach is that the slight variation in sampling rates on different nodes can cause the actuation times to drift between individual nodes. For example, on two nodes fitted with an SHM-A, the sampling rates differ within the resolution of the clock on the Imote2 when sampling at 10 Hz; yet, a drift results in the difference of command times, which is illustrated in Figure 6.3. Some of this drift could also be attributed to error in the clock drift estimate during time synchronization, but this part of the drift should not be significant within the initial operation of the application. Although this difference in the command time will accumulate over time, the performance is at the limit of the current hardware and software; and, the error is reasonable over a standard testing timeframe. Therefore, the current timed approach maintains consistent actuation intervals over an experimental timeframe.

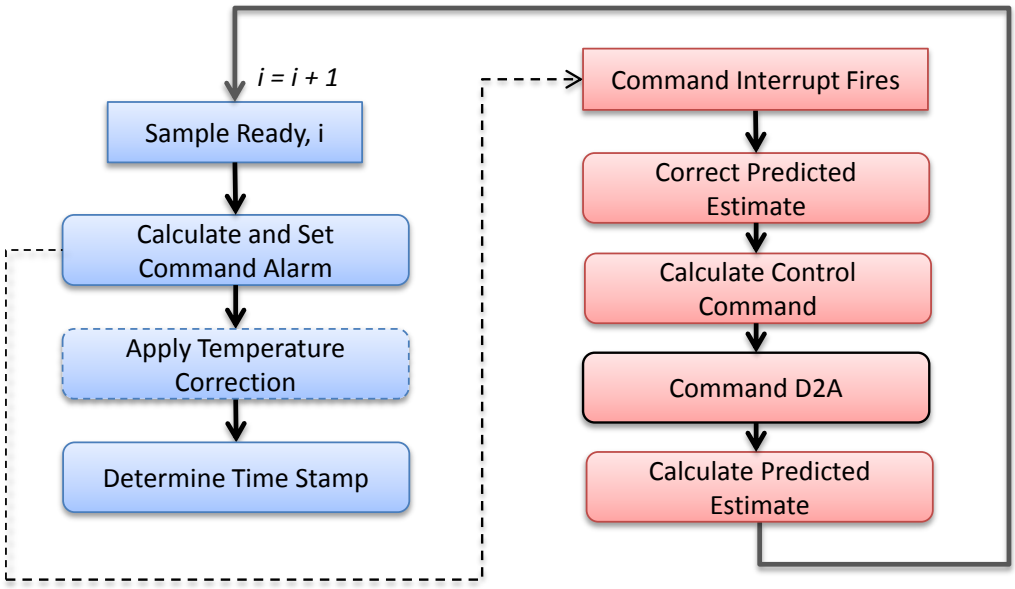

Figure 6.2: Sensing and Command Flowchart for Leaf Node within Fully Decentralized Control with an SHM-A.

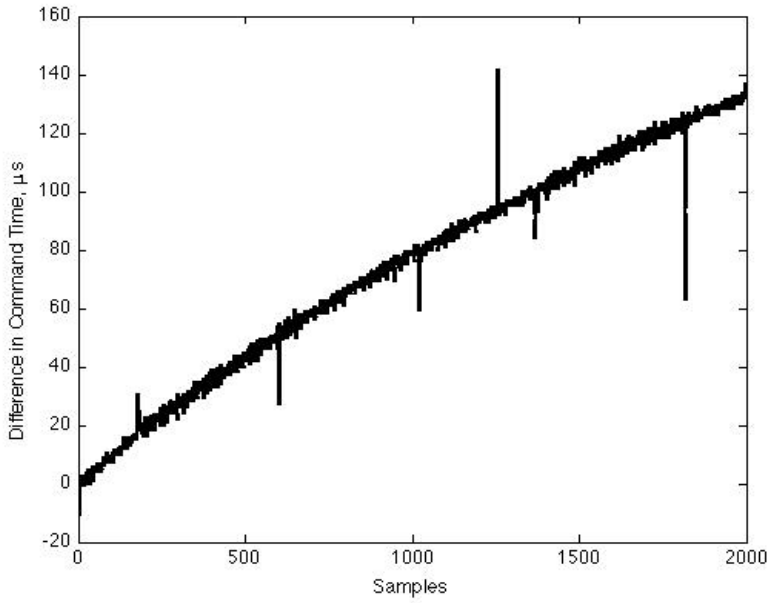

Figure 6.3: Drift in the Difference in the 100ms Command Interval among Controller Nodes.

On the controller node, the estimation and control gain calculations were broken up to limit the processing time and care was taken to ensure their accuracy. The predictor-corrector formulation of the Kalman filter allows the time update of the estimate, or prediction, to be calculated separately from the measurement update, or correction, as shown in Figure 6.2. Within the calculations, care was taken to limit cancellation error and leverage any sparsity in the system to limit the number of operations and improve accuracy. To evaluate the performance of the calculations on the controller node, a sample controller developed for a SDOF setup was implemented on the Imote2 fitted with an SHM-A. A random input was applied to the node and the resulting calculations were compared with an implementation on Matlab. The Imote2 and Matlab calculations lie directly on top of one another with a maximum error of $4x10^{-5}$. Therefore, the numerical error due to calculations on the Imote2 processor is limited.
In addition, the results of a timing analysis of the relative components conducted with the Imote2 operating at 104 MHz are given in

Table 6.1. The ‘Sensing Time’ is the time from when a sample is received through determining the timestamp. The ‘Command Time’ encompasses the time required to correct the predicted estimate, calculate the control command, and command the SHM-D2A. The ‘Estimate Time’ is the processing time required to calculate the predicted estimate. The standard deviations are small because the processing time should be consistent. Because the variation is small, the mean plus one standard deviation offers a good baseline to calculate the maximum sampling rate possible with this level of computation. If all three components are considered, the maximum sampling rate possible if only processing is considered is about 330 Hz. Therefore, if the appropriate sensing hardware is used, the additional processing power of the Imote2 and the implementation on the controller node results in significantly improved sampling rate performance for decentralized control.

Table 6.1: Timing Analysis of Controller Node Processing Components in Decentralized Control.

	Sensing Time	Command Time	Estimate Time
Mean (µs)	571.0	896.9	1411.5
Standard Deviation (µs)	101.9	21.1	14.6
Mean + Standard Deviation (µs)	672.9	918.0	1426.1

6.1.2 Fully Decentralized Control with an SHM-SAR for Data Acquisition

Because the SHM-SAR driver uses alarms for data acquisition, the sensing and control implementation on the leaf node for fully decentralized control uses a different approach than outlined in section 6.1.1. Additionally, no appreciable time delay between data acquisition and sample availability on the Imote2 is found for the SHM-SAR; so, the command time and sample ready event overlap. The sensing and control approach on the leaf node uses the sample ready event to signal the command for actuation; and, no additional alarm is required (Figure 6.4). The consistency of the command interval is dependent on the performance of the sampling interval and any variation in the time required to command the SHM-D2A. As seen in Chapter 4, the SHM-SAR driver results in a consistent sampling interval and particularly when the processor operates at 406 MHz. By limiting the computation between sampling and commanding the SHM-D2A, the variation in the time required for actuation is minimal; however, the framework builds in one sample delay between sampling and commanding.

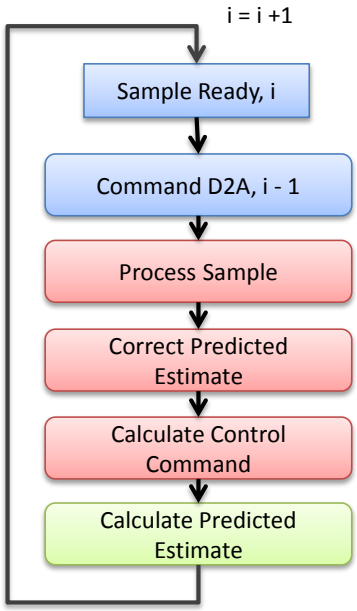

Figure 6.4: Sensing and Commanding Flowchart on Leaf Node for Fully Decentralized Control with an SHM-SAR.

Because alarms are used in this framework to maintain consistent sampling intervals and, by extension, the control intervals, a timing analysis is used to determine the maximum sampling rate and the time required for each component. Significant loads on the processor will cause large variations in the sampling interval and delays to accumulate, so the timing analysis is essential for successful control implementation. In the timing analysis presented in Table 6.2, the

'Command and Process Sample Time' corresponds to the time from the sample being passed to the application until it is processed, which includes the time required to command one channel of the SHM-D2A. The 'calculation time' includes updating the predicted estimate, calculation of the control command for the next step, *i*, and updating the predicted estimate given that command. The same calculation formulation is used as for the SHM-A, so the calculation accuracy is unchanged; however, the calculation time is shorter due to the higher processor speed. The 97th percentile value from the cumulative density function of the timing analysis is used to determine the minimum interval so that variation in the sampling interval due to load on the processor is minimal. Given the timing analysis, the maximum sampling rate is about 975 Hz. This decentralized control rate is significantly higher than for the SHM-A and previous implementations in the literature.

Table 6.2: Timing Analysis for Leaf Node Framework with SHM-SAR.

	Command and Process Sample Time (μs)	Calculation Time (μs)	Minimum Interval (μs)
Mean	406.8	526.3	933.1
Mean + Standard Deviation	463.0	531.2	991.2
97th Percentile	498	533	1024

Any drift in the command times among nodes for the SHM-SAR framework is mainly due to the SHM-SAR driver. Because the timing analysis limits error due to load on the processor, the largest source of error in the command time is the alarm interrupts for sensing used by the driver. At a 406 MHz processor speed, the variation in the sampling interval among nodes is small. Some additional drift over time will occur due to time synchronization among the nodes, but this drift should not be significant in the initial application operation. Figure 6.5 shows the difference in the command time for two leaf nodes fitted with the SHM-SAR running fully decentralized control at 25 Hz. The jumps every 100 samples are due to the time stamping process, which interpolates between time stamps captured every 100 samples. Therefore, the difference in the command time is truly the value it is converging to over time, which is approximately 15 μs. In addition, unlike for the SHM-A framework, the difference in command time does not grow with time but is bounded. This difference in command times among nodes is non-deterministic but is a small percentage of the interval. Therefore, the difference in the control time due to the implementation on the Imote2 is very small and will not impact the controller performance.

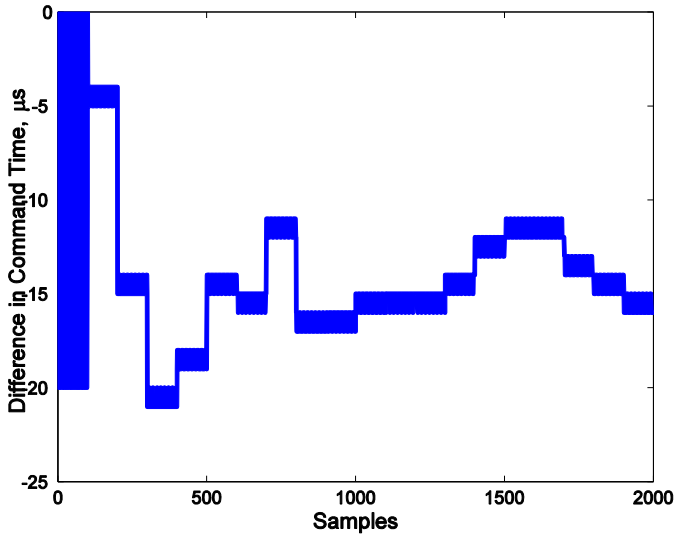

Figure 6.5: Drift in Command Interval for Fully Decentralized Control Framework with SHM-SAR.

6.2 Centralized Control Implementation

Centralized control combines wireless data acquisition and control calculations on the received data. Because the SHM-SAR offers low latency and excellent decentralized control implementation performance, the SHM-SAR data acquisition board will be used exclusively for centralized control. Therefore, the centralized control implementation outlined in this section combines the controller node insights from section 6.1.2 and the real-time wired data acquisition presented in Chapter 5.

The overall centralized control framework uses three different node classifications: gateway node, controller node, and leaf nodes (Figure 6.6). The gateway node is responsible for initializing the application, conducting time synchronization, and issuing the time-division multiple-access communication protocol (TDMA) delay message based on the responsive nodes. In experimental settings, the gateway also retrieves data from the controller node to evaluate the performance. The controller node processes the remote data, completes the control calculations, and commands the SHM-D2A. The leaf nodes continuously sense and send the data to the control node similar to the leaf nodes in Section 5.2. The commands to initialize the application and set the TDMA delay are sent reliably to ensure the control application is initialized properly (Figure 6.7). On the other hand, the data from the leaf nodes is sent unreliably to the controller node. As a result, data loss is possible in the centralized control implementation.

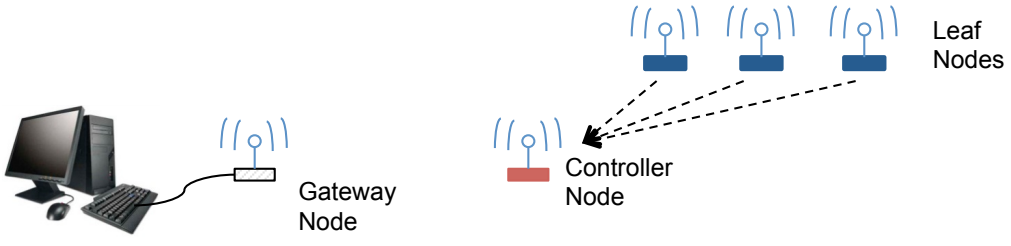

Figure 6.6: Centralized Control Node Framework.

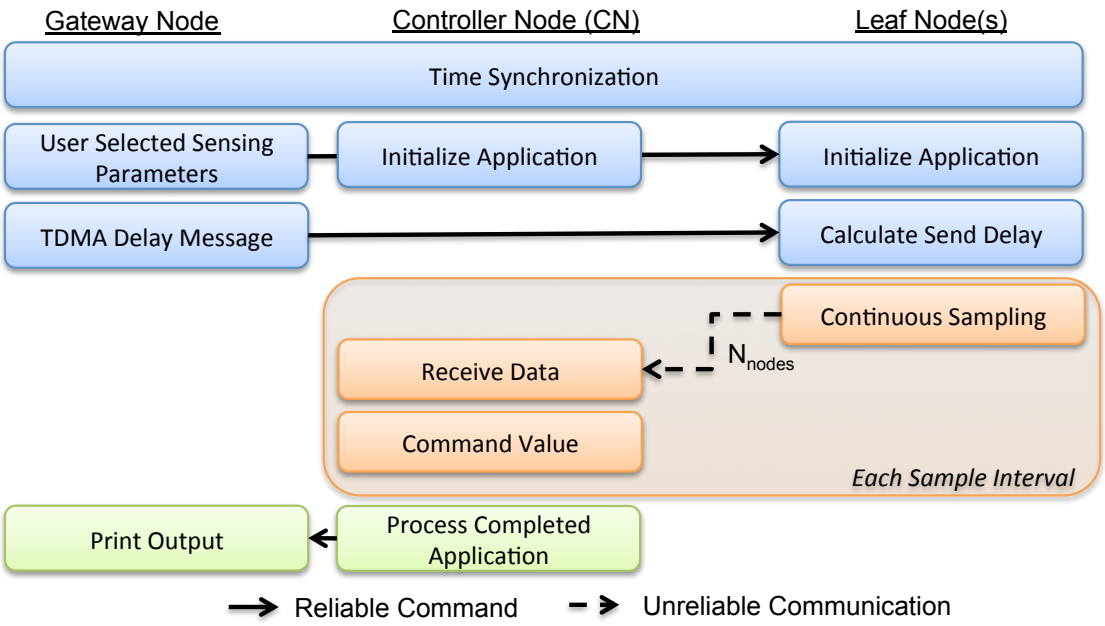

Figure 6.7: Application Framework for Centralized Control.

To limit the load on the processor due to receiving data, completing calculations, and issuing the command, the sampling and control are divided onto two different node types. If all those elements were on one node, the processing load can be prohibitive and cause the sampling and control to drift significantly; thus, making the application performance much less stable. Similar to the driver for the SHM-SAR, the control node uses an alarm to time the commands. Therefore, the command alarm on the controller node overlaps with sensing alarm on the leaf nodes. As illustrated in Figure 6.8, when the alarm interrupt fires, the command is issued to the SHM-D2A and then the alarm is reset using equation (4.2). The predicted estimate is updated based on the command applied. If all the leaf node samples are received, the estimate is corrected and the next command is calculated. Similar to fully decentralized control, the framework includes a one-sample control delay.

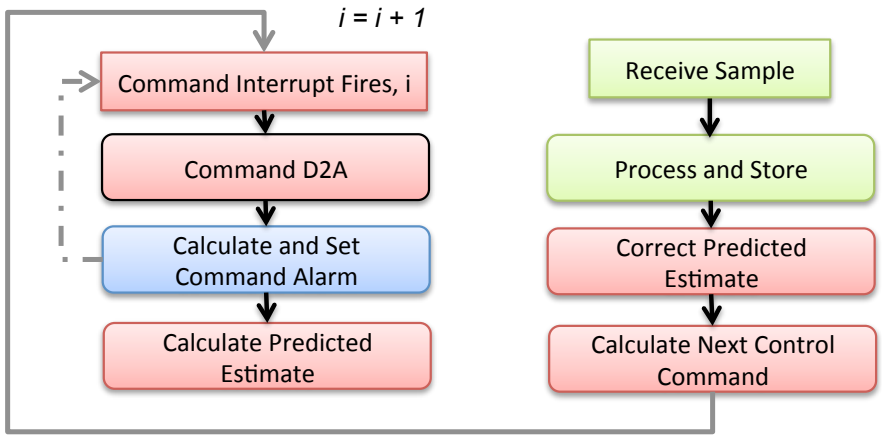

Figure 6.8: Remote Sample Processing and Calculation Flowchart for Control Node in Centralized Control.

The timing analysis is essential for determining the maximum sampling interval possible while maintaining an accurate control interval on the control node. One key to the control node

framework is that the time-update of the estimate must be completed before samples are received from the leaf nodes. This approach allows the estimator to be time-updated if enough remote samples are not received to update the predicted estimate. Table 6.3 presents the timing analysis for a system with four leaf nodes and twelve states in the control model. Although the time required for sending per node will be consistent, the calculation time will vary with number of states in the model. Thus, for four remote nodes with a timeslot length of 7.8 ms, the maximum sampling rate is around 31 Hz. This sampling rate is similar to a network for wireless real-time data acquisition.

Table 6.3: Timing Analysis for Control Node in Centralized Control.

	Command and Estimate Time	Send Time (per node)	Control Calculation Time
Mean (µs)	295.4	7095.0	1034.2
Mean + Standard Deviation (µs)	303.9	7463.1	1044.5
97th Percentile (µs)	311	7707.5	1059

6.3 Summary

The frameworks developed for two different control architectures achieve consistent command intervals among nodes, accurate onboard computation, and notable sampling rates. The fully decentralized and centralized control application frameworks build on insights gained in Chapter 5, particularly the use of tight scheduling, alarm interrupts, and TDMA communication protocols. The fully decentralized control leaf node framework for use with the SHM-SAR highlights the advantage of this low-latency data-acquisition board over the SHM-A. The maximum possible decentralized sampling rate is significantly higher than previously identified in the literature. The centralized control framework maintains the sampling rate performance of real-time wireless data acquisition while including control calculations. Finally, these frameworks can easily be adapted to other levels of decentralization.

SINGLE-STORY BUILDING CONTROLLED WITH SMART SENSORS

This chapter evaluates the low-latency hardware and wireless control framework through control of a single-degree-of-freedom (SDOF) structure fitted with an active mass driver (AMD). The successful implementation of active control using the Imote2 smart sensor platform is compared to a wired system for performance evaluation. This chapter presents the system model, discrete control design techniques, wired continuous control design for comparison, smart sensor control design, and experimental results.

7.1 System Model

The setup used for the active control experiment, performed in the Smart Structures Technology Laboratory is shown in Figure 7.1. The structure, manufactured by Quanser Consulting Inc., is a single-story building clamped to a fixed base. The aluminum columns have a section of 2 x 108 mm and an interstory height of 490 mm. The mass of the story is 1.662 kg and the mass of each column is 0.227 kg. The structure is fitted with an AMD to control the structure. The mass of the AMD is 0.88 kg; although the mass of the AMD is a large percentage of the total structure, the goal of the experiment is to compare the performance of the two control systems. The AMD is fitted with a DC motor to move the cart along a geared track. An optical encoder is used to feedback the position of the cart along the 19 cm track. The position control of the cart is realized using a proportional derivative (PD) controller with the encoder feedback. The control is implemented using a WinCon real-time controller on a PC fitted with a MultiQ I/O board. Finally, a capacitive DC accelerometer with a range of ±2g and a sensitivity of 1V/g was placed on the top story.

A system identification was conducted to develop a model of the experimental setup. A band-limited white noise command displacement was input to the cart to excite the structure and the resulting AMD displacement and the acceleration of the top story was measured using a VibPilot data acquisition system. The resulting transfer functions were calculated and input into a frequency domain identification tool called MFDID (Kim et al. 2005), which will be described in more detail in Chapter 8. An analytical model of the system was developed alongside the experiment to develop intuition for the model identification. The resulting analytical model shown in Figure 7.2; the experimental data is shown in blue and the identified model is shown in red. The identified model closely matches the experimental data in the frequency domain.

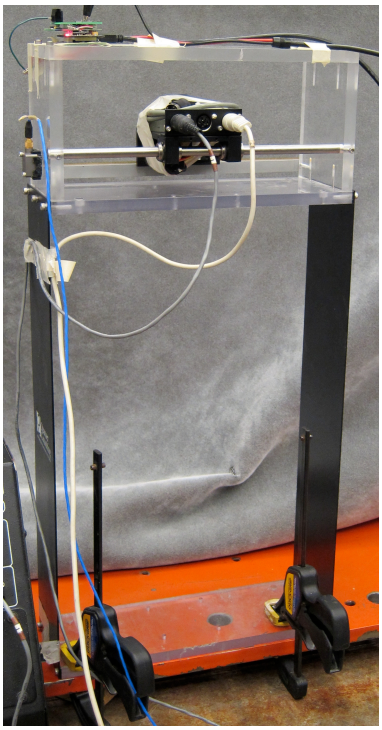

Figure 7.1: Single-story experimental setup.

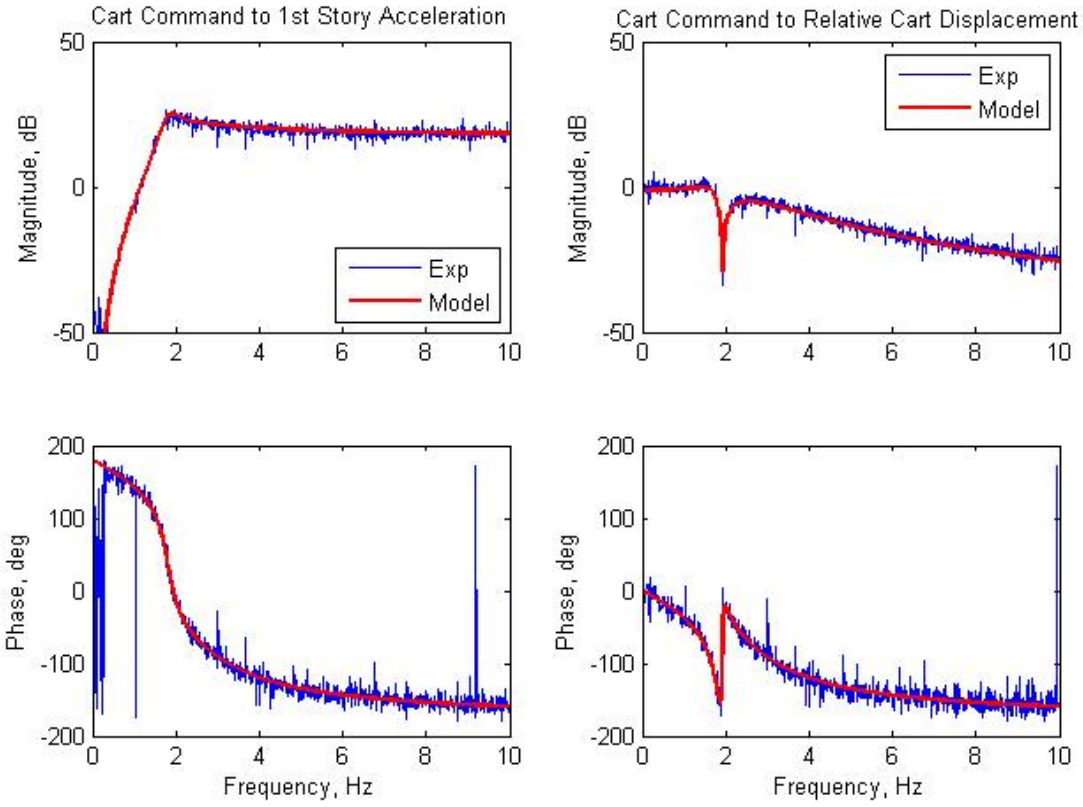

Figure 7.2: Experimental Transfer Function and Identified Model of Small-Scale Setup.

The identified model neglects the high-frequency dynamics of the motor, which results in a four- pole model. The high frequency dynamics of the motor would require a pole far into the left-half plane that is significantly faster than the system of interest; therefore, the pole can be neglected. The acceleration response (g) due to the cart command (V) has four zeros at the origin and the cart displacement response has three zeros. The identified natural frequencies and damping are listed in Table 7.1. The first frequency corresponds to the structure and the second corresponds to the AMD. The identified damping in the first mode likely overestimates the damping in the structure, because experimentally the structure appears lightly damped.

In addition, the experimentally identified transfer functions illustrate the phenomenon of control-structure interaction (CSI) in which the dynamics of the structure directly impact the dynamics of the AMD controller. The phenomenon, first described by Dyke et al. (1995), is explained analytically for the AMD system by Battaini et al. (2000). The pole of the structure corresponds to the zero observed in the transfer function from the cart command to the cart displacement. Thus, at the natural frequency of the structure, where the response is the greatest, the AMD has the least ability to control the response. This system identification approach successfully captured CSI; inclusion of CSI is essential for control design.

Table 7.1: Identified Natural Frequencies and Damping of Experimental Setup.

Natural Frequency (Hz)	Damping (%)
1.81	11.9
2.59	58.3

Given the identified poles and zeros of the system, the state-space representation of the structure used for control design is as follows:

$$\mathbf{A} = \begin{bmatrix} -1.36 & 16.00 & 0 & 0 \\ -8.05 & -1.36 & 32.00 & 0 \\ 0 & 0 & -9.49 & 64.00 \\ 0 & 0 & -2.74 & -9.49 \end{bmatrix} \quad \mathbf{B} = \begin{bmatrix} 0 \\ 0 \\ 0 \\ 16 \end{bmatrix}$$

$$\mathbf{C} = \begin{bmatrix} -0.23 & -0.17 & 1.41 & 10.73 \\ 0.01 & -0.02 & 0.20 & 0 \end{bmatrix} \quad \mathbf{D} = \begin{bmatrix} -7.91 \\ 0 \end{bmatrix} \tag{7.1}$$

7.2 Discrete Control Design at Slow Sampling Rates

An experimental control implementation typically requires a discrete-time representation of the controller. Because the wireless control system can often run at a slow sampling rate, a discrete-time controller is necessary. For the wireless system, a slow sampling rate results from the time required for sensing, processing, and communication. Beyond ensuring the bandwidth of the system to be controlled is below the Nyquist frequency, the two important considerations for the performance of the discrete control design include: a discrete-time representation of the system and the inclusion of delays within the system model.

7.2.1 Discrete-Time Representation of the System to be Controlled

Three common transformation techniques are used to develop discrete-time equivalents based on numerical integration (Franklin 1998); these techniques are illustrated in Figure 7.3. The forward rectangular rule, or zero-order hold (ZOH), can create an unstable system because the resulting discrete-time poles do not necessarily lie within the unit circle. The backward rectangular rule forces the poles within the right-half plane of the unit circle. The trapezoid rule, commonly known as the Tustin method, always results in a stable system because the resulting poles must lie within the unit circle; however, this transformation can result in significant distortion. Another approach is an algorithm that tries to match the zero-pole equivalent in a discrete system and match the gain at the origin. All these approaches have advantages and disadvantages, but the two most common transformation approaches that will be addressed in this section is the ZOH and Tustin transformation.

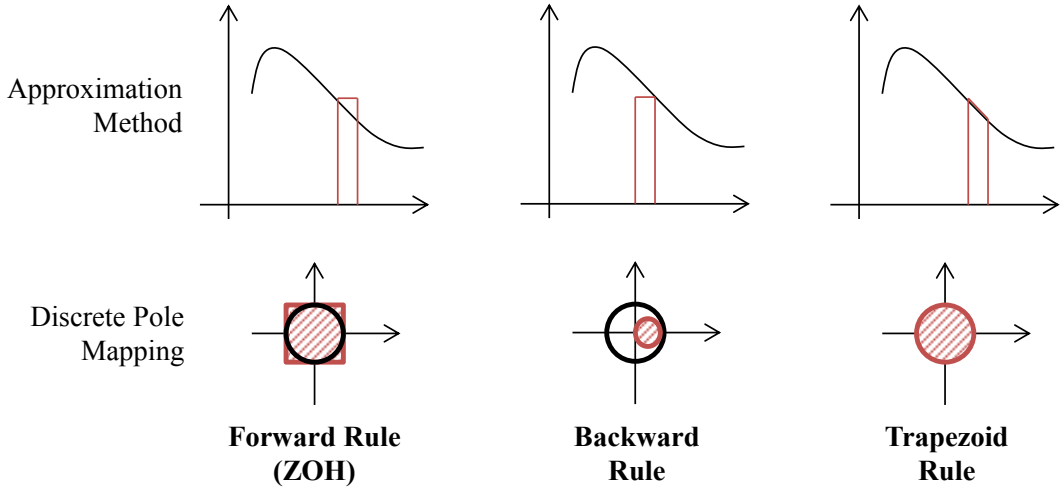

Figure 7.3: Discrete Equivalent Transformation Techniques.

One approach to control design is to transform a compensator designed in continuous time into discrete time. As described in Chapter 2, this approach is common in wired control systems, because a fast sampling rate can be employed. Within wired control systems, the most common approach for transformation of the compensator designed in continuous into discrete time is the Tustin method, because it guarantees a stable system and can closely represent the controlled continuous-time system. However, when applied to systems with a slow sampling rate, transformed continuous-time controllers often result in instability and poorer performance. When using a ZOH transformation of the continuous controller, often an unstable control system results. Similarly, when a Tustin transform of the compensator is used, the discrete closed-loop system at the slow sampling rate is near the stability boundary. Therefore, a less authoritative compensator is required for stability in discrete-time. The instability and poorer performance using this control transform approach is likely due to the slow sampling rate and un-modeled internal delay present in a discretely sampled system.

For systems operating at a slow sampling rate, designing a controller directly on the discrete-equivalent of the system leads to a more consistently stable system and better control performance. A sample single-degree-of-freedom system fitted with an AMD is used to compare the discrete time transformation of a system prior to control design. As shown in Figure 7.4, the Tustin transformation gives much better results at approximating the continuous-time system

whereas the ZOH transformation gives poor results at the origin in both the magnitude and phase. However, a ZOH transformation results in a better control design because it approximates the sampled data system present in control.

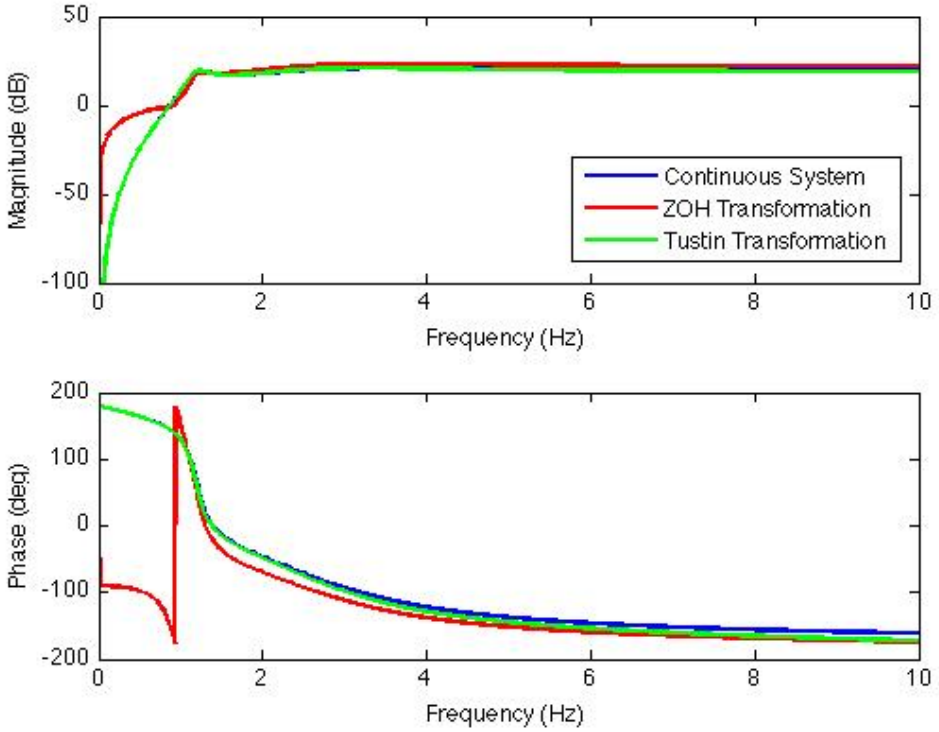

Figure 7.4: Comparison of Discrete Time Transformation Techniques in the Frequency Domain.

A sample and hold system used in the control system can be directly modeled in discrete-time with a hold equivalent transform, as shown in Figure 7.5. A sample and ZOH is an exact model for the sample and hold common in the A/D converter used in discrete control. Thus, a ZOH transform reflects the actual sampled system that will be encountered by the controller. In addition, a ZOH sampled system introduces a delay of *T/2*, where *T* is the sampling interval. This internal delay is integrated into the model during the transform; and thus, the delay can be compensated for in the controller design. As a result, although the ZOH representation looks poorer in the frequency domain, a ZOH equivalent transform to a discrete-time model prior to control offers the best performance for a slowly sampled system.

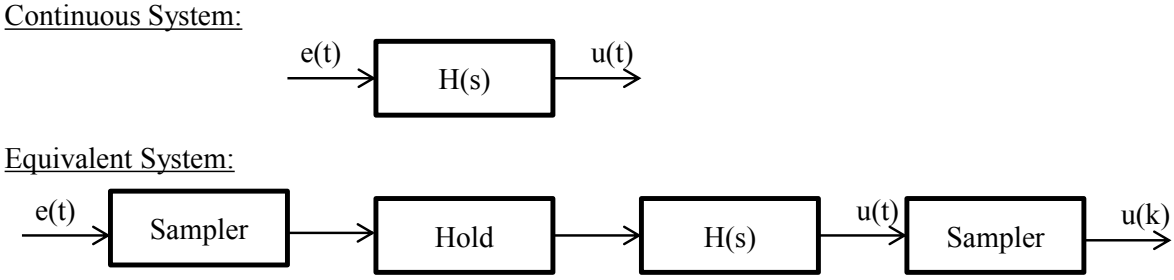

Figure 7.5: Equivalent Sample and Hold System in Discrete-Time Control.

7.2.2 Inclusion of Delays with the System Model

The time required for the sensing hardware, processing, and wireless communication results in at least a one-sample delay in the control system, which can be included as a sensor or input delay. The two different delay approaches are shown in Figure 7.6, where the controller is represented by an estimator and control gain, K. When a sensor delay is considered in the system, the system responds to a command input in exactly the same way as without the delay because the estimator sees the input command through the feedforward loop. However, the estimator is sensitive to disturbances through the delayed output (Franklin 1998). In addition, the delayed states are not weighted within the control gain, but are weighted within the estimator design. On the other hand, when an input delay is present in the system, the delays will be excited in the system response to an input command; and thus, the delayed system is used within the control design. However, the delayed states are not weighted within the estimator. In addition, the control feedback will be delayed before it can react to a disturbance to the plant, so the system is more sensitive to disturbances (Franklin 1998). As a result, the representation of the delay can impact the resulting control design and performance of the system.

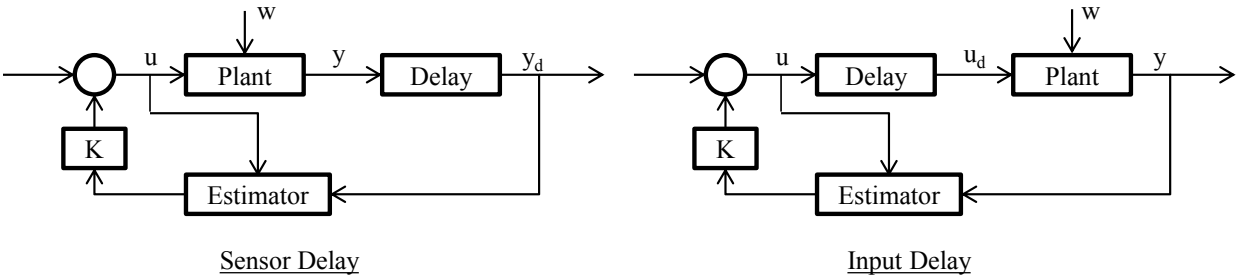

Figure 7.6: Delay Representations (Franklin 1998).

In simulation, the two representations can result in comparable control performance if the delay is compensated for in the control design; however, the representation should adequately represent the delay present in the experimental system. Although the delay present in the wireless system seems to be a sensor delay, an input delay better reflects the experimental configuration because the controller computation occurs on the sensor prior to the application of control to the system. In addition, the estimator design based on an input delay requires slightly less computation because the delayed state is not weighted, which can be advantageous on a smart sensor platform. As a result, based on the experimental configuration, an input delay model should be used to include the delay present in wireless control systems.

Several approaches to modeling the input delay within the system model are available, as described in Chapter 2; however, not all approaches allow dynamic output feedback. Two common approaches that do allow dynamic output feedback include the Padé approximation in continuous systems and state augmentation in discrete systems (Sain et al. 1992; Franklin 1998). Because a continuous-time model is required for Padé delay states, an equivalent one step delay could be included in the continuous time system. The order of the Padé approximation is limited by the bandwidth of the system when converted to discrete-time. In the previous analytical SDOF example, including the delay with a Padé approximation prior to discrete-time transformation resulted in a system close to the stability boundary and poorer performance in the presence of a time delay. Therefore, an input delay should be added to the discrete-time ZOH transformation of the system, described in the previous section, by including a delay state in the state-space representation:

$$\begin{bmatrix} x[k+1] \\ u_d[k+1] \end{bmatrix} = \begin{bmatrix} \Phi & \Gamma \\ 0 & 0 \end{bmatrix} \begin{bmatrix} x[k] \\ u_d[k] \end{bmatrix} + \begin{bmatrix} 0 \\ 1 \end{bmatrix} u(k) + \begin{bmatrix} \Gamma \\ 0 \end{bmatrix} w(k)$$
$$y(k) = \begin{bmatrix} 1 & 0 \end{bmatrix} \begin{bmatrix} x[k] \\ u_d[k] \end{bmatrix} \tag{7.2}$$

where u_d is the delayed input. Although the **A** matrix is no longer full rank, the augmented system does satisfy the conditions for a solution to the linear quadratic regulator (LQR) control problem. This discrete-time state augmentation approach was the best solution for implementing an input delay within the system model and resulted in good compensation performance.

7.3 Control Design

7.3.1 Wired Continuous Control Design

A wired control system is developed for comparison with the smart sensor implementation. Because the wired system operates at 1000 Hz, the wired system can be approximated as continuous. Therefore, this section presents the continuous control design that is implemented on the wired system.

Acceleration feedback has been shown to be effective in active structural control, as described in Chapter 2. Because acceleration measurements can be reliable and inexpensive, the system will use the top story acceleration response as the primary measurement for control of the structure. Therefore, the control design will combine an estimator and linear quadratic regulator control design as outlined in Chapter 3. Furthermore, because the capacitive accelerometer provides a flat frequency response over the range of interest and zero phase lag, the sensor dynamics will be neglected in the design.

The LQR control design uses acceleration weighting to minimize the acceleration. To implement the acceleration weighting, the cost function presented in equation (3.10) is altered to:

$$J = \int_0^\infty [yQy + uRu]\,dt \tag{7.3}$$

where y is the acceleration output, Q is the relative weighting on the measurement, u is the control effort, and R is the weighting on the control effort. For the control design in this case, the ratio of Q/R is varied and the root-mean-square (RMS) of the acceleration response and the control effort are determined based on numerical simulation. In simulation, the cart is used to excite the structure prior to switching from excitation to control. Two initial conditions are considered based on when the cart is switched from excitation to control: the cart is at maximum velocity or maximum displacement. The RMS of the acceleration normalized by the uncontrolled response is plotted versus the RMS of the control effort for the two initial conditions in Figure 7.7. As the control force weighting, R, decreases, the additional control effort actually causes a worse response than the uncontrolled. The control design that resulted in a minimum response to the initial displacement was selected because it is the larger response of the two initial conditions; the selected controller design is highlighted with a red 'x' in Figure 7.7. The associated Q and R values are

$$Q = [1] \quad R = [0.9955]$$

and the resulting control gain matrix is

$$\mathbf{K} = \begin{bmatrix} 0.0048 & -0.0344 & -0.2182 & -0.1068 \end{bmatrix}.$$

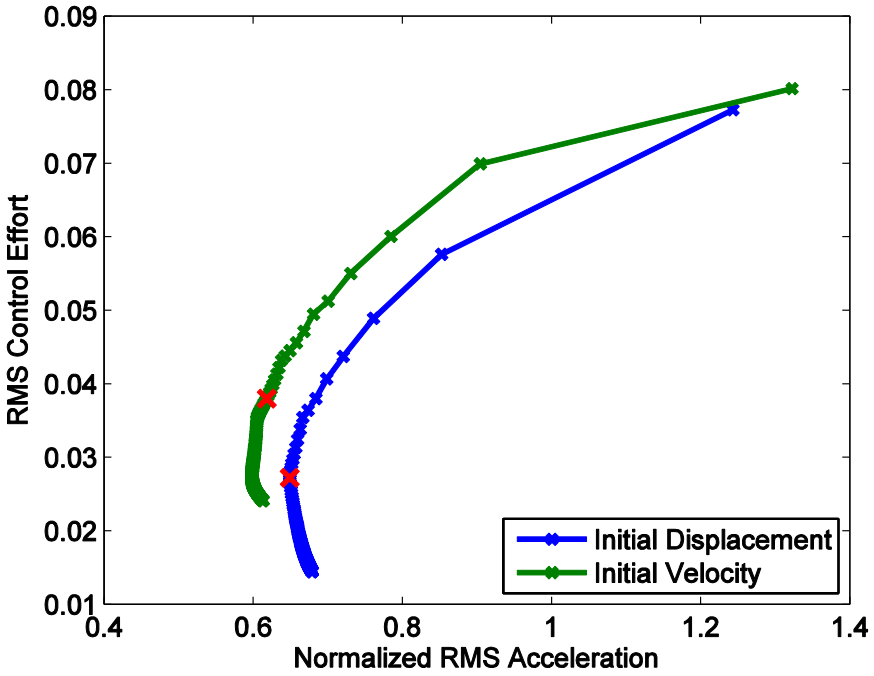

Figure 7.7: Summary of Continuous LQR Control Designs with Selected Design Highlighted.

An estimator is required to reconstruct the full-state response of the system based on the acceleration measurement. Because the process noise is hard to estimate within the system, the final estimator design is determined experimentally. A range of estimator designs is determined analytically and then applied experimentally with the same LQR control design. The estimator that results in the best performance of the complete control system is selected:

$$S_w = \begin{bmatrix} 1 \end{bmatrix} \quad S_v = \begin{bmatrix} 10 \end{bmatrix}$$

and the resulting estimator gain is

$$\mathbf{L} = \begin{bmatrix} -7.1861 & 5.8207 & 3.1096 & -0.2130 \end{bmatrix}.$$

7.3.2 Discrete Control Design for Smart Sensor Implementation with the SHM-A

A discrete control design was developed for the Imote2 wireless smart sensor fitted with an SHM-A. Given the decimation scheme presented in section 4.1, the latency associated with use of this sensor board is about 30 milliseconds. After combining the sensor latency with processing latency, a sampling interval of 40 milliseconds was selected, or a sampling rate of 25 Hz. Due to this slow sampling rate, a discrete control design is necessary. Following the design guidelines presented in section 7.2, a zero-order-hold discrete transformation of the system was determined that included an input delay through state augmentation. The resulting state-space system is

$$\mathbf{A}_d = \begin{bmatrix} 0.8510 & 0.5854 & 0.3355 & 0.2753 & 0.0464 \\ -0.2946 & 0.8510 & 0.9533 & 1.2020 & 0.2793 \\ 0 & 0 & 0.5904 & 1.6705 & 0.6245 \\ 0 & 0 & -0.0714 & 0.5904 & 0.5103 \\ 0 & 0 & 0 & 0 & 0 \end{bmatrix} \quad \mathbf{B}_d = \begin{bmatrix} 0 \\ 0 \\ 0 \\ 0 \\ 1 \end{bmatrix}$$

$$\mathbf{C}_d = \begin{bmatrix} -0.2288 & -0.1760 & 1.4085 & 10.7332 & -7.9088 \\ 0.0076 & -0.0162 & 0.2002 & 0 & 0 \end{bmatrix} \quad \mathbf{D}_d = \begin{bmatrix} 0 \\ 0 \end{bmatrix}$$

Similar to the continuous control design, accelerometer weighting was used for the optimal discrete LQR control design. In numerical simulation, the AMD was again used to excite the structure prior to switching to control; two initial condition cases were considered: the cart is at maximum velocity or maximum displacement prior to switching to control. The RMS acceleration normalized to the RMS uncontrolled response and RMS control effort was tabulated for a range of Q/R ratios and the two initial conditions. The normalized RMS acceleration response is plotted against the RMS control effort in Figure 7.8. As the control effort increases, the response initially decreases and then ultimately the additional control effort negatively impacts the response. The control design selected minimizes the normalized RMS acceleration for the maximum cart displacement initial condition and is highlighted in Figure 7.8 with a red 'x'. The control design response weighting, Q, and control effort weighting, R, are:

$$Q = [1] \quad R = [2.6727]$$

which results in a control gain

$$\mathbf{K}_d = \begin{bmatrix} 0.0160 & -0.0092 & -0.0904 & -0.6142 & -0.3655 \end{bmatrix}$$

Therefore, the discrete control design results in a significantly different weighting design and subsequent control gain than the continuous system.

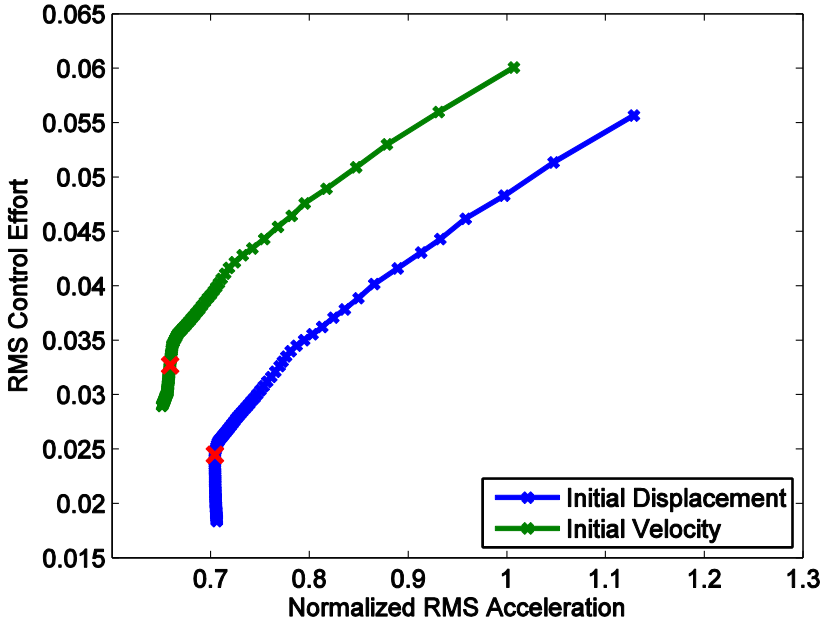

Figure 7.8: Summary of Discrete LQR Control Designs with Selected Design Highlighted.

The accelerometer on the SHM-A was used for control feedback, due to its ease of implementation and the previous success with acceleration feedback in active structural control. Because the feedback measurements only include the acceleration, the full-state must be reconstructed using an estimator. A predictor-corrector formulation of the discrete-time Kalman filter was used for estimation, as described in Chapter 3. Similar to the continuous design, a range of estimators determined analytically were experimentally implemented to determine the best estimator given the process and sensor noise in the system. The estimator that resulted in the best overall control performance was selected. The resulting process and sensor noise weightings are:

$$S_w = [1] \quad S_v = [100]$$

which results in the estimator gain matrix

$$\mathbf{L}_d = \begin{bmatrix} -0.1109 & 0.1442 & 0.0334 & -0.0092 & 0 \end{bmatrix}.$$

The larger noise weighting is due to the higher noise floor of the accelerometer on the SHM-A in addition to the noise added through aliasing during decimation. As expected, the resulting discrete-time design differs from the continuous control design.

7.3.3 Discrete Control Design for Smart Sensor Implementation with SHM-SAR

In addition, a discrete control design was developed for the Imote2 wireless smart sensor fitted with an SHM-SAR data acquisition board. Given the latency results presented in section 4.3 and the fully decentralized control framework presented in section 6.1, a sampling rate of 950 Hz was selected. Although this sampling rate is comparable to the wired system, a discrete control design approach was used because it will be implemented on the smart sensor platform. In addition, an input delay was included in the design to account for the one sample delay in the

control application. Following the design guidelines presented in section 7.2, a zero-order-hold discrete transformation of the system that included an input delay through state augmentation was used for design. The resulting state-space system is

$$\mathbf{A}_d = \begin{bmatrix} 0.9985 & 0.0168 & 0.00028 & 6.3334e-6 & 2.6698e-8 \\ -0.0085 & 0.9985 & 0.0335 & 0.001127 & 6.3357e-6 \\ 0 & 0 & 0.9899 & 0.06669 & 0.0005635 \\ 0 & 0 & -0.0029 & 0.9899 & 0.01676 \\ 0 & 0 & 0 & 0 & 0 \end{bmatrix} \quad \mathbf{B}_d = \begin{bmatrix} 0 \\ 0 \\ 0 \\ 0 \\ 1 \end{bmatrix}$$

$$\mathbf{C}_d = \begin{bmatrix} -0.2288 & -0.1670 & 1.4085 & 10.7332 & -7.9088 \\ 0.0076 & -0.0162 & 0.2002 & 0 & 0 \end{bmatrix} \quad \mathbf{D}_d = \begin{bmatrix} 0 \\ 0 \end{bmatrix}$$

Similar to the previous discrete control design, accelerometer weighting was used for the optimal discrete LQR control design. In simulation, the AMD was again used to excite the structure prior to switching to control; two initial condition cases were considered: the cart is at maximum velocity or maximum displacement prior to switching to control. The RMS acceleration normalized to the RMS uncontrolled response and RMS control effort was tabulated for a range of Q/R ratios and the two initial conditions. The normalized RMS acceleration response is plotted against the RMS control effort in Figure 7.9. As the control effort increases, the response initially decreases, and then ultimately the additional control effort negatively impacts the response. The control design selected minimizes the normalized RMS acceleration for the maximum cart displacement initial condition and is highlighted in Figure 7.9 with a red 'x'. The control design response weighting, Q, and control effort weighting, R, are:

$$Q = [1] \quad R = [1.1697]$$

which results in a control gain

$$\mathbf{K}_d = \begin{bmatrix} 0.00462 & -0.0337 & -0.2132 & -0.1178 & -0.00187 \end{bmatrix}$$

As the sampling rate increases, the control design will approximate the continuous control design with an input delay.

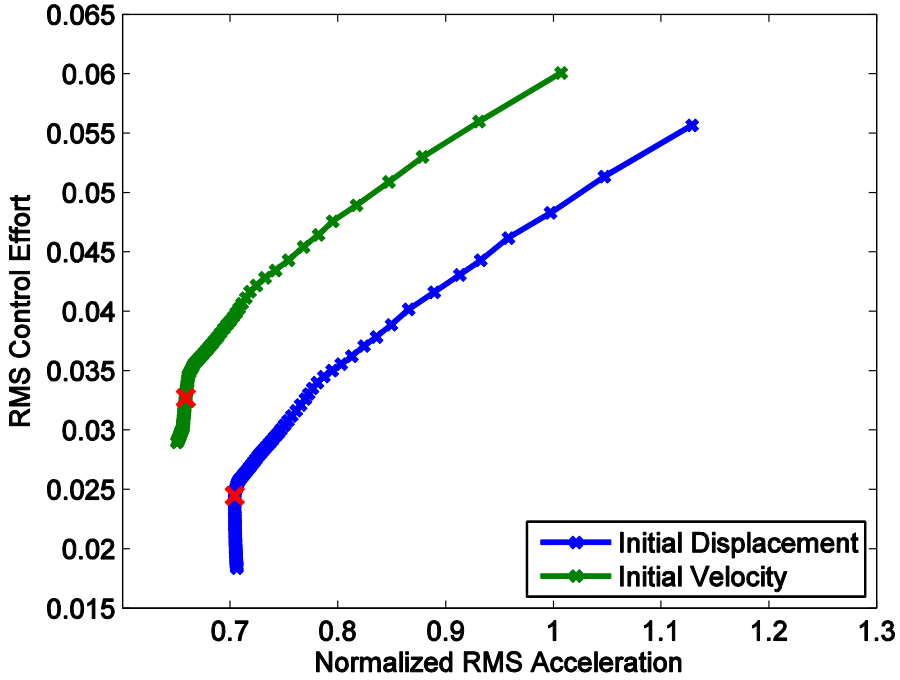

Figure 7.9: Summary of Discrete LQR Control Designs with Selected Design Highlighted.

A wired accelerometer was used for control feedback, due to its ease of implementation, previous success, and for comparison with the other control systems. Because the feedback measurements only include the acceleration, the full-state must be reconstructed using an estimator. A predictor-corrector formulation of the Kalman filter was used for estimation, as described in Chapter 3. Similar to the continuous design, a range of estimators determined analytically were experimentally implemented to determine the best estimator given the process and sensor noise in the system. The estimator that resulted in the best overall control performance was selected. The resulting process and sensor noise weightings are:

$$S_w = [1] \quad S_v = [10]$$

which results in the estimator gain matrix

$$\mathbf{L}_d = \begin{bmatrix} -0.00729 & 0.00626 & 0.00322 & -0.000242 & 0 \end{bmatrix}$$

The noise weighting is the same as the wired design, because the same accelerometer is used and little additional noise is added due to the SAR-based data acquisition. However, the resulting estimator gain matrix is different due to the discrete-time time design, as expected.

7.4 Experimental Results

The previous control designs have been implemented on the single-story experimental structure to validate the use of the smart sensor platform for active structural control. Five different configurations were considered for the validation: uncontrolled, zeroed control, wired control, smart sensor control with the SHM-A, and smart sensor control with the SHM-SAR. For the uncontrolled configuration, the AMD was fixed to the side of the structure; therefore, the

additional mass due to the cart was still present but otherwise did not influence the response. In zeroed control, a zero displacement command was issued to the AMD. Schematics of the wired and smart sensor control experimental setups are provided in Figure 7.10, Figure 7.11, and Figure 7.12, respectively. In the schematics, the solid red lines represent analog signals and the dashed red line represents the digital encoder signal. The blue lines represent the computer control calculations and the green lines represent the wireless smart sensor node.

In the wired system (Figure 7.10), the acceleration feedback is passed to the control computer through the MultiQ A/D. The continuous control design programmed onto the computer calculates the required cart displacement command. The displacement command is converted to an appropriate voltage through the PD cart control, which uses the encoder feedback. The voltage is then applied to the AMD through the amplifier and power source.

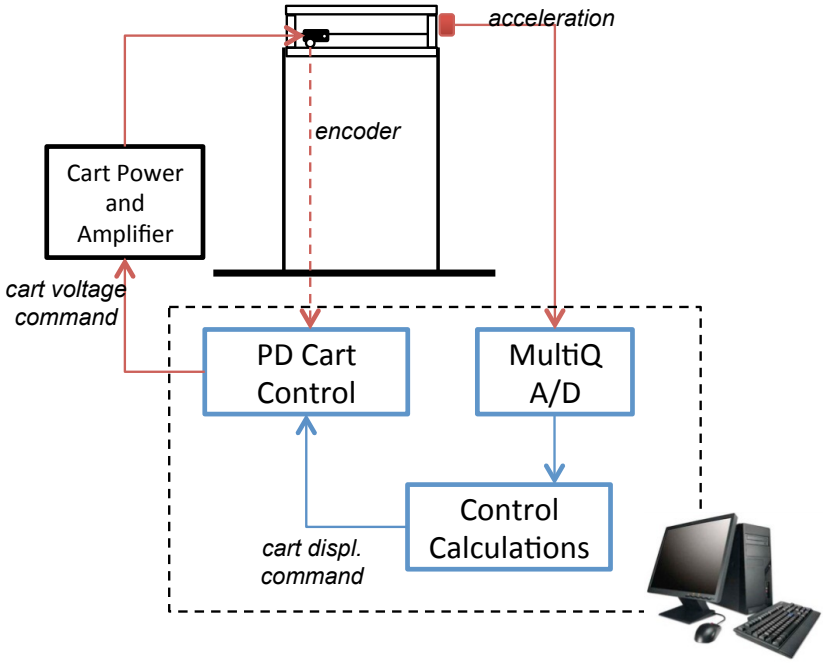

Figure 7.10: Schematic of Wired Control Experimental Setup.

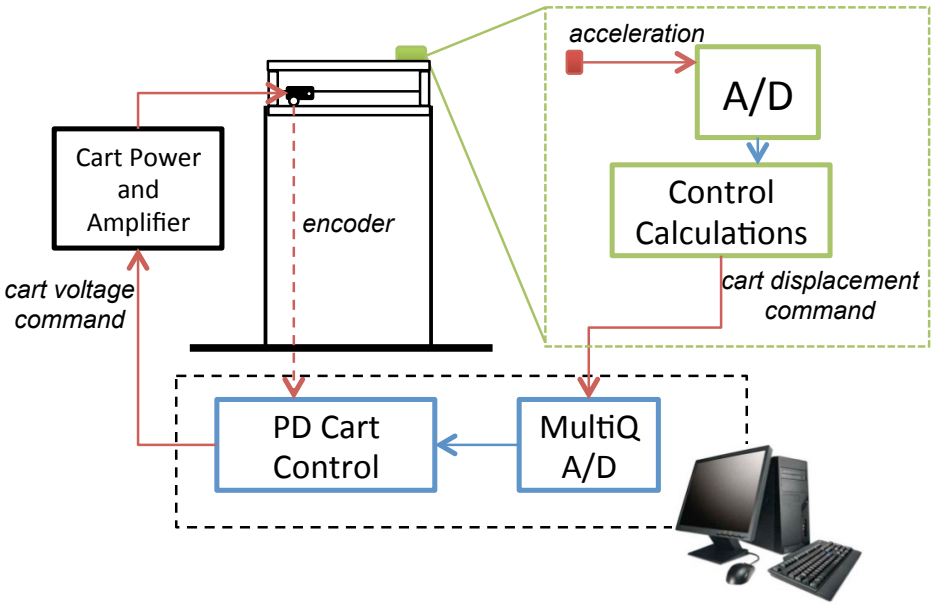

Figure 7.11: Schematic of Smart Sensor Control Experimental Setup with the SHM-A for Data Acquisition.

On the other hand, in the wireless system (Figure 7.11), the wireless smart sensor is responsible for the acceleration measurement and control calculations. The fully decentralized control implementation on the Imote2 platform (described in section 6.1) is programmed with the discrete control design discussed previously. The resulting cart displacement command is issued as an analog voltage from the SHM-D2A to the MultiQ board for the PD control of the AMD. The control computer then outputs the required voltage to the AMD, which is applied through the cart amplifier. The control computer is used for the PD control rather than the wireless smart sensor because the SHM-A cannot currently handle the encoder feedback required for displacement control.

Two other considerations in the smart sensor experimental control implementation include the accelerometer calibration and the resolution of the MultiQ A/D. The offset and scale factors of the *x*-axis on the SHM-A accelerometer were determined using static calibration (Jang and Rice 2009). Because the model was not originally identified using the SHM-A, the accelerometer measurements must be scaled appropriately for successful control implementation. The second consideration is the resolution of the MultiQ A/D. Because the required AMD displacements are small values when scaled in meters, the full voltage range of the MultiQ A/D input is not used; therefore, the 12-bit resolution of the ADC is an issue. The output was multiplied by 10 on the Imote2 prior to conversion to obtain better resolution of the command input and stay within the output range of the SHM-D2A.

Similarly, for the smart sensor experimental implementation with the SHM-SAR, the wired accelerometer output and the resolution of the MultiQ A/D need to be considered. The accelerometer output has to be appropriately shifted and scaled for use with the data acquisition board. The capacitive accelerometer offers the ability to shift the DC offset to 1.25V, or the mean of the input voltage range. The mean value is then removed in software on the Imote2 prior to control calculations. The control output is again multiplied by 10 on the Imote2 prior to conversion to obtain better resolution of the command input and stay within the output range of the SHM-D2A.

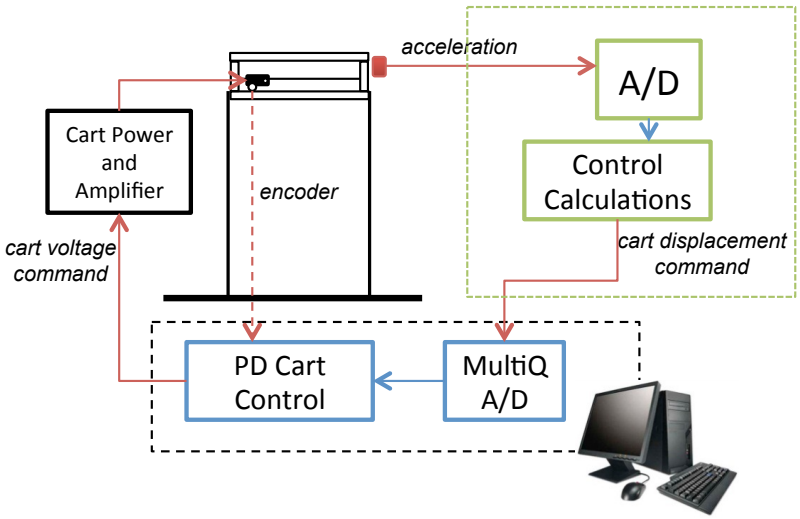

Figure 7.12: Schematic of Smart Sensor Control Experiment with SHM-SAR for Data Acquisition.

In the experiment, an initial displacement was applied to the structure and then released to obtain the free response of the structure for each control configuration. A comparison of the responses for the four configurations is provided in Figure 7.13 and the RMS accleration response is given in Table 7.2. The uncontrolled response, shown in blue, reflects the damped free response of a structure. The zeroed response, shown in red, has a significantly faster decay in the response than the uncontrolled. Therefore, the AMD with a zero command introduces significant damping to the system due to the friction and slight motion of the AMD. The wired system, shown in cyan, achieves a significant reduction in the response. The smart sensor system with the SHM-A, shown in green, achieves comparable performance to the wired system; however, the performance is not as good initially. This result is likely due to the slow sampling rate. The smart sensor system with the SHM-SAR, shown in pink, performs as well as the wired system. Thus, the discrete-time control implementation on the smart sensor was able to achieve a similar reduction in the response as the continuous-time wired controller. Additionally, the new data acquisition hardware developed for wireless structural control (SHM-SAR) outperforms the SHM-A; so, in future control experiments, only the SHM-SAR configuration will be considered.

Table 7.2: RMS Acceleration Response Comparison for Small-Scale Experimental Setup.

Experimental Configuration	RMS Acceleration Response
Uncontrolled	0.0893
Zeroed Control	0.0573
Smart Sensor Control – SHM-A	0.0430
Smart Sensor Control – SHM-SAR	0.0355
Wired Control	0.0356

In both controlled cases, the control predominantly occurs during the beginning of the response. As shown in Figure 7.13(b), the control effort alters both the magnitude and frequency of the response for the both the wired and smart sensor systems. The responses during the initial period lie within the zeroed control response and then are reduced further. At about three seconds, the control efforts are within the friction of the device and the systems return to free

response. The smart sensor control efforts are significantly lower than the wired system and still achieve comparable performance.

Overall, the experimental results highlight the successful implementation of active structural control using a wireless smart sensor platform. By properly accounting for discrete-time control design at slow sampling rates, the smart sensor implementation achieves comparable performance to the wired system.

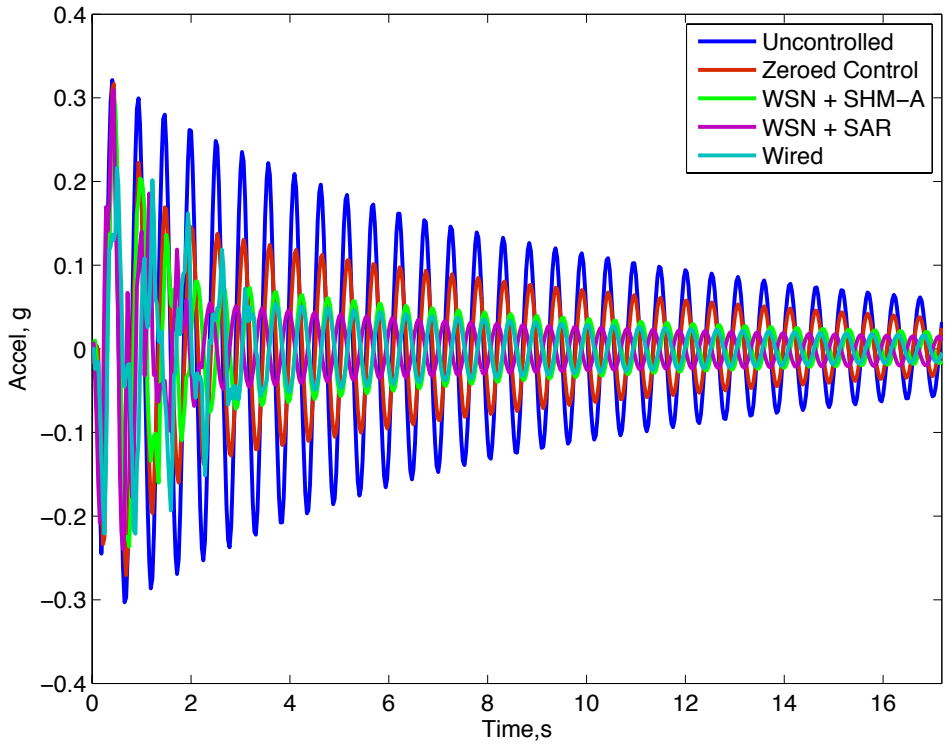

(a)

Figure 7.13: (a) Comparison of Experimental Response of Small-Scale Setup (b) Zoom Over the Region of Control.

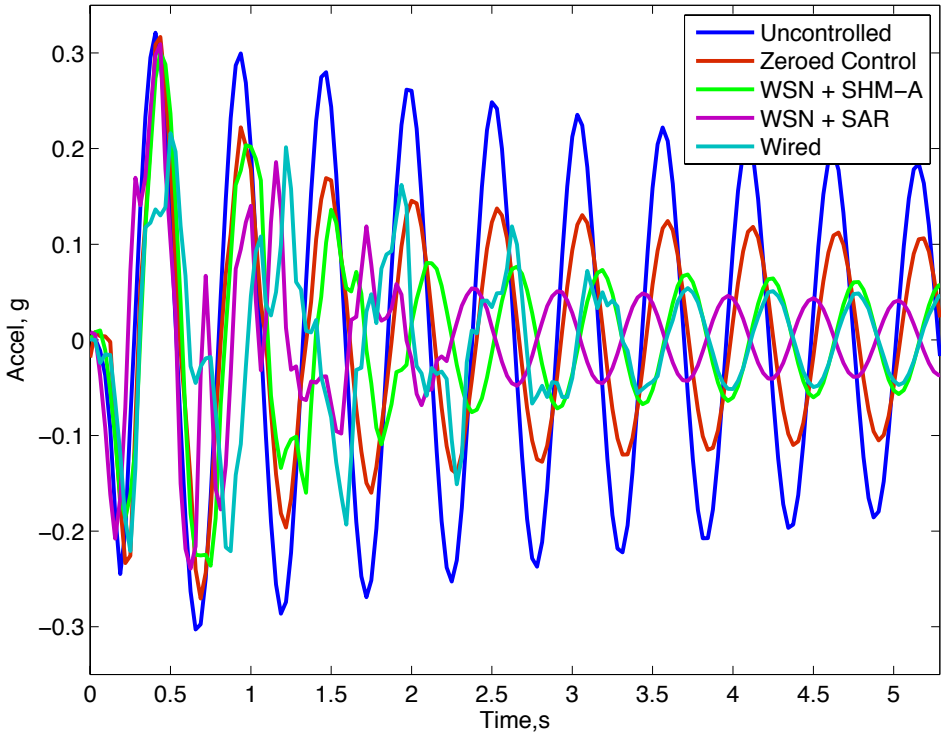

(b)

Figure 7.13 continued.

7.5 Summary

This chapter provides an overview of the wireless smart sensor platform and control algorithms used in this work. The wireless sensor hardware, specifically the ADC used, has inherent implications on the latency in the system. Thus, the data acquisition architecture should be considered. In addition, the slower sampling rate due to the latency should be accounted for in the control design. A discrete-time model, which is based on a ZOH transformation and includes an input delay, offers better performance and insight on the stability of the closed-loop system during control design. Two smart sensor control systems were compared to a wired control system on a SDOF system fitted with an active control device. The smart sensor control systems offered comparable performance to the wired system; thus, highlighting the feasibility of wireless active control. In addition, the low-latency data-acquisition was experimentally verified and outperformed the original acquisition hardware developed for SHM.

WIRELESS ACTIVE CONTROL OF A MULTI-STORY STRUCTURE

This chapter reports on the implementation of wireless smart sensors to control a multi-story structure. Two active mass dampers (AMDs) were used to control the response of a four-story structure subject to base excitation. Two control strategies were implemented on the Imote2 fitted with the updated SHM-SAR and SHM-D2A acquisition and actuation hardware for comparison. The system identification, wired control design used for comparison, and wireless control performance are presented in this chapter.

8.1 Structural System

The experimental system used in this study of wireless structural control is a four-story structure fitted with two AMD control systems on 2nd and 4th floors. The structure is comprised of components by Quanser Consulting and has an overall height of 2.2 meters. The aluminum columns have a section of 2 x 108 mm and an inter-story height of 490 mm. The mass of the second and fourth story is 1.662 kg, stories one and three have a mass of 1.15kg, and the mass of each column is 0.227 kg. The additional mass on the second and fourth stories is due to the fixtures for the AMD. A summary of the component dimensions and mass are given in Table 8.1. In addition, a small, single-axis shake table excites the structure. A custom servo-motor drives the table with a stroke of ±5 cm and encoder feedback is used for proportional derivative (PD) control of the table. The complete setup is shown in Figure 8.1.

Table 8.1: Experimental Structure Components Summary

Component	Properties
Column Dimensions	2 x 108 x 490 mm
Column Mass	0.277 kg
1st and 3rd Story Mass	1.15 kg
2nd and 4th Story Mass	1.662 kg
AMD mass	0.454 kg

The combination of the two AMDs on the second and fourth story helps limit the structural response in higher modes and offers different levels of control decentralization. Each AMD is fitted with a DC motor to move the cart along a geared track. Because the AMDs are inherently unstable systems, proportional-derivative (PD) controllers based on the optical encoder feedback are used for position control of the carts. In addition, the PD controllers can be tuned to ensure good position tracking as well as the frequencies of the control mode for each AMD.

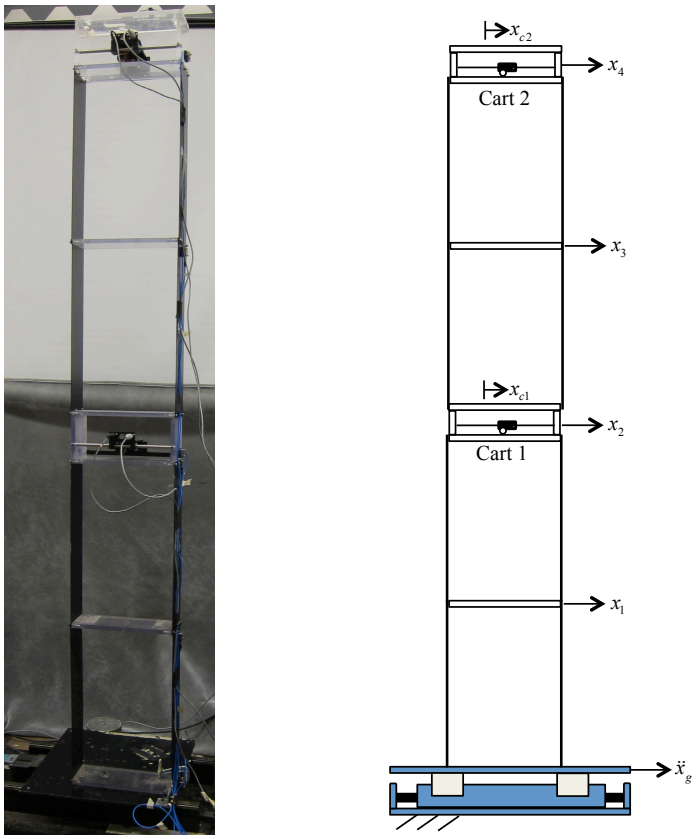

Figure 8.1: Experimental Setup (left) and Analytical Model Diagram (right).

By tuning the PD controllers, the control mode frequencies associated with each AMD can be adjusted (within reason) to have control authority over a desired range. An analytical model of the system, which included the PD control of each cart, was developed to determine the best ratio of the AMD control gains for the control of the structure. A diagram of the analytical model for reference is provided in Figure 8.1. To limit the coupling of the two controller modes, the proportional gains should not be equal. The controller gains for cart 1 and cart 2 are K_{p1} = 120, K_{d1} = 0, K_{p2} = 115, K_{d2} = 0, respectively. The resulting proportional gains, determined experimentally, ensure good tracking performance while preserving the desired relationship.

8.2 System Model

A high-fidelity system model is essential for successful control design and analysis. Unlike in Chapter 7, the multi-story system used in the experiment requires a multi-input, multi-output (MIMO) system model to capture the control inputs, base excitation inputs, and structural response. Figure 8.2 highlights the inputs and outputs modeled in the experimental setup. The three inputs are the desired displacements, u_d, of the two AMDs and the ground excitation. The measured outputs are the accelerations of each story and the AMD relative displacements. Given the MIMO nature of the system, three separate single-input multiple-output (SIMO) models are used to develop the complete system model (Chang and Spencer 2012). The SIMO models are developed from exciting the structure with each of the AMDs and shake table individually as shown in Figure 8.3. The models are then combined in two steps to develop a complete system model that captures control structure interaction.

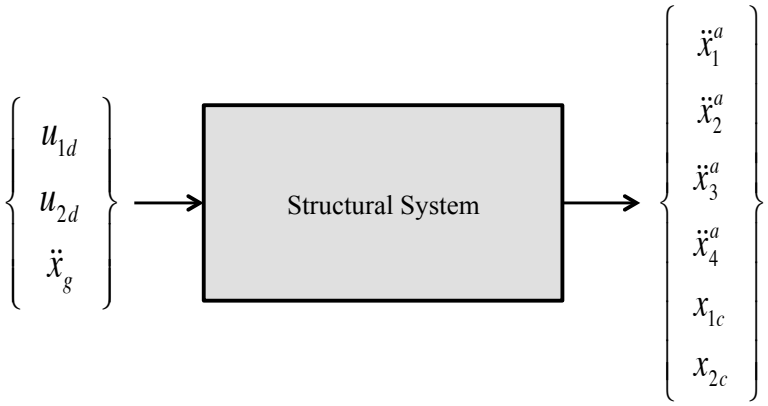

Figure 8.2: System Model Inputs and Outputs.

Identification of the system model from the AMD inputs to the structural response is the most important for control design, because the model captures how the control input will impact the system response. As a result, the two AMD SIMO systems are identified in the frequency domain and combined first. For each individual system identification, a 10 Hz band-limited white noise displacement input is commanded to the primary AMD, ten-percent of that BLWN signal is applied to the secondary AMD, and a zero command is issued to the table, as shown in Figure 8.3 (a) and (b). The smaller BLWN signal input to the secondary AMD allows any coupling of the two AMD systems to be captured and provides a more accurate representation of the damping in the system when compared to a zeroed command. The zeroed command to the table allows any table-structure interaction to be captured, which is expected to be minimal in this setup. The primary AMD command input, AMD displacements, and structural accelerations were measured using a dSpace data acquisition system and resulted in six transfer functions for each AMD.

The ground input SIMO identification is used to model how the excitation will impact the structural response. As shown in Figure 8.3(c), a band-limited white noise command is input to the shake table and the story accelerations and AMD displacements are measured. A zero command is applied to the two AMDs to capture any control structure interaction. In this case, the interaction is minimal due to the light mass of the carts and the strong PD control loops. The zeroed carts, however, introduce additional damping to the system. The measured responses resulted in six experimental transfer functions and the magnitudes of the AMD displacements are very low. The SIMO model identified from the six experimental transfer functions will ultimately be combined with the MIMO system for the two control inputs.

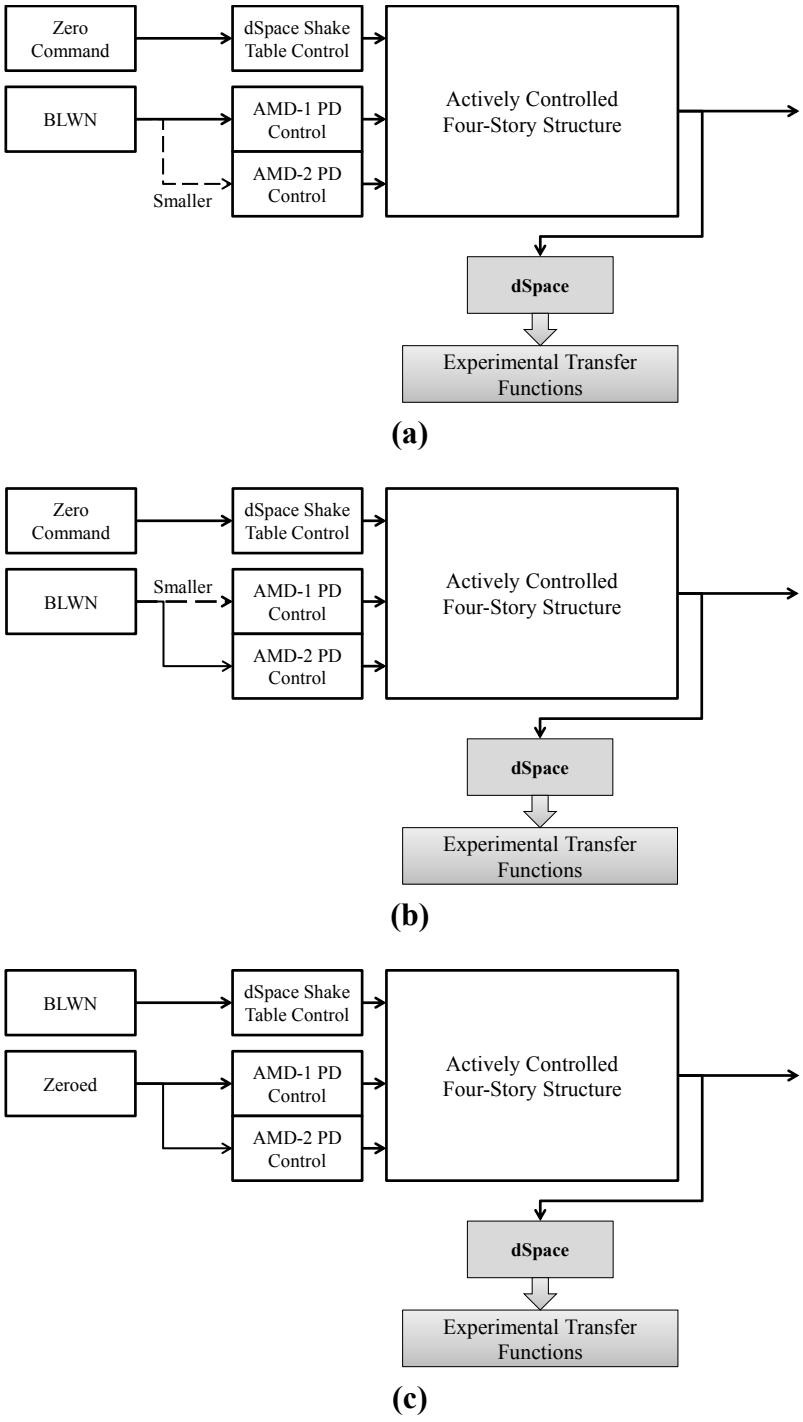

Figure 8.3: Experimental SIMO System Identifications: (a) X_{c1} Approach, (b) X_{c2} Approach, and (c) X_g Approach.

A frequency domain identification of the resulting transfer functions is used to determine the single-input models. The tool, *MFDID*, developed by Kim et al. (2005) uses a four-stage optimization process to identify the SIMO models. Although *MFDID* may be used for MIMO model identification, only SIMO systems are identified using this tool to limit pole-zero cancellation of the AMD modes, which is highly likely in this system if a MIMO approach is used initially. The number of poles and zeros is specified prior to optimization and can then be

manually tuned during post-processing to improve the fit. Using the analytical system model, the appropriate ratio of poles and zeros, as well as the number of zeros at the origin, can be determined to improve the frequency domain model fit. A screen capture of the MFID graphical user interface after optimization for AMD-1 is provided in Figure 8.4. The blue line represents the experimental transfer function and the red line is the identified model.

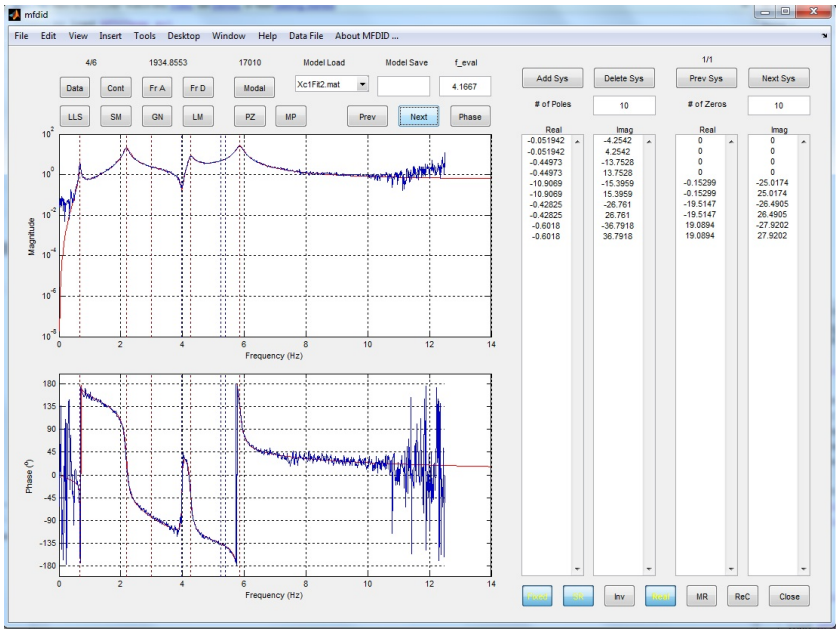

Figure 8.4: MFDID System Identification Screen Capture.

Each identified SIMO system for an AMD input includes the structural poles and the control poles for the respective AMD. Although analytically the control mode for the other AMD should be present in the SIMO system, the interaction of the two AMDs is relatively small and is not easily identified in the frequency domain. As a result, each identified system model has ten poles: eight from the structure and two from the control. The high-frequency dynamics of the DC motor are neglected and the PD control loop is incorporated in the system model. The four structural modes determined in each SIMO system have similar frequencies and real and imaginary components, which will ensure good model combination. The system combination of the two AMD SIMO models will result in a MIMO system with the four structural modes and a control mode for each AMD for a total of 6 modes, or 12 poles.

The SIMO models from the control inputs are combined to develop a MIMO model prior to combination with the ground input SIMO model, because the fidelity of the AMD input model is the most important for the control design. The identified models are combined using a modified minimal realization approach developed by Chang and Spencer (2012). The state-space representation of the SIMO models (Equations 3.4 – 3.7) are initially transformed to modal canonical form and a balance realization is performed on each repeated set of states one at a time. Once the new **A** and **B** matrices for the originally repeated states are identified, the measurement matrix, **C,** is determined. The remaining non-redundant states are added to the combined system to form the complete MIMO system. Figure 8.5 shows a comparison of the original SIMO identification for the AMD-2 command input and the combined MIMO system model for the command inputs. The original SIMO identification, shown in cyan, closely matches the experimental transfer functions in red. In addition, the combined system (blue)

successfully preserves the natural frequencies, damping, and system behavior from the SIMO system.

The identified ground input model is combined with the previously determined MIMO model to capture the effect of the ground excitation on the structural response. Because the interaction of the zeroed carts on the structural response due to the ground is small, only structural modes are present in the SIMO model identified with *MFDID*. The eight redundant states of the SIMO system are combined with the MIMO control input model using the same modified minimal realization approach. More weight is given to the control input state matrix, **A**, during the combination, because the model has a more accurate representation of the damping in the system. The total combined system model has twelve poles: eight structural poles and two poles for each controller.

The combined system results in a complete model that includes the control inputs, the ground excitation and captures any control-structure interaction. Figure 8.6-8.8 show the transfer functions of the MIMO system for the AMD-1 input, AMD-2 input, and ground excitation, respectively. The model matches the poles and damping well for the AMD inputs. Some errors are present in the zeros and at the origin; however, the model matches the overall pole-zero behavior well. In addition, the transfer functions from each AMD input to its own AMD displacement capture the control-structure interaction phenomena. On the other hand, the transfer functions from each AMD input to the other AMD displacement are small in magnitude, due to their limited interaction given the strong PD control of the AMDs. In general, the small magnitude relationships are hard to represent in the model due to the resolution, but any discrepancies are reasonable if the model magnitude remains small. Furthermore, the poles of the ground input transfer function are slightly shifted to the left due to the smaller damping captured in the model than is present when the AMDs are zeroed. However, the magnitude of the transfer function and the system behavior due to a ground excitation input is captured in the model. The identified frequencies and damping are provided in Table 8.2. The third and fourth natural frequencies are associated with high damping because they are from the control systems. Overall, the identified model is a highly accurate model of the experimental system over the frequency range of interest.

Table 8.2: Identified Natural Frequencies and Damping of the Experimental Setup.

Natural Frequencies (Hz)	Damping Ratio (%)
0.68	1.34
2.19	3.05
2.76	56.65
3.00	57.80
4.25	1.48
5.86	1.64

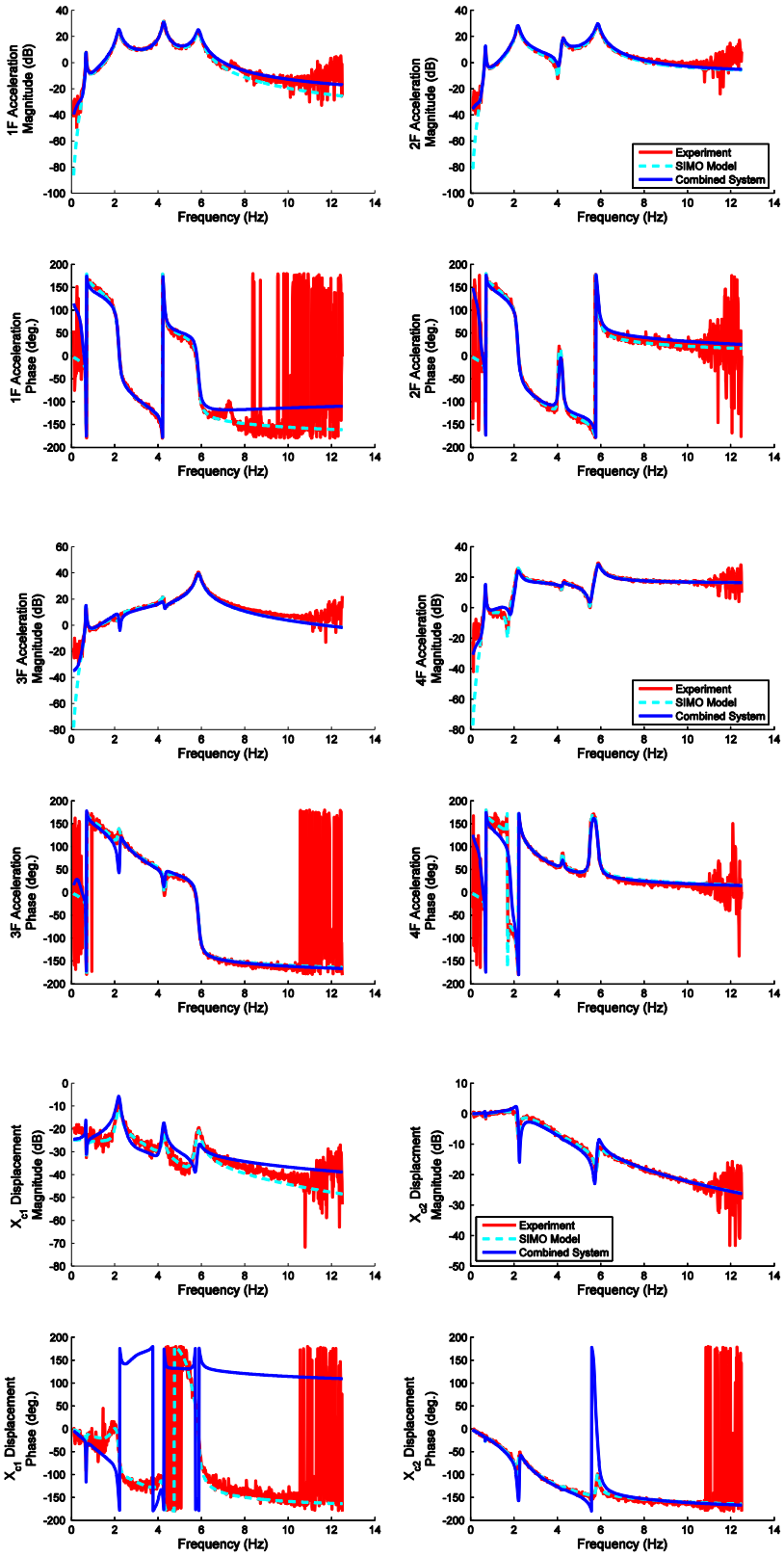

Figure 8.5: Combined Identified System Model for Control Inputs - X_{c2} Command Input

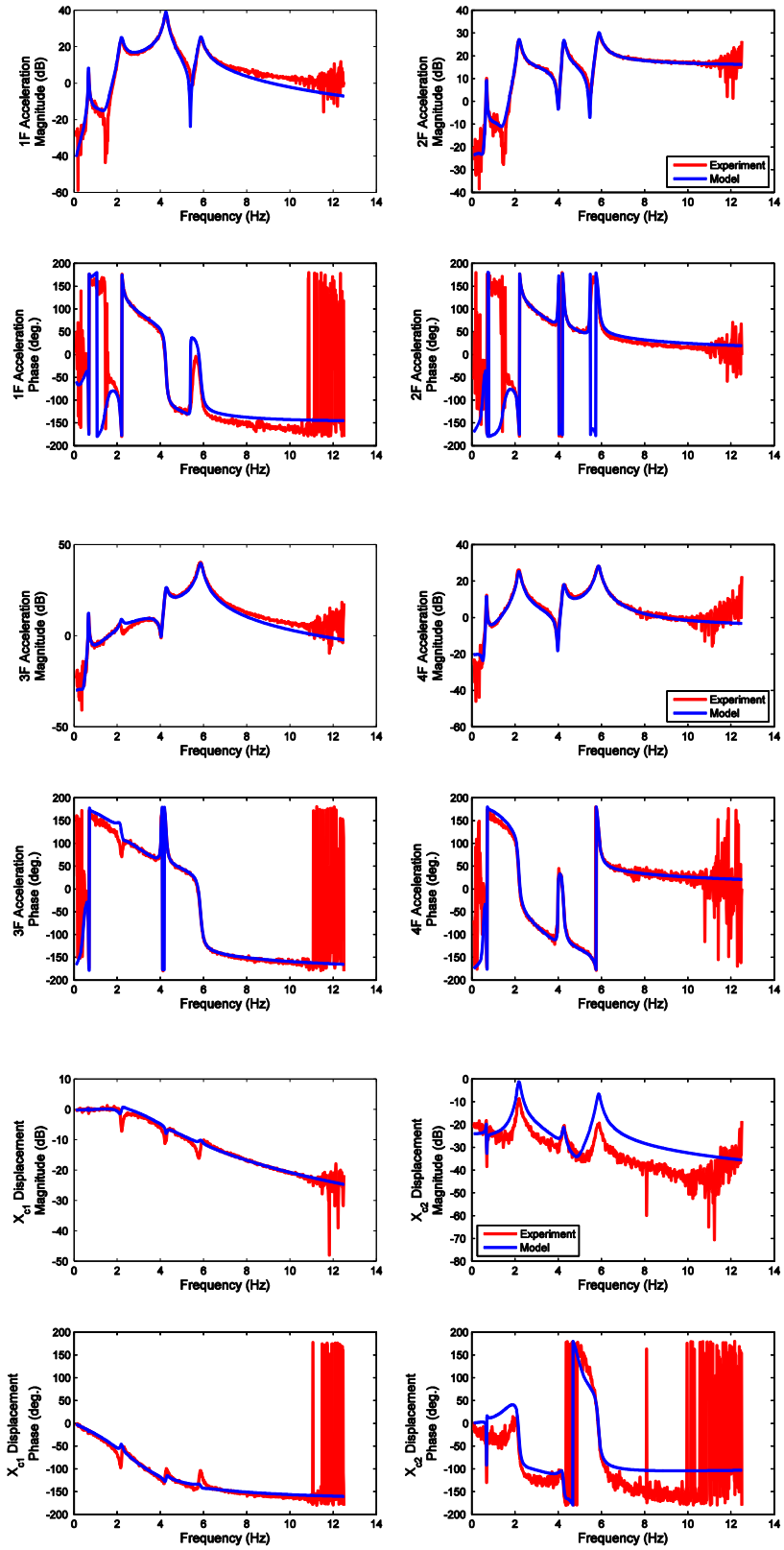

Figure 8.6: Transfer Functions of the MIMO System from AMD -1 Input.

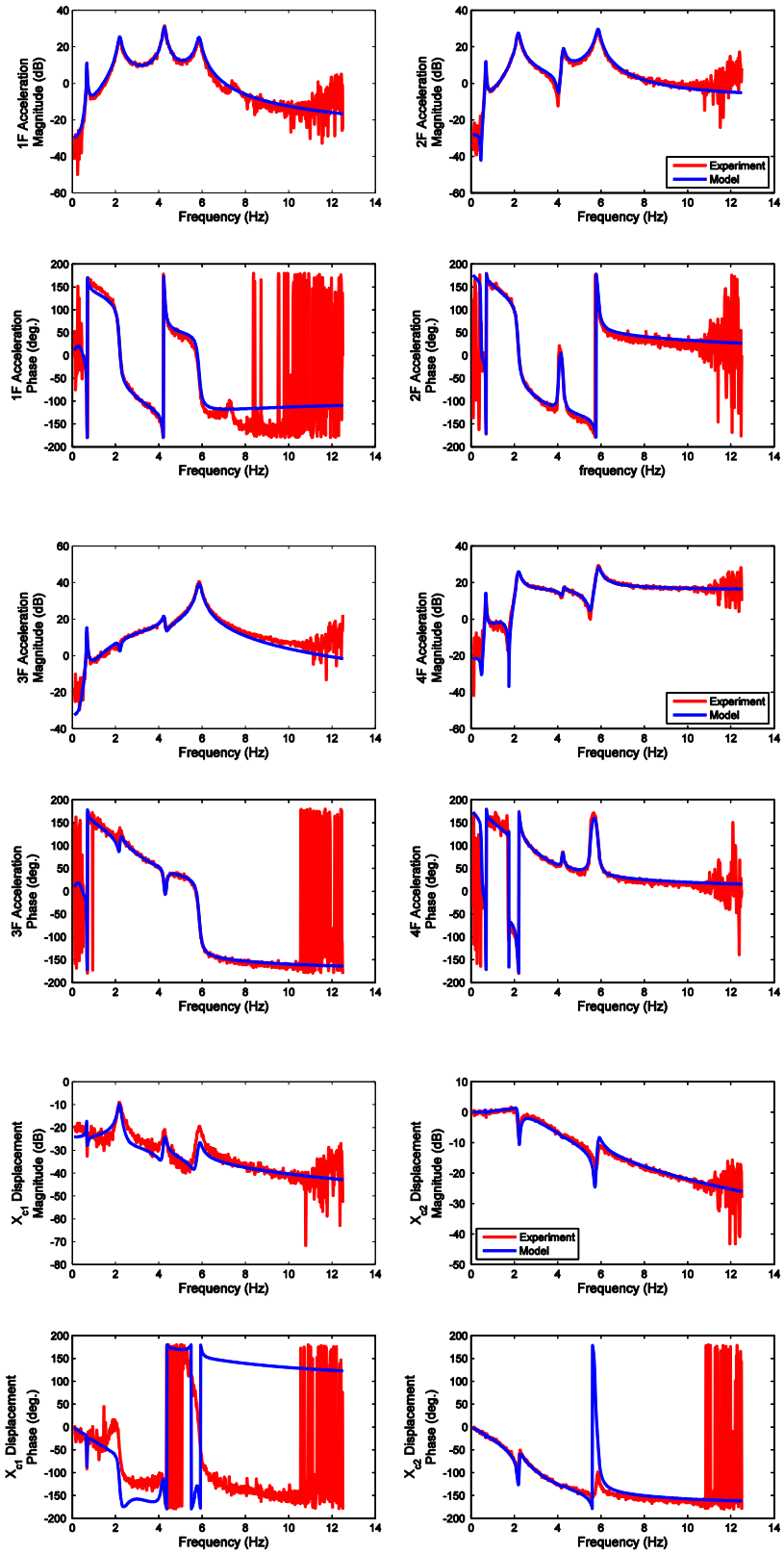

Figure 8.7: Transfer Functions of the MIMO System from AMD-2 Input.

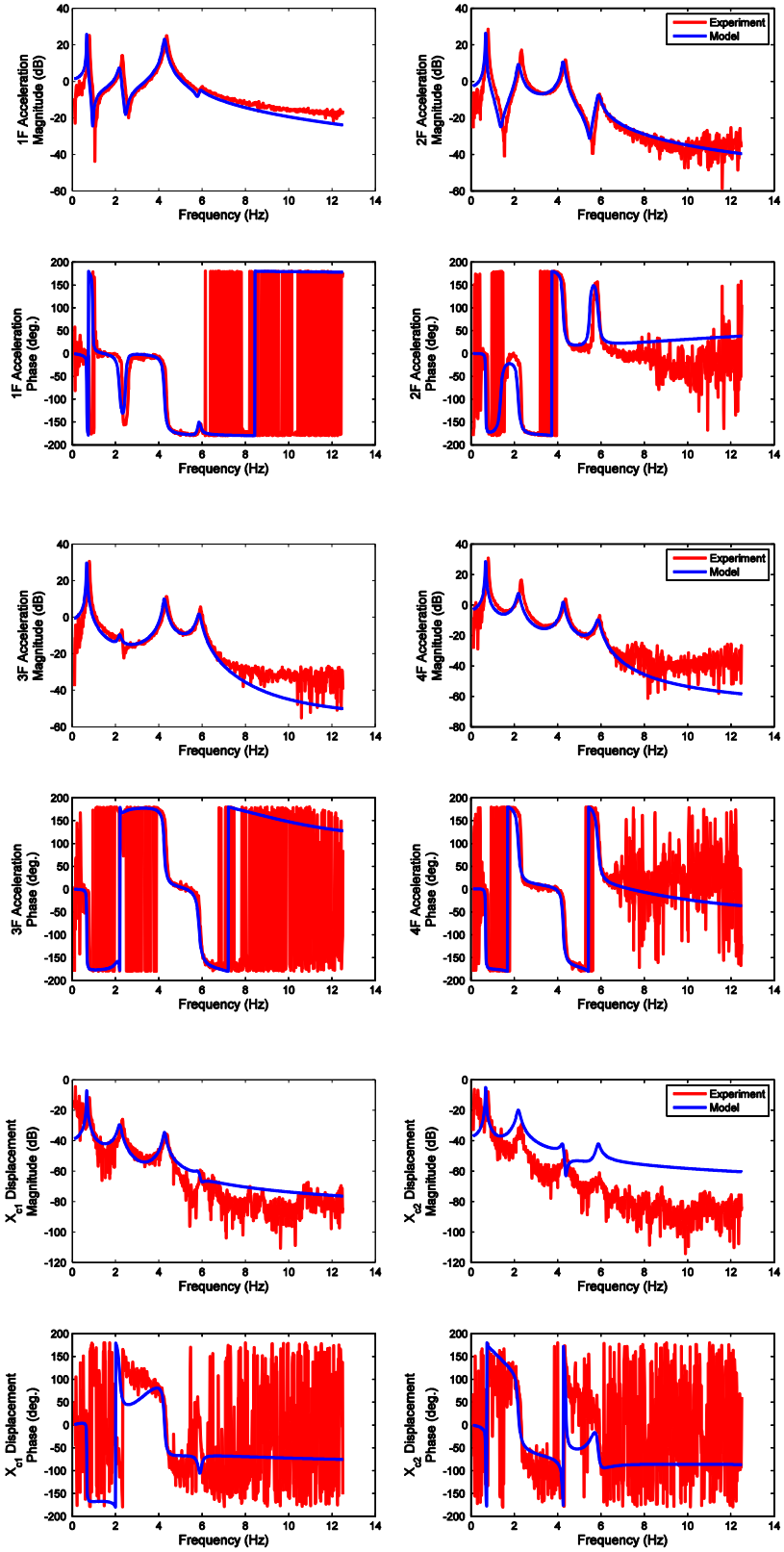

Figure 8.8: Transfer Functions of MIMO model from Ground Excitation Input.

In addition, the PD controllers of the AMD systems resulted in the desired mode shapes and natural frequency distribution. The identified mode shapes of the system are illustrated in Figure 8.9; the blue line is the real component and the dashed red line is the imaginary component. The third mode represents the control mode for AMD-2 and the fourth mode represents the control mode for AMD-1. Despite the similar mass of the carts, the different proportional gains resulted in the two distinct control modes. Also, the frequency of the AMD-1 control mode is greater, which will help in the control of higher frequency modes. Therefore, the behavior of the analytical model used for the gain selection mirrors the experimental setup.

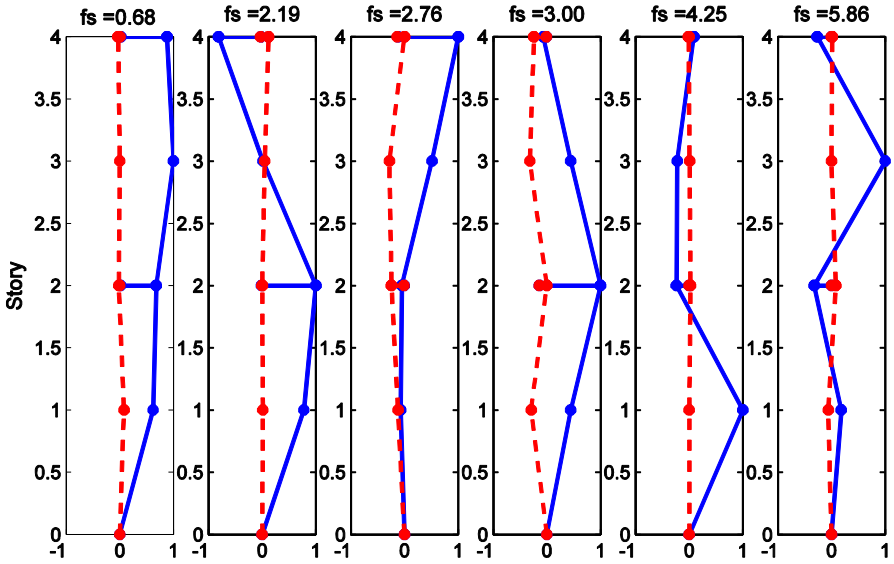

Figure 8.9: Identified Mode Shapes and Associated Natural Frequencies.

8.3 Wired Control Design

A wired control system is used for comparison with the wireless sensor control implementations. The wired control system operates at 1000 Hz and, as such, is approximated as a continuous system during the control design. The control designs explored is this section are used to inform the discrete control designs outlined in the following sections for the wireless smart sensors.

Two main approaches to the control system model are considered in the design of the feedback controller. In the first approach, which is illustrated as Case A in Figure 8.10, the model developed in section 8.2 is used as the system for design. The two inputs to the system are the ground excitation, $\ddot{x}_g$, and control input, u. In the second approach, an input-shaping filter is added to the system model to form an augmented system for control design. The shaping filter focuses the control effort to a narrower band of frequencies of interest. As shown in Figure 8.11, a filter on the inputs shapes a wide band excitation, w, to model the frequency content of an earthquake excitation. A Kanai-Tajimi filter is used in Case B to shape the wide-band excitation. The Kanai-Tajimi filter equations are given in equation (8.1); and, the filter properties are ω_g = 5.27 rad/sec and ζ_g = 80% in order to focus the control on the first two modes of the systems. The augmented system with the input shaping filter will include two additional states due to the filter. These two control system cases are used in the feedback control design for comparison.

$$\ddot{a} + 2\zeta_g \omega_g \dot{a} + \omega_g^2 a = w(t)$$
$$\ddot{x}_g = -2\zeta_g \omega_g \dot{a} - \omega_g^2 a \tag{8.1}$$

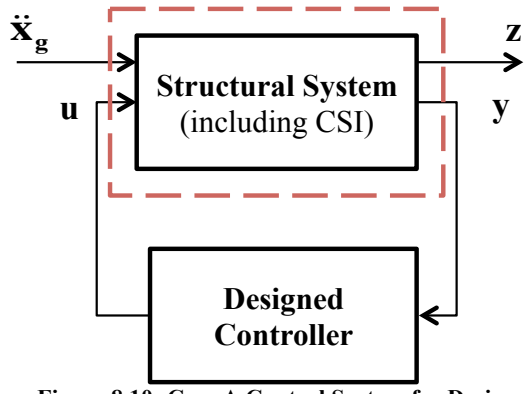

Figure 8.10: Case A Control System for Design.

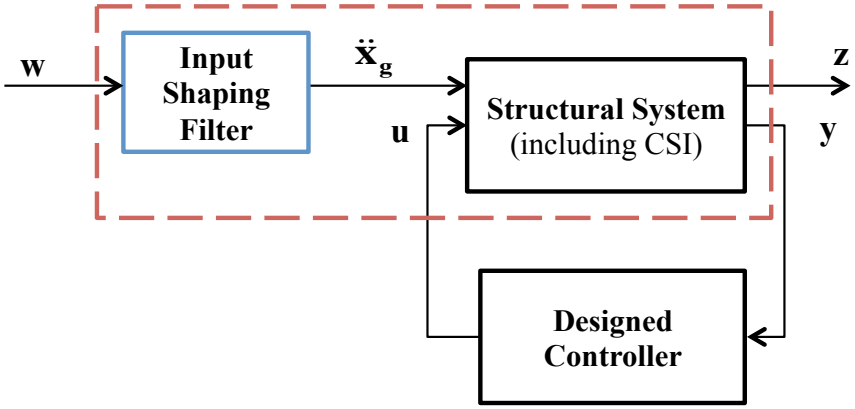

Figure 8.11: Case B Control System for Design.

Given the system identification, only acceleration measurements, *y*, are available for feedback control; as a result, a Linear Quadratic Gaussian (LQG) regulator is used. Based on the separation principle, the Linear Quadratic Regulator (LQR) and Kalman estimator are designed separately (Section 3.4). Two LQR control weightings are considered. In the first, the two AMD controllers weighted equally. In the second, the fourth-story AMD, AMD-2, is given more control authority. Two Kalman filter measurement weightings are considered as well. The first weights all acceleration measurements equally; and, the second places less weight on the measurements from the second and fourth story, due to the noisier measurements caused by the motion of the cart. A summary of the control designs considered is given in Table 8.3. In total, eight different LQG controllers are considered.

Table 8.3: Control Design Weighting Summary.

Shaping Filter	LQR Weighting	Kalman Weighting
Case A – No Shaping	(a) $\mathbf{Q} = \mathbf{I},\ \mathbf{R} = \begin{bmatrix} r_1 & 0 \\ 0 & r_1 \end{bmatrix}$	(1) $\mathbf{S}_v = diag\left(\begin{bmatrix} 1 & 1 & 1 & 1 \end{bmatrix}\right)$
Case B – Input Shaping	(b) $\mathbf{Q} = \mathbf{I},\ \mathbf{R} = \begin{bmatrix} r_1 & 0 \\ 0 & 0.5r_1 \end{bmatrix}$	(2) $\mathbf{S}_v = diag\left(\begin{bmatrix} 1 & 1000 & 1 & 1000 \end{bmatrix}\right)$

The LQR control design is selected to minimize the root mean square (rms) acceleration response with the least rms control effort. The control performance for the calculated feedback control gain is determined using the Lyapunov equation to calculate the rms response when full state knowledge is known. The broadband system input is modeled in the frequency range of interest using a Kanai-Tajimi spectrum with ω_g = 15 rad/sec and ζ_g = 30%. The rms acceleration response and rms control effort are calculated for a range of control weightings, r_1, and each **R** weighting matrix (Table 8.3). The calculated acceleration response versus the required control effort for AMD-1 is plotted for each shaping filter case (A or B) in Figure 8.12 and Figure 8.13. The four lines for each weighting matrix are for the acceleration of each of the four stories. The plots show that case b, which gives AMD-2 more control authority, reduces the rms accelerations of the story with less control effort for both shaping filter cases. As a result, this weighting matrix is chosen. Also, as the control weighting, r_1, is lowered, eventually there is little response reduction despite a significant increase in the rms control effort. The control weightings that result in the lowest rms acceleration without a significant increase in the control effort for Case b are selected for the LQR design.

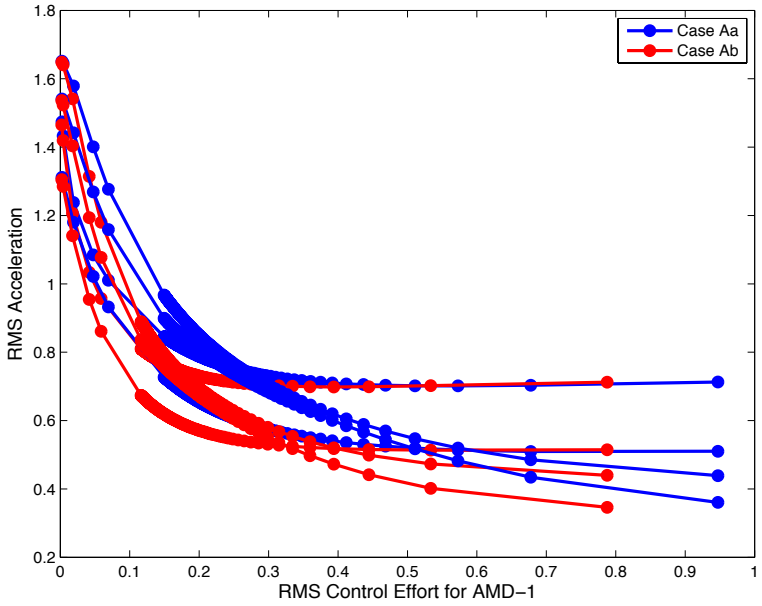

Figure 8.12: LQR Control Performance Summary for Case A and AMD-1.

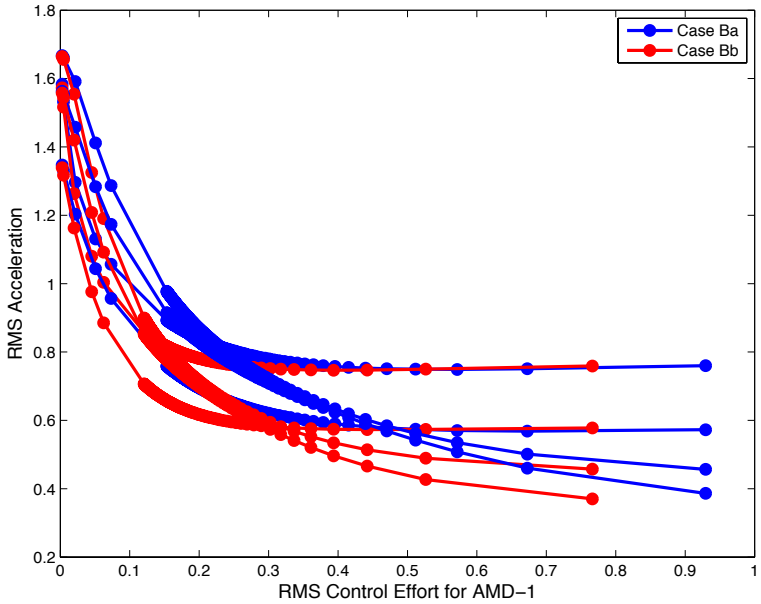

Figure 8.13: LQR Control Performance Summary for Case B and AMD-1.

The Kalman filter design is selected to recover the performance of the LQR controller when there is full-state knowledge. The ratio of the closed loop LQG response to the closed loop LQR response is calculated with the Lyapunov equation for a range of process noise weighting, S_w, values. Figure 8.14 and Figure 8.15 show the calculated response ratio versus the process noise weighting for the two measurement-noise weighting cases for each shaping filter case, respectively. The process noise weighting at which the response ratio stabilizes is selected for the design, because too high a weighting can ultimately cause much poorer estimator performance in the presence of measurement noise.

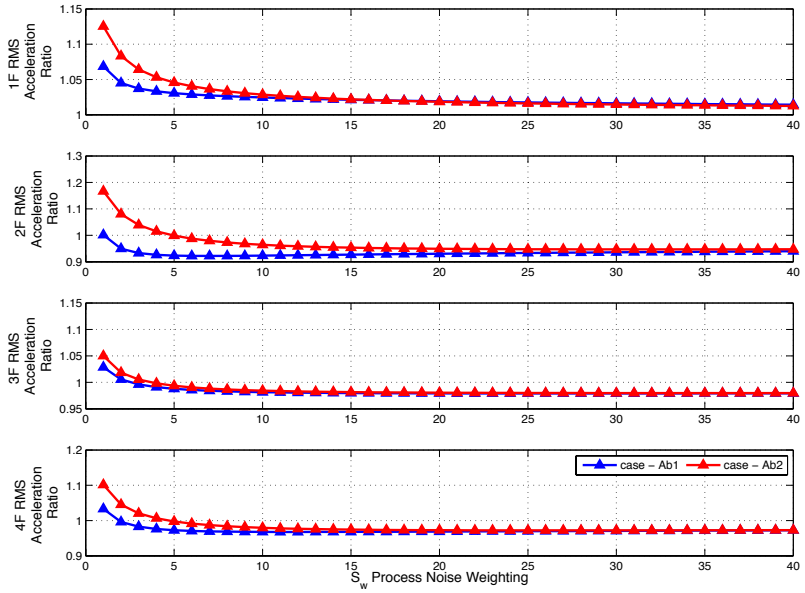

Figure 8.14: Case A Kalman Filter Performance Recovery for Process Noise Weighting Values.

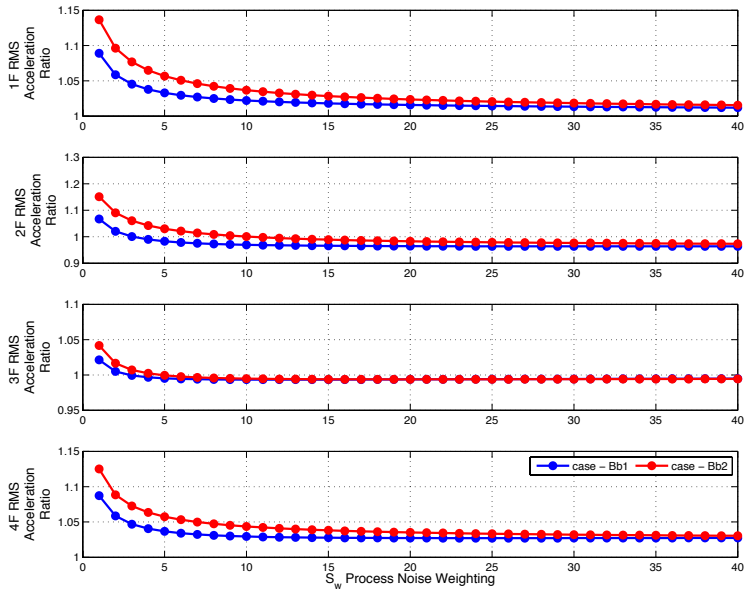

Figure 8.15: Case B Kalman Filter Performance Recovery for Process Noise Weighting Values.

Prior to selecting final design values the loop gain and sensitivity transfer functions are used to evaluate the stability of the controller design. As shown in Figure 8.16, the loop gain is determined by looking at the open loop performance of the system. The sensitivity transfer function is the identity matrix minus the loop gain.

$$L(s) = H_{uy}H_{yu}$$
$$S(s) = \mathbf{I} - H_{uy}H_{yu} \tag{8.2}$$

The loop gain and sensitivity functions should be high in regions of high authority or system knowledge. However, the loop gain should be really small in areas of uncertainty. For example, a small magnitude loop gain in the higher frequency range can help with noise rejection. Similarly, the sensitivity function should be close to unity in areas of uncertainty. The loop gains, plotted in Figure 8.17, are high in the regions of good system knowledge and roll off at high frequencies for good noise rejection. Similarly, the sensitivity transfer function is unity at high frequencies (Figure 8.18). Because these two control designs exhibit good performance and stability, they were implemented experimentally. The final wired designs are presented in Table 8.4.

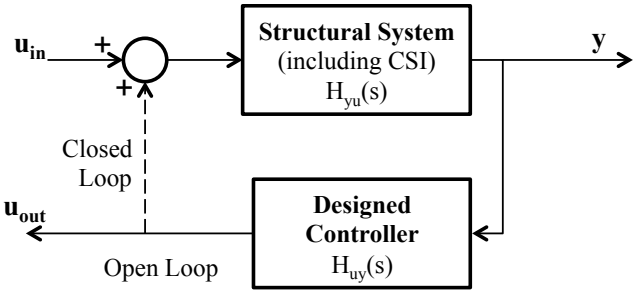

Figure 8.16: Representation of the Loop Gain Calculation.

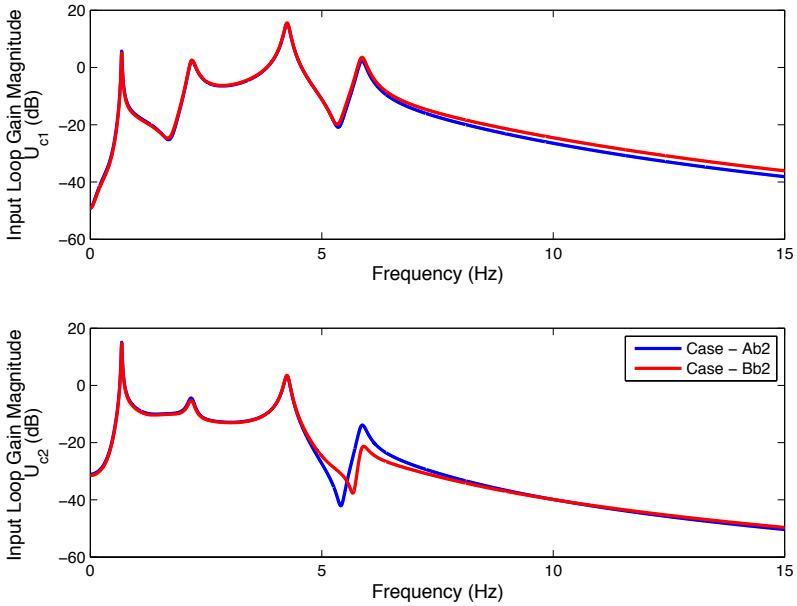

Figure 8.17: Loop Gain Magnitudes for Case A and B Control Designs.

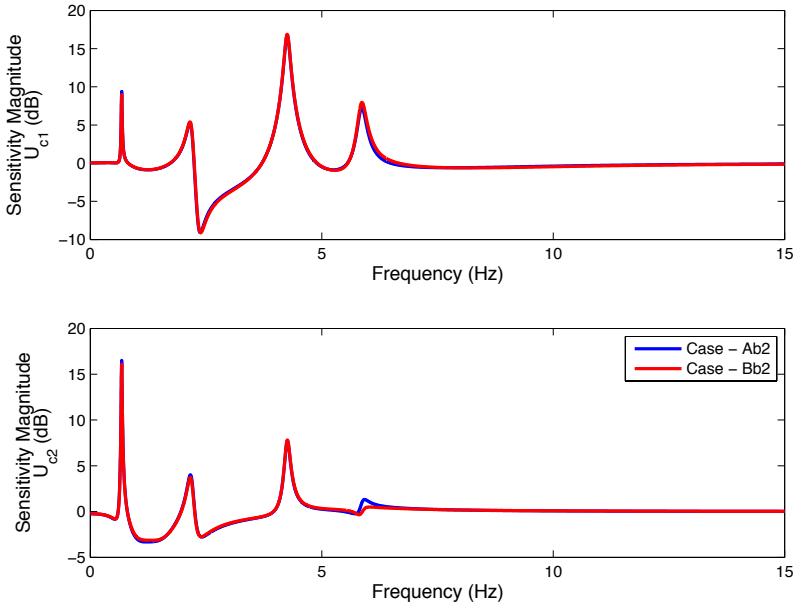

Figure 8.18: Sensitivity Transfer Function Magnitude for Case A and B Designs.

Table 8.4: Wired Control Design Weightings.

Shaping Filter	LQR Weighting	r_1	Kalman Weighting	S_w
Case A – No Shaping	(b) $\mathbf{Q} = \mathbf{I}, \mathbf{R} = \begin{bmatrix} r_1 & 0 \\ 0 & 0.5r_1 \end{bmatrix}$	2.512	(2) $\mathbf{S}_v = diag\left(\begin{bmatrix} 1 & 1000 & 1 & 1000 \end{bmatrix}\right)$	15
Case B – Input Shaping	(b) $\mathbf{Q} = \mathbf{I}, \mathbf{R} = \begin{bmatrix} r_1 & 0 \\ 0 & 0.5r_1 \end{bmatrix}$	2.914	(2) $\mathbf{S}_v = diag\left(\begin{bmatrix} 1 & 1000 & 1 & 1000 \end{bmatrix}\right)$	15

8.4 Centralized Control Design for Wireless Smart Sensors

A design methodology similar to that outlined in Section 8.3 is used to develop the centralized control design for the wireless smart sensor implementation; however, the control design is developed in discrete-time due to the slow sampling rate. In addition, an input delay will be included in the design based on the conclusions from Chapter 7. This section will outline the control design for the centralized system implemented on the wireless smart sensor network.

As discussed in Chapter 6, the resulting sampling rate is a function of the number of wireless communications and the number of states in the control design. In this centralized scheme, four nodes will communicate with the controller node requiring at least 32 milliseconds. An initial communication offset for the computational load on the processor is used to improve the communication reliability. The communication and this small offset results in a sampling interval of about 33 milliseconds or a rate of 30 Hz. The controller will be designed in discrete-time at this 30 Hz rate.

Initially the set of control weightings outlined in Table 8.3 were considered for the control design. For Case A, the system model identified in section 8.2 was converted to discrete time and an input delay was included in the system model prior to control design. The system consists of the original twelve states and an additional delay state for each control input. For Case B, the Kanai-Tajimi filter was converted to discrete time prior to combination with the discrete system model to form the augmented system for design. In this case, the input-shaping filter adds an additional two states to the model. Because the input-shaping filter has little impact on the control performance in the wired control system, the additional computation load due to the filter states was deemed unnecessary. Thus, only Case A is considered for the wireless control implementations.

The LQR design is selected to minimize the rms structural accelerations with the least rms control effort. The control feedback gain is initially designed assuming full-state feedback. A discrete Lyapunov equation is used to determine the rms acceleration response and control effort for the closed loop system. The covariance of the state

$$\mathbf{R}_x(k) = \varepsilon\left\{\mathbf{x}(k)\mathbf{x}^T(k)\right\} \tag{8.3}$$

and at k+1

$$\begin{aligned} \mathbf{R}_x(k+1) &= \varepsilon\left\{\mathbf{x}(k+1)\mathbf{x}^T(k+1)\right\} \\ &= \Phi_{cl}\mathbf{R}_x(k)\Phi_{cl}^T + \Gamma\mathbf{R}_w(k)\Gamma^T \end{aligned} \tag{8.4}$$

so, at steady state

$$\mathbf{R}_x(\infty) = \Phi_{cl}\mathbf{R}_x(\infty)\Phi_{cl}^T + \Gamma\mathbf{R}_w\Gamma^T \tag{8.5}$$

Using the formulation above, the discrete Lyapunov equation can be used solve for the steady-state response, which can then be used to determine the rms acceleration response and control effort (Franklin et al. 1998). Figure 8.19 shows the rms acceleration response versus the rms control effort for a range of control weightings, r_1, and the two weighting cases for **R**. Case b, where the controller on the fourth story is given more authority, offers better performance with the same control effort. As the control cost weighting decreases, eventually the control effort significantly increases with little reduction in the rms acceleration response. For the second story, the larger control effort actually starts to increase the response. The control weighting selected is at the minimum of these curves, where the control performance is best for the amount of control effort required.

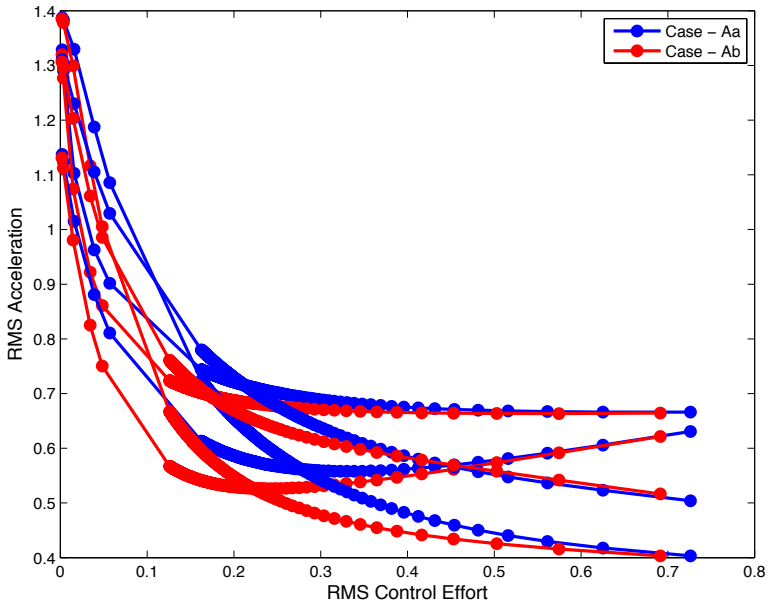

Figure 8.19: Centralized Wireless Control LQR Design Summary.

The Kalman estimator is designed to recover the performance of the LQR control design, which assumed full-state feedback. A predictor-corrector form of the estimator is designed to reconstruct the full-state based on acceleration measurements. The ratio of the closed loop responses with the LQG system to the closed loop response with the centralized LQR control design is determined for a range of process noise weightings, S_w, using the discrete Lyapunov equation. Figure 8.20 shows the results for the two different measurement noise weighting matrices. At the slow sampling rate and with only story accelerations for feedback the original LQR performance cannot be completely recovered; however, the performance of the centralized LQG controller is able to closely match that of the original centralized LQR design. The process noise weighting when the response ratio levels off is selected for the design.

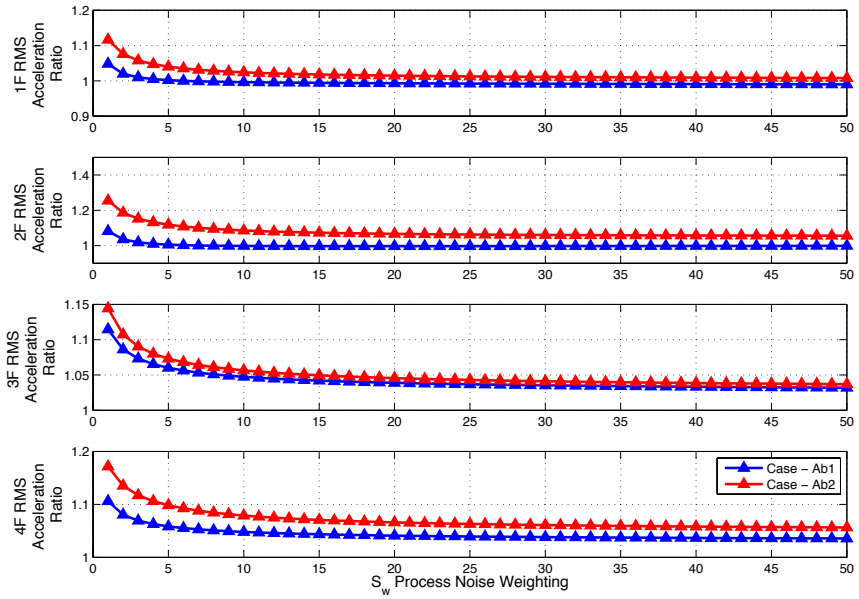

Figure 8.20: Centralized Control Kalman Estimator Design Summary.

As was done previously, prior to experimental implementation the stability of the two estimator designs is evaluated with the loop gain and sensitivity transfer functions. Figure 8.21 shows the loop gain transfer function magnitude for the two estimator designs. Although the equal weighting of the measurements appeared to be more effective in the Kalman filter design, the roll-off of the loop gain at higher frequencies is much slower. Therefore, to improve the stability of the system in areas with higher noise and less system knowledge, the second estimator will be used. Furthermore, the sensitivity transfer function magnitude, given in Figure 8.22, is unity in the higher frequency range. Without evaluating the loop gain, a complete view of the stability and performance of the centralized LQG control design would not have been available.

Although the same measurement feedback is available in the centralized control design as in the wired system, the resulting control design is very different due to the slow sampling rate and discrete-time design. The final centralized control design parameters are:

$$\mathbf{Q} = \mathbf{I}_{4x4} \ , \mathbf{R} = \begin{bmatrix} 1.8 & 0 \\ 0 & 0.9 \end{bmatrix} , S_w = 10 \ , \mathbf{S}_v = diag\left(\begin{bmatrix} 1 & 1000 & 1 & 1000 \end{bmatrix} \right)$$

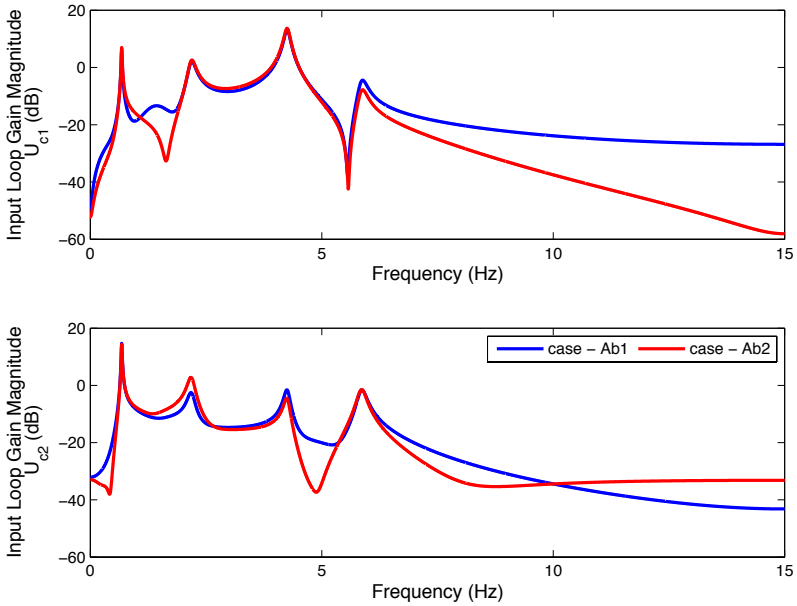

Figure 8.21: Centralized Control Design Loop Gain Transfer Functions.

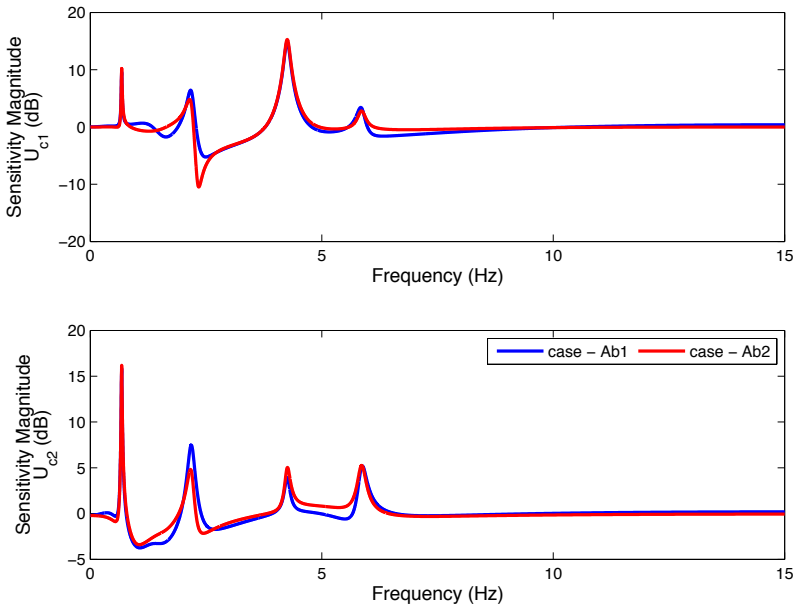

Figure 8.22: Centralized Control Design Sensitivity Transfer Functions.

8.5 Fully Decentralized Control Design for Wireless Smart Sensors

In the decentralized control approach, independent controllers are located at each AMD for a total of two control nodes (Figure 8.23). Because an LQG control approach is required and the controllers are not collocated with each system measurement, a heuristic algorithm enforcing a sparsity pattern on a global control design is not advantageous. As a result, the system is divided into two subsystems, and the controller is designed for each subsystem (Loh et al. 2007). Each

controller only has the feedback of the local acceleration measurement, and no communication is allowed among the controller nodes.

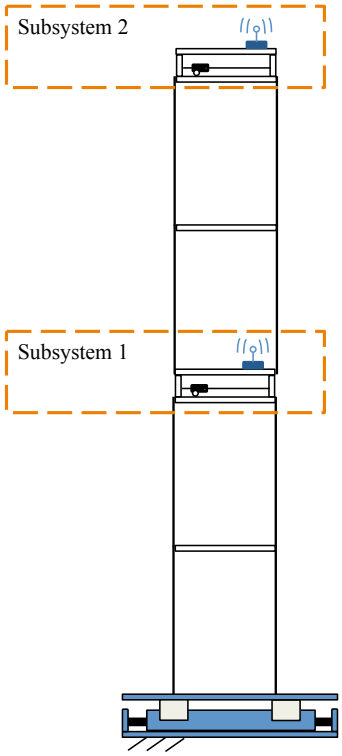

Figure 8.23: Decentralized Control Subsystems.

Although the decentralized control implementation is similar to Chapter 7, the larger system size will reduce the maximum sampling rate of the wireless smart sensors. The number of states processed in the LQG controller increases from five to fourteen, which significantly increases the computational burden on the processor. As a result, the sampling rate of the decentralized system is 725 Hz. However, this sampling rate is more than adequate for the structural system and is still significantly higher than previous wireless decentralized control implementations outlined in Chapter 2.

Initially the LQR design is determined for each subsystem assuming full-state feedback. The discrete-time model is divided into two subsystems as

$$\begin{aligned} \mathbf{z}_d[k+1] &= \Phi \mathbf{z}_d[k] + \sum_{i=1}^{2} \Gamma_i u_i[k] + \mathbf{G}\ddot{x}_g[k] \\ y_j[k] &= \left(\mathbf{C}_d\right)_j \mathbf{z}_d[k] + \left(\mathbf{D}_d\right)_j \ddot{x}_g[k] + \sum_{i=1}^{2} \left(\mathbf{F}_d\right)_{j,i} u_i[k] \end{aligned} \tag{8.6}$$

where j = 2,4 for the acceleration measurement at the second and fourth stories, respectively. A cost function used to determine the control gain for each subsystem weights the complete system state response and the local control effort

$$J_i = \sum_{k=\text{inital time}}^{k\to\infty} \mathbf{z}_d^T[k]\mathbf{Q}\mathbf{z}_d[k] + u_i^T[k] R_i u_i[k] \tag{8.7}$$

where the weighting R can be different for each AMD subsystem. Similar to the previous control designs, two ratios of the control weighting, R_i, are considered. In case a, the weighting is equal; and, in case b, the weighting on second subsystem is half of the first subsystem. The two compensators are combined with the system model to evaluate stability of the global system and determine the control performance with the discrete Lyapunov equation. Because only local stability is guaranteed in the subsystem control design, the stability of the complete system must be determined initially by looking at the closed-loop eigenvalues. In Figure 8.24, the rms acceleration response is plotted versus the rms control effort for a range of control weighting values that resulted in a stable system. The concave portion of the curves near the origin is because the individual subsystem designs do not necessary result in optimal global control. However, similar to the previous control designs, eventually the reduction in the rms acceleration response is limited despite an increase in the rms control effort. Also, case b results in better control given the same level of control effort. The weighting value, $r_1 = 9$, at which the case b controller minimizes the response with a reasonable level of control effort is selected for the LQR control design.

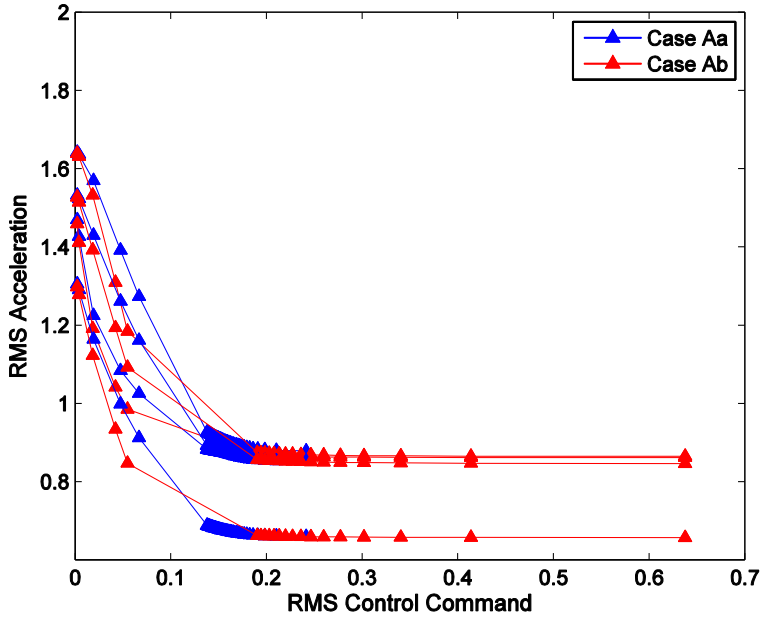

Figure 8.24: Fully Decentralized Control System LQR Design.

A Kalman estimator is designed for each subsystem given the individual measurement and knowledge of only the local control input. A predictor-corrector type Kalman filter is designed for each measurement in equation (8.6) to reconstruct the full state of the system. Because only one measurement is available, the measurement noise, S_v, is kept constant and the process noise is varied equally in both estimator designs. Despite the lack of measurement feedback, the Kalman estimators are able to reproduce the performance of the LQR control design, which assumed full-state feedback (Figure 8.25). The process noise value selected, $S_w = 4$, is where the ratio is close to one for all acceleration ratios and most have stabilized. Given the lack of measurement feedback and the high fidelity system model, a very high process noise weighting value should not be selected for the fully decentralized controller.

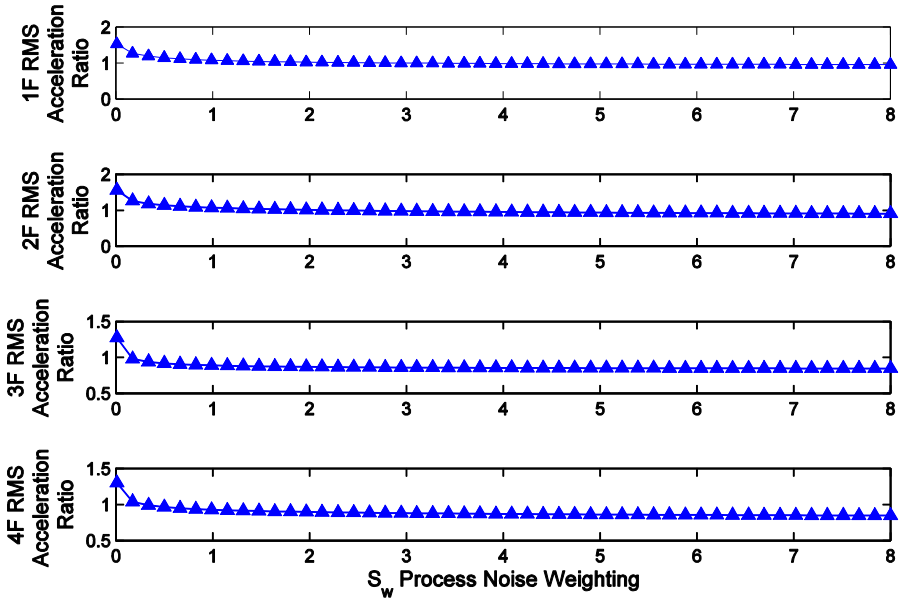

Figure 8.25: Kalman Estimator Designs for Fully Decentralized Control System.

Stability of the fully decentralized control system is a significant concern, because only subsystem stability is guaranteed. The loop gain and sensitivity transfer functions for the selected control design offer good insight on the performance of the closed loop system. The loop gain, shown in Figure 8.26, does roll off at higher frequencies, but this roll-off is very slow. Similarly, the sensitivity transfer function magnitude slowly approaches unity at higher frequencies (Figure 8.27). Therefore, although the system is stable, there could be poor noise rejection at higher frequencies. Despite the stability concerns, the robustness to node failure and the higher sampling rate make the fully decentralized control approach attractive for implementation.

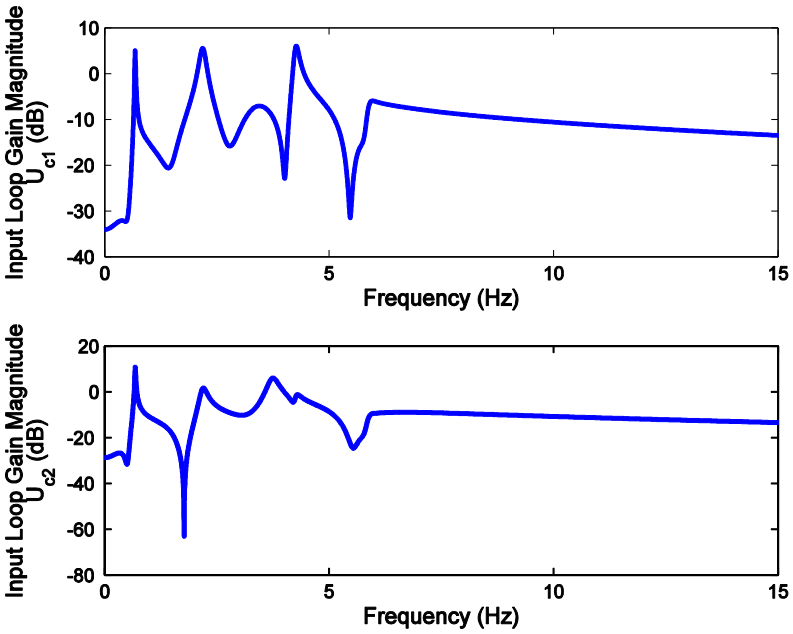

Figure 8.26: Loop Gain Transfer Functions Magnitude for Fully Decentralized Control Design.

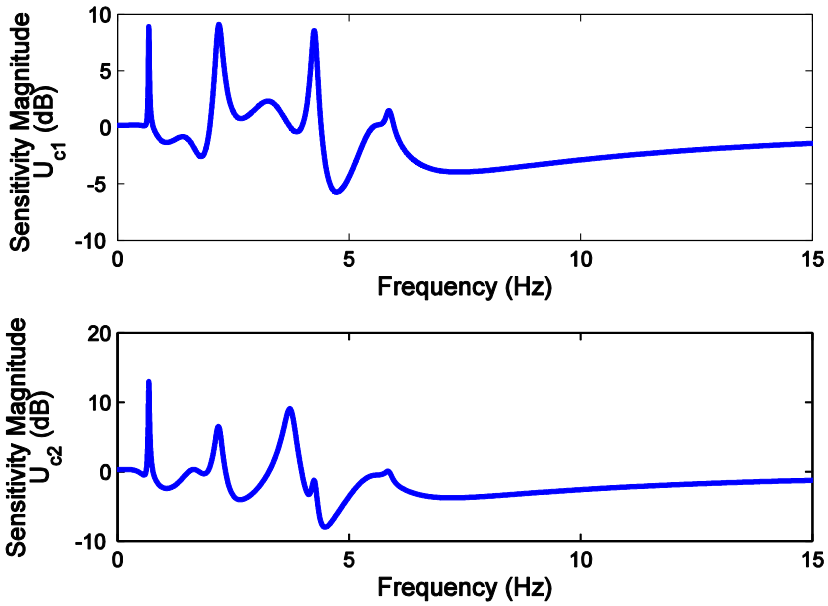

Figure 8.27: Sensitivity Transfer Functions Magnitude for Fully Decentralized Control Design.

8.6 Experimental Results

The control performance of the wired and wireless smart sensor controllers outlined in the previous sections is evaluated on the experimental setup in both the frequency and time domain. For evaluation, the controlled systems are subjected both to a band-limited white-noise input and earthquake loadings. The performance of all systems is compared using the same wired capacitive accelerometers manufactured by PCB Piezotronics. The accelerometers have a measurement range of ±3g, a frequency range of 0-100 Hz, and a sensitivity of 1V/g. In total, five systems are evaluated: uncontrolled, zeroed control, wired control, centralized wireless control, and fully decentralized wireless control.

The inner control loops for the shake table and AMD are implemented on dSpace model 1103; and the outer control systems are implemented on either the wireless smart sensors or dSpace as appropriate. The dSpace system is equipped with single-ended encoder inputs, 16-bit analog inputs, and 16-bit analog outputs alongside the digital signal processing board for control. For the wired control system, the control loop is executed in dSpace at 1000 Hz using the approach given in Figure 8.28. A discrete-time equivalent of the LQG control design is created with a Tustin transformation to better approximate the continuous-time system. Any distortion should not be significant due to the high sampling rate. For the wireless control systems, the digital conversion of the acceleration measurements, control processing, and analog output of the command displacement is completed onboard the wireless sensor nodes (WSN) similar to Figure 7.11. The command displacement from the WSN is processed by dSpace to determine the command voltage based on the PD cart control. In the fully decentralized wireless system, the acceleration is measured with the onboard accelerometer. Figure 8.29 shows a decentralized control node deployed on the structure. The SHM-SAR Rev. 2.0 and SHM-D2A are stacked on the Imote2. The USB connection provides a consistent source of power and the cable from the SHM-D2A carries the command displacement output to dSpace.

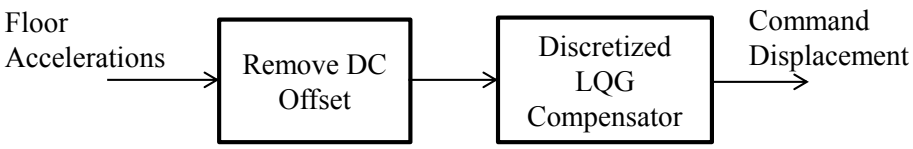

Figure 8.28: Wired Control Implementation within dSpace.

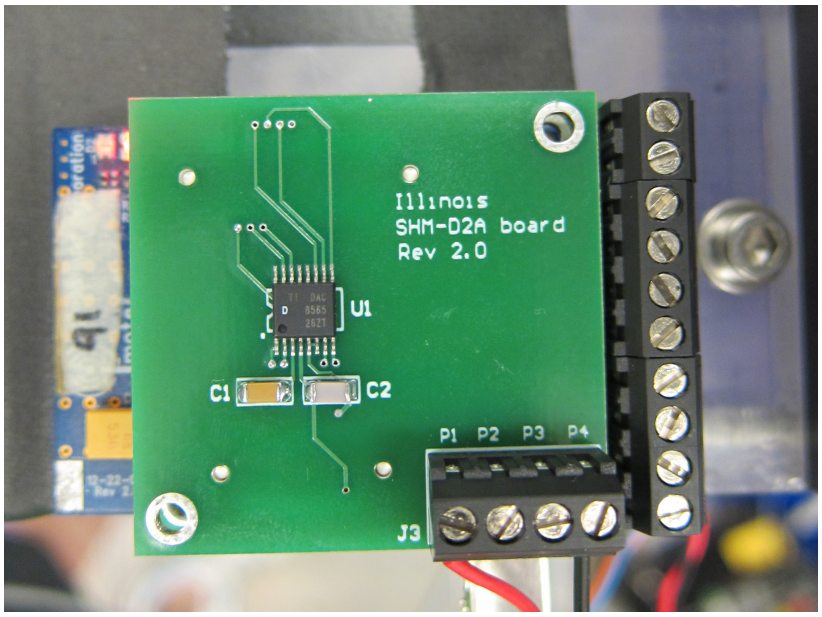

Figure 8.29: Decentralized Control Leaf Node on Experiment Structure.

Prior to closed-loop testing, the loop gain transfer functions are determined experimentally and compared with the analytical results to verify the closed-loop system model and the experimental setup. To determine the open loop response, a band-limited white noise is input to one AMD at a time and the calculated control commands are measured. Examples of the experimentally obtained loop gains for the wired, centralized, and fully decentralized system are plotted in Figure 8.30 (a)-(c), respectively. Overall, the experimental and analytical results match well, so the closed-loop system model used in design is satisfactory. The wireless centralized loop gain shows there is significantly more noise in the system due to the aliasing present from the slow sampling rate and data loss from communication. However, the overall behavior matches the analytical system. On the other hand, the wireless fully decentralized experimental loop gain matches the analytical results very closely. Thus, the lack of any data loss and the faster sampling rate for fully decentralized control significantly lowers the noise in the system.

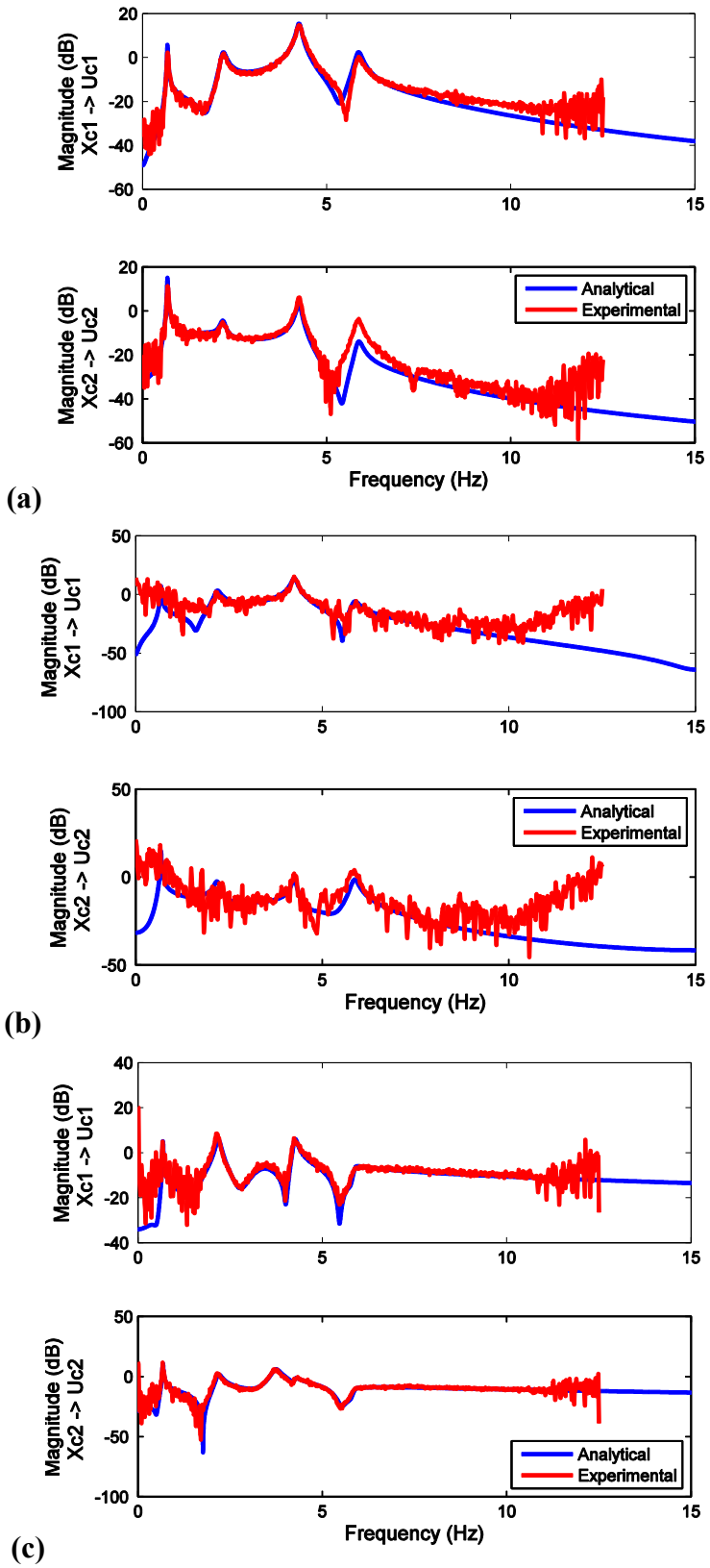

Figure 8.30: Experimental Loop Gain Comparisons for (a) Wired, (b) Centralized, and (c) Fully-Decentralized Control Systems.

8.6.1 Frequency Domain Performance

The closed loop system is excited by a band-limited white-noise ground excitation from 0 to 10 Hz to determine the response reduction at the natural frequencies of the structure. The uncontrolled and zeroed responses are determined as well for comparison. In zeroed control, a zero command is applied to the AMDs; by zeroing the AMDs, there will be additional damping in the system when compared to completely uncontrolled. The transfer functions from the acceleration response of each story to the ground acceleration are presented in Figure 8.31. The ratio of the peak response at the first natural frequency and the rms response compared to the uncontrolled system is provided in Table 8.5.

All of the control systems reduce both the peak responses and the rms responses of the structure. As expected, the additional damping of the zero control reduces the peak response of the first natural frequency by about 50%; the reduction in the overall rms response is more modest. The feedback controllers significantly outperform the zeroed control in reducing the peak response at the first natural frequency of the system and also further reduce the rms response. Therefore, the active control systems successfully improve the performance of the structure in the frequency domain.

The three feedback controller systems offer a similar reduction of the first mode response but differ in their overall performance. In Figure 8.31, the reduction at the first natural frequency does not appear as significant as other modes, but this performance is good given the limited stroke of the AMDs. On the other hand, the wired and decentralized controllers offer better overall performance than the centralized wireless system. In the frequency domain, the centralized controller flattens the response by lowering the response at the higher natural frequencies but slightly raises the response at other frequencies. The wired and decentralized control result in similar reductions in the rms response, except at the first story due to the contribution of the third mode. Overall, however, the decentralized wireless control system results in comparable performance to the tethered system.

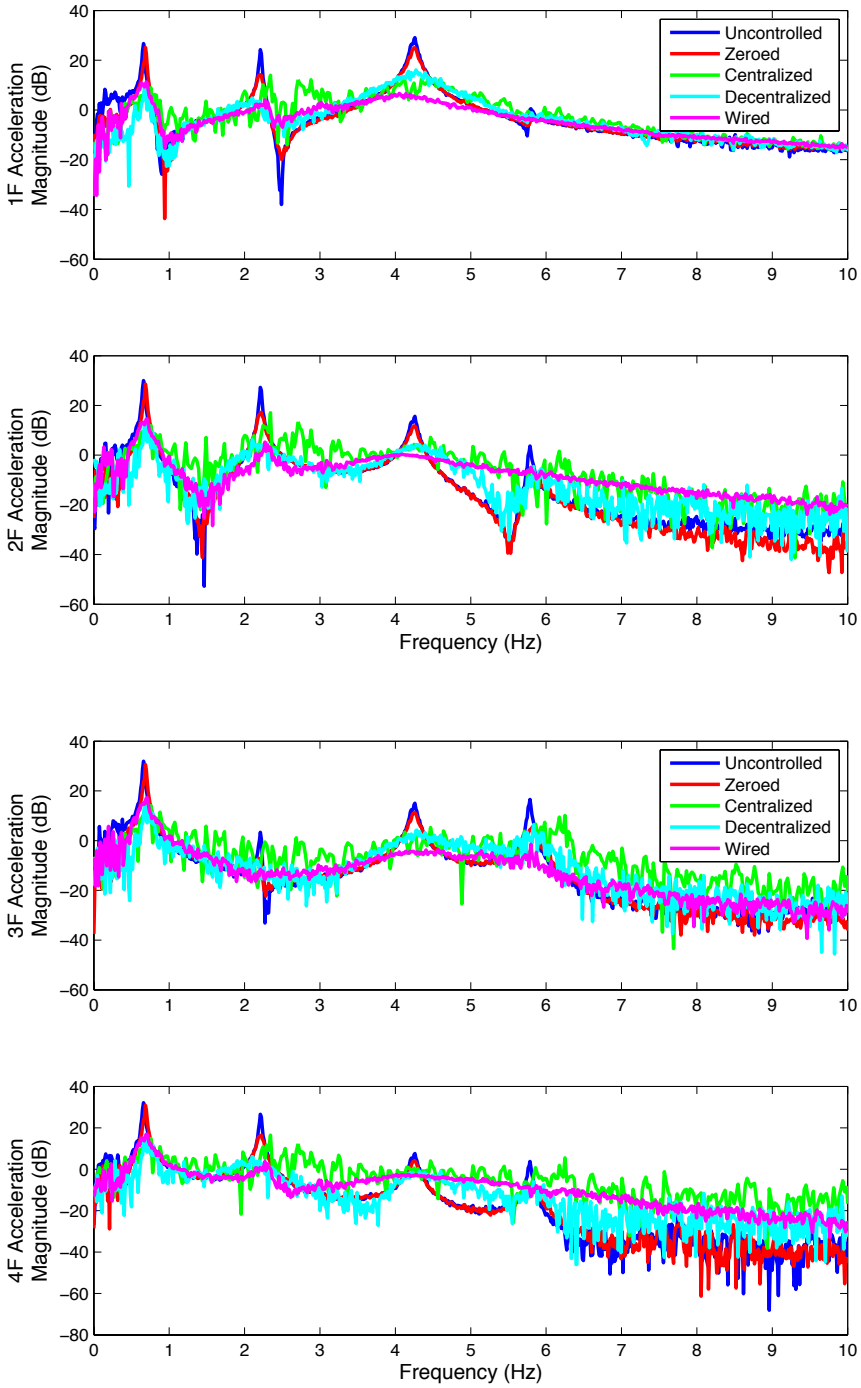

Figure 8.31: Transfer Functions of All Controllers from Ground Acceleration to Structural Responses

Table 8.5: Reductions in Frequency Domain Response of All Controllers Compared to Uncontrolled Response

Controller	1st Floor Acceleration	2nd Floor Accelerations	3rd Floor Acceleration	4th Floor Acceleration
(a) ratio of peak responses at 1st natural frequency to uncontrolled responses				
Zeroed	0.55	0.53	0.52	0.52
Wired	0.17	0.16	0.17	0.15
Centralized	0.19	0.18	0.16	0.18
Decentralized	0.17	0.17	0.16	0.17
(b) ratio of RMS responses to uncontrolled responses				
Zeroed	0.76	0.75	0.84	0.79
Wired	0.29	0.34	0.37	0.34
Centralized	0.64	0.68	0.56	0.62
Decentralized	0.46	0.28	0.28	0.25

8.6.2 Seismic Excitation Response

A set of earthquake records is used to evaluate the time domain performance of the control systems. The four seismic excitations are:

- El Centro: El Centro Array #9, Imperial Valley, CA (1940)
- Kobe: KJMA Station (1995)
- Chi Chi: Station CHY006 (1999)
- Northridge: Castaic Old Ridge Rt Station (1994)

The records, gathered from the PEER ground motion database (http://peer.berkeley.edu), are not time-scaled for the setup, because the first natural frequency of the structure lies within the region of peak demand of the earthquakes. However, the earthquake records are linearly scaled so the PGA is feasible for the small-scale experimental setup.

For accurate reproduction by the shake table, each earthquake record undergoes transfer function iteration to determine the appropriate displacement command for the table controller (Spencer and Yang 1998). The experimental transfer function for the shake table from the displacement command to the measured acceleration is used to determine a shake table model. The identified 3-pole, 3-zero model is:

$$H(s) = \frac{s^2(s+16.18)}{(s+860.9)^2(s+8.57)} \tag{8.8}$$

The zeros at the origin are shifted slightly prior to inverting the model for transfer function iteration to limit the large low-frequency component in the displacement command. Transfer function iteration is conducted offline to determine the displacement commands for each earthquake record (Spencer and Yang 1998). The comparison of the table produced and desired acceleration in Figure 8.32 shows some overshoot of the desired acceleration and reflects some

challenges reproducing small motions. These two limitations are likely due to the friction in the table bearings. However, overall, the shake table can successfully reproduce ground motions through transfer function iteration.

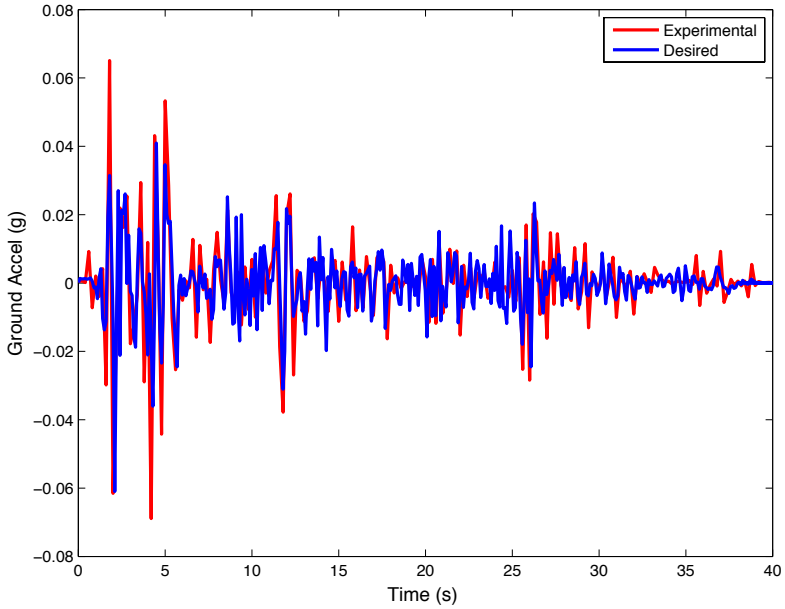

Figure 8.32: Comparison of Shake Table Generated Motion Compared to Desired for 0.2*El Centro.

The closed-loop responses of all five systems are compared for each earthquake excitation in Figure 8.33 (a) – (d). The majority of the response occurs during the initial impulse of the earthquake and eventually undergoes free vibration. In general, all the controllers limit the response during the free vibration period; however, the response during the peak motion varies widely between controller and earthquake excitation. Table 8.6 and Table 8.7 present the ratio of the peak response and rms response to the uncontrolled for each story acceleration under each ground motion. In general, the wired control system offers the best control performance in both the peak and rms response. However, the decentralized wireless control system is similar, particularly for the El Centro and Northridge ground excitations.

The two levels of decentralization of the wireless control systems present very different control performance. Despite having more knowledge of the system response, the centralized control system is less effective and uses more control effort. The centralized controller has difficulty reducing the response during the initial impulse but reduces the overall rms response of the structure. This behavior can mostly be attributed to the low sampling rate and the additional noise due to aliasing. Although some data loss occurs during control, the data loss in this experimental setup is very small. In addition, both wireless systems have more trouble with the Chi Chi and Kobe ground motions, because of the more cyclic impulsive load and saturation of the SHM-SAR measurements. However, the fully decentralized wireless control system still results in good overall performance despite the lack of global knowledge of the system response.

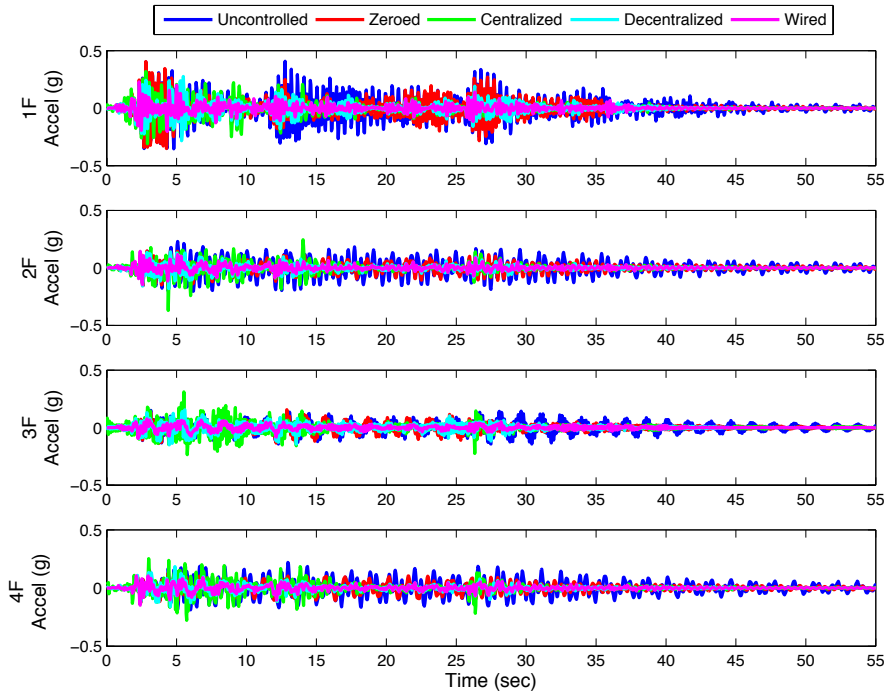

(a)

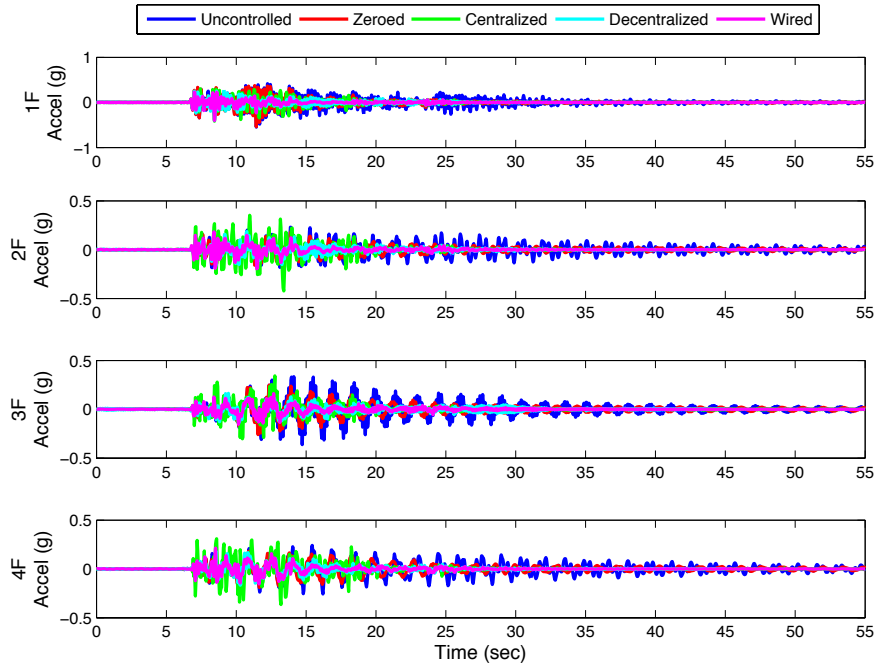

(b)

Figure 8.33: Acceleration Responses of All Control Systems Subjected to Seismic Motions: (a) 0.2*El Centro, (b) 0.2*Northridge, (c) 0.3*Chi Chi and (d) 0.1*Kobe.

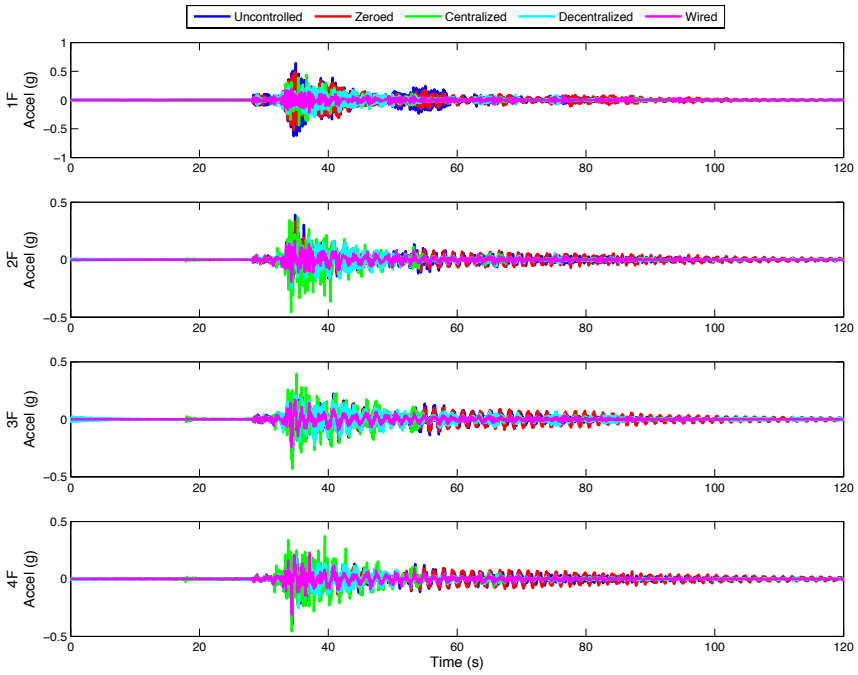

(c)

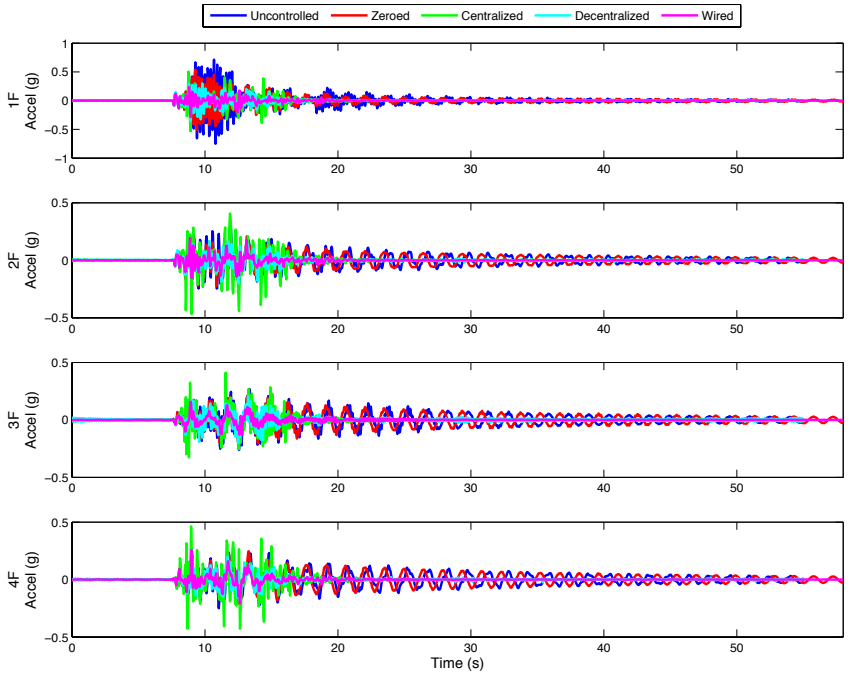

(d)

Figure 8.33 (cont.).

Table 8.6: Ratio of Peak Responses to Uncontrolled for Each Ground Excitation.

Controller	1st Floor Acceleration	2nd Floor Acceleration	3rd Floor Acceleration	4th Floor Acceleration
(a) Ratio of Peak Response to Uncontrolled for 0.2*El Centro Ground Excitation				
Zeroed	0.99	0.67	1.04	0.70
Wired	0.56	0.64	0.63	0.67
Centralized	0.78	1.61	2.07	1.26
Decentralized	0.70	0.79	1.03	0.84
(b) Ratio of Peak Response to Uncontrolled for 0.2*Northridge Ground Excitation				
Zeroed	0.98	0.91	0.72	0.74
Wired	0.73	0.85	0.45	0.83
Centralized	0.76	1.84	0.95	1.42
Decentralized	0.72	0.81	0.45	0.71
(c) Ratio of Peak Response to Uncontrolled for 0.3*Chi Chi Ground Excitation				
Zeroed	0.82	0.85	0.95	0.90
Wired	0.34	0.50	0.87	0.78
Centralized	0.69	1.17	1.56	1.15
Decentralized	0.46	0.63	0.81	0.77
(d) Ratio of Peak Response to Uncontrolled for 0.1*Kobe Ground Excitation				
Zeroed	0.72	0.74	0.79	0.99
Wired	0.38	0.65	0.60	1.02
Centralized	0.71	1.56	1.54	1.84
Decentralized	0.47	0.67	0.77	0.85

Table 8.7: Ratio of RMS Response to Uncontrolled for Each Ground Excitation.

Controller	1st Floor Acceleration	2nd Floor Acceleration	3rd Floor Acceleration	4th Floor Acceleration	AMD-1 Command (m)	AMD-2 Command (m)
(a) Ratio of RMS Response to Uncontrolled for 0.2*El Centro Ground Excitation						
Zeroed	0.76	0.58	0.77	0.61	--	--
Wired	0.32	0.30	0.38	0.31	0.0050	0.0096
Centralized	0.53	0.59	0.89	0.64	0.0138	0.0170
Decentralized	0.53	0.42	0.70	0.41	0.0070	0.0080
(b) Ratio of RMS Response to Uncontrolled for 0.2*Northridge Ground Excitation						
Zeroed	0.78	0.69	0.67	0.73	--	--
Wired	0.35	0.43	0.34	0.41	0.0074	0.015
Centralized	0.63	0.97	0.64	0.87	0.017	0.022
Decentralized	0.51	0.51	0.44	0.48	0.011	0.013
(c) Ratio of RMS Response to Uncontrolled for 0.3*Chi Chi Ground Excitation						
Zeroed	0.83	0.87	1.04	0.98	--	--
Wired	0.32	0.52	0.57	0.59	0.0049	0.0145
Centralized	0.60	1.18	1.22	1.14	0.014	0.019
Decentralized	0.56	0.76	0.93	0.77	0.0069	0.0082
(b) Ratio of RMS Response to Uncontrolled for 0.1*Kobe Ground Excitation						
Zeroed	0.67	0.84	0.92	0.93	--	--
Wired	0.23	0.37	0.32	0.36	0.0056	0.0110
Centralized	0.53	1.07	0.76	0.95	0.0136	0.0160
Decentralized	0.39	0.52	0.54	0.50	0.0082	0.0102

8.6.3 Robustness of Fully Decentralized System to Leaf Node Failure

One distinct advantage of the fully decentralized control system is the robustness to node or sensor failure. To evaluate the robustness, the performance of the decentralized control system when a leaf node fails is compared with the original fully decentralized wireless system. Two failure cases are considered under the Northridge ground motion:

- The leaf node on the fourth story fails at the peak response and only AMD-1 is available.
- The leaf node on the second story fail at the peak response and only AMD-2 is available.

Failure of the leaf node is approximated in the experiment by zeroing the control to the respective AMD at the specified time of failure.

In both cases, the decentralized control system is still able to reduce the response of the structure and no instability results (Figure 8.34). As expected, the failure of the fourth-story AMD results in poorer performance, because AMD-2 is essential for limiting the first mode response. On the other hand, Table 8.8 indicates that failure of the leaf node on the second story results in comparable rms performance to the original system; although, the loss of AMD-1 does

result in larger peak responses. Therefore, decentralized wireless control can be a good and robust option for active structural control.

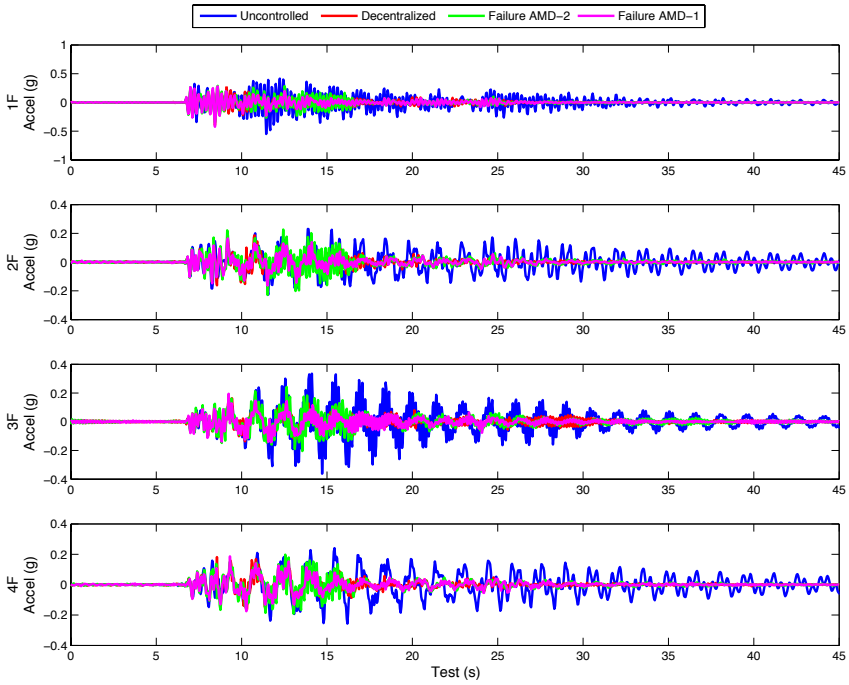

Figure 8.34: Acceleration Responses for Decentralized Control Systems When a Controller Node Fails under 0.2*Northridge Excitation.

Table 8.8: Summary of Response Ratios when a Decentralized Control Leaf Node Fails.

Controller	1st Floor Acceleration	2nd Floor Acceleration	3rd Floor Acceleration	4th Floor Acceleration	AMD-1 Command (m)	AMD-2 Command (m)
(a) Ratio of Peak Response to Uncontrolled for 0.2*Northridge Ground Excitation						
Zeroed	0.98	0.91	0.72	0.74	--	--
Decentralized	0.72	0.81	0.45	0.71	--	--
AMD-1Fail	0.77	0.71	0.54	0.73	--	--
AMD-2 Fail	0.63	0.99	0.67	0.77	--	--
(b) Ratio of RMS Response to Uncontrolled for 0.2*Northridge Ground Excitation						
Zeroed	0.78	0.69	0.67	0.73	--	--
Decentralized	0.51	0.51	0.44	0.48	0.011	0.013
AMD-1Fail	0.50	0.47	0.43	0.47	0.010	0.0129
AMD-2 Fail	0.61	0.67	0.58	0.59	0.012	0.012

8.7 Summary

A four-story, small-scale structure suitable for different levels of control decentralization is used to evaluate two wireless active control systems. A high-fidelity MIMO model of the system that accounts for control structure interaction is formed from three SIMO models and used subsequently in control design. The wireless control designs are based on the control implementations presented in Chapter 6; due to the larger number of states in the system, the fully decentralized system operates at 725 Hz and centralized system runs at 30 Hz. The two wireless control systems are successfully implemented on the experimental structure. Despite the lack of complete knowledge of the system response, the fully decentralized control system outperforms the centralized wireless system in both the frequency and time domain due to the faster sampling rate and lack of data loss. The fully decentralized system also offers comparable performance to the wired system and robustness during node failure.

Chapter 9

CONCLUSIONS AND FUTURE RESEARCH

9.1 Conclusions

This research presents a wireless smart sensor solution for active control of civil systems that has been successfully used on an experimental test structure. The hardware and software designed and produced overcomes the practical challenges for wireless active control, including time delay, data loss, and real-time performance. The LQG control design approaches addressed discrete-time control systems with internal delays, slow sampling rates, or lack of system knowledge. The designed wireless control system offered excellent performance on a four-story base-excited structure controlled with two active mass dampers. The successful implementation of the wireless system for active control highlights the potential of wireless smart sensors for a variety of control applications.

A thorough background of structural control has been provided, focusing in particular on systems that address the practical challenges of control including sensor failure, time-delay, and low sampling rates. Previous wireless control systems have focused on semi-active control, where smart sensor performance is not as much of a concern due to their inherent stability. These experimental applications present a good first step toward addressing and identifying the challenges of wireless structural control. Modern control theory as well as the wireless smart sensor platform and software framework that are at the core of the work are presented as necessary background for the successful design, production, and implementation of the wireless control system.

Low-latency data acquisition and actuation hardware tailored for control applications has been designed and implemented on the Imote2 smart sensor platform. Prior to development, the limitations of data acquisition hardware tailored for SHM are presented; the oversampling and digital filtering used to improve the resolution introduces significant latency into the system. Through the use of an SAR-type analog-to-digital converter and careful design of the corresponding driver, the latency due to the hardware alone is almost negligible. An onboard accelerometer further simplifies acceleration feedback for control. The control loop is completed with an actuation interface that complements the performance of the data acquisition hardware.

Real-time wireless data acquisition is essential for feedback control; however, application is not straightforward due to inherent challenges of the embedded software and the smart sensor platform. The application framework accounts for the single-threaded operating system and communication latency by using a tightly timed approach and a TDMA communication protocol that accounts for the sensing/processing time and the number of nodes in the network. The performance of the application highlights the challenge of centralized control and the tradeoff between the number of nodes in the network and the maximum possible sampling rate. The framework is extended for near real-time, high-throughput applications that require large network sizes and high sampling rates.

The application framework and insights gained from real-time data acquisition are extended in the implementation of fully decentralized and centralized control strategies on the Imote2 fitted with low-latency hardware. In fully decentralized control, sensing, control calculations, and actuation all occur on each leaf node. The tight timing, alarm based approach, and powerful onboard processing capabilities preserve computational accuracy while operating

at a very high sampling rate. The sampling rate achieved is significantly higher than previous implementations of fully decentralized control. The framework is then combined with real-time wireless data acquisition for centralized control. The application design limits data loss while preserving sampling rates adequate for control of most civil systems.

The wireless control system was applied to a small-scale single-degree-of-freedom structure with an active control system to evaluate the performance of the complete system in comparison to a wired control implementation. An approach for discrete-time control design that accounts for slow sampling rates and an input delay is used for the smart sensor control designs. By taking account of the discrete-time nature of the control system and the input delay in the design, the stability and performance of the closed-loop system can be preserved. The low-latency wireless control system outperforms the original data acquisition hardware tailored for SHM and offers comparable performance to the wired control system.

The centralized and fully decentralized wireless control systems are compared using a four-story experimental structure suitable for different levels of decentralization. Two active mass dampers are used for control of the structure; by tuning the PD control system for each AMD, the control modes can be adjusted to improve the performance. The non-parametric model of the MIMO system identified experimentally captures the control structure interaction of the two AMDs and the shake table for use in the control designs. The fully decentralized controller consists of two independent subsystems that are designed separately to reduce the acceleration response of the complete structure. Because only the stability of each subsystem is guaranteed, care was taken to ensure global stability of the controlled system. Despite the lack of complete system knowledge, the decentralized wireless control system outperformed the centralized wireless system under both a BLWN input and earthquake excitations. The additional response knowledge in the centralized system does not overcome the limitations of centralized wireless control: the slower sampling rate, a higher noise level due to aliasing, and the occasional loss of data. Furthermore, the decentralized wireless control system offered comparable performance to the wired system in the frequency domain and in the RMS response under earthquake excitations.

One distinct advantage of decentralized control systems is their robustness to sensor failure. To evaluate the robustness of the fully decentralized wireless system, failure of a subsystem controller was enforced during the application of an earthquake ground motion. The decentralized control system was able to reproduce the RMS control performance of the original, intact system. Because wireless control systems are well suited to decentralized control strategies, these results highlight the promise of wireless smart sensors for control over traditional tethered systems.

9.2 Future Research Directions

This research has addressed many of the challenges for wireless control of civil systems including latency, sampling rate performance, and discrete control design at slower sampling rates. The results encourage many new avenues of research, which will be discussed below.

- Partially decentralized wireless control. The four-story actively controlled structure highlighted the performance advantage of fully decentralized wireless control despite the lack of complete knowledge of the system. Partially decentralized wireless control systems will likely offer a balance of system knowledge and sampling rate to further

improve the control performance. The flexibility of the wireless control implementation on the Imote2 will simplify the application of different levels of decentralization.

- Hierarchically decentralized wireless control. Hierarchical control systems offer a higher level of control that can be used to ensure concordant behavior of control subsystems and modify the controller under different conditions. The hierarchical systems, popular in autonomous control applications, have yet to be applied to structural control; however, the onboard processing and wireless communication capabilities of smart sensor platforms make this control architecture more attractive.

- Lower noise, low-latency data acquisition hardware. One limitation of low-latency data acquisition is the aliasing of noise at slower sampling rates. An easily modified anti-aliasing filter that does not introduce significant delay would improve the performance of the hardware while still making them feasible for control applications.

- Event based structural control. Control techniques that do not require tight timing or a consistent sampling rate have not been applied to structural control systems because they typically used for much longer time scales. Wireless smart sensors are well suited for this control approach, because maintaining real-time performance continues to be a challenge on wireless smart sensor platforms.

- Multi-tasking wireless sensor networks. As wireless smart sensor networks become more common for structural or environmental monitoring, they could be leveraged for more than one application to improve the overall performance of the system. For example, an SHM deployment could be used for control under extreme events and long-term monitoring otherwise. A smart sensor network that is tailored for multiple tasks is not trivial due to the conflicting performance requirements of these systems.

- Application of wireless control to energy harvesting systems. Feedback of environmental conditions and the state of the energy harvesting system (i.e. wind turbines) may be used to optimize the energy output. The low cost of deployment and ability to interface with a variety of sensors make wireless control networks appealing for these typically large-scale systems.

REFERENCES

Agrawal, A. K., and Yang, J. N. (2000). Compensation of time-delay for control of civil engineering structures. *Earthquake Engineering & Structural Dynamics*, 29(1), 37-62.

Analog Devices, Inc. (2008). "16-bit, 4-Channel/8-Channel, 250 kSPS PulSAR ADC Rev.B." Norwood, MA.

Antsaklis, P.J and Passino, K.M. (1993). *An Introduction to Intelligent and Autonomous Control.* Kluwer Academic Publishers, Massachusetts.

Battaini, M., Yang, G., and Spencer Jr., B.F. (2000). Bench-Scale Experiment for Structural Control. *Journal of Engineering Mechanics*, 136(2): 140-148.

Bryson, A.E. (2002). *Applied Linear Optimal Control: Examples and Algorithms*. Cambridge, United Kingdom: Cambridge University Press.

Casciati, F., and Rossi, R. (2003). Fuzzy Chip Controllers and Wireless Links in Smart Structures. *Proceedings of the AMAS/ECCOMAS/STC Workshop on Smart Materials and Structures (SMART '03)*, Warsaw, Poland.

Casciati, S., and Chen, ZC. (2012). An Active Mass Damper System for Structural Control Using Real-Time Wireless Sensors. *Structural Control and Health Monitoring*. DOI: 10.1002/stc:1485.

Chang, C.-M., & Spencer, Jr., B. F. (2012). "Multi-axial Active Isolation for Seismic Protection of Buildings". *Newmark Structural Engineering Laboratory Report Series*, Vol. 30, University of Illinois at Urbana-Champaign, Illinois. http://hdl.handle.net/2142/30839.

Chu, S.Y., Soong, T.T., Lin, C.C., and Chen, Y.Z. (2002). Time-delay effect and compensation on direct output feedback controlled mass damper systems. *Earthquake Engineering and Structural Dynamics*, 31: 121-137. DOI: 10.1002/eqe.101

Chu, S.Y., Soong, T.T., and Reinhorn, A.M. (2005). *Active, Hybrid, and Semi-active Structural Control: A Design and Implementation Handbook*. West Sussex, England: John Wiley & Sons.

Chung, L. L., Lin, C. C., and Lu, K. H. (1995). Time-delay control of structures. *Earthquake Engineering & Structural Dynamics*, 24(5), 687-701. doi:10.1002/eqe.4290240506

Dyke, S.J., Spencer, B.F., Quast, P., and Sain, M.K. (1995). Role of Control-Structure Interaction in Protective System Design. *Journal of Engineering Mechanics*, 121(2): 322-338.

Dyke, S. J., Spencer Jr, B.F., Quast, P., Kaspari Jr, D.C., and Sain, M.K. (1996). Implementation of an Active Mass Driver Using Acceleration Feedback Control. *Microcomputers in Civil Engineering*, 11: 305-323.

Eker, J., Cervin, A., and Hörjel, A. (2001). Distributed Wireless Control Using Bluetooth. *In Proceedings of IFAC Conference on New Technologies for Computer Control*. Hong Kong, P.R. China.

Franklin, G., Powell, J., and Workman, M. (1998). *Digital Control of Dynamic Systems*. Third Edition. California: Ellis-Kagle Press.

Galbreath, J.H., Townsend, C.P., Mundell, S.W., Hamel, M.J., Esser, B., Huston, D., and Arms, S.W. (2003). Civil Structure Strain Monitoring with Power-efficient, High-speed Wireless Sensor Networks. *Proceedings of the 4th International Workshop on Structural Health Monitoring*, Stanford, CA, 1215-1222.

Gobriel, S., Mosse, D., and Cleric, R. (2009). TDMA-ASAP: Sensor Network TDMA Scheduling with Adaptive Slot-Stealing and Parallelism. *Proceedings of the 29th International Conference on Distributed Computing Systems (ICDCS'09)*. IEEE, Montreal, QC, 458-465.

Guenther, O., Hogg, T. and Huberman, B.A. (1997). Controls for Unstable Structures. *Proc. Of SPIE Conference on Mathematics and Control in Smart Structures*, March, 754-763.

Hirata, H., and Powell, J.D. (1990). Sample Rate Effects on Disturbance Rejection for Digital Control Systems. *Proceedings of American Controls Conference*, San Diego, CA, 1137-1145.

Hogg, T., and Huberman, B. A. (1998). Controlling smart matter. *Smart Materials and Structures*, 7(1), 1-14. doi:10.1088/0964-1726/7/1/001

Housner, G. W., Bergman, L. A., Caughey, T. K., Chassiakos, A. G., Claus, R. O., Masri, S. F., Skelton, R. E., Soong, T. T., Spencer, B. F., and Yao, J. T. P. (1997). "Structural Control: Past, Present, and Future." *Journal of Engineering* Mechanics, 123(9): 897-972. doi:10.1061/(ASCE)0733-9399(1997)123:9(897).

Jang, S. and Rice, J. (2009). "Calibration Guide for Wireless Smart Sensors. Illinois Structural Health Monitoring Project." http://shm.cs.uiuc.edu/files/docs/CalibrationGuide.pdf (last accessed April 16, 2012).

Jo, H., Sim, SH., Mechitov, K.A., Kim, R., Li, J., Moinzadeh, P., Spencer Jr., B.F., Park, J.W., Cho, S., Jung, H-J, Yun, C-B, Rice, J.A., and Nagayama, T. (2011). Hybrid Wireless Smart Sensor Network for Full-scale Structural Health Monitoring of a Cable-stayed Bridge. *SPIE Conference*, San Diego, CA: 6-10.

Kawka, P.A., and Alleyne, A.G. (2005). Stability and feedback control of wireless networked systems. *In Proceedings of the 2005 American Control Conference*, Portland, OR: IEEE 2953-2959. doi:10.1109/ACC.2005.1470423.

Kim, S.B., Spencer Jr, B.F., Yun, C-B. (2005). Frequency Domain Identification of Multi-Input, Multi-Output Systems Considering Physical Relationship between Measured Variables. *Journal of Enginering Mechanics*, 131(5), 461-472. doi:10.1061/(ASCE)0733-9399(2005)131:5(461)

Kurata N, Kobori T, Takahashi M, Niwa N, Midorikawa H. (1999). Actual seismic response controlled building with semi-active damper system. *Earthquake Engineering and Structural Dynamics*, 28(11):1427–1447.

Kwakernaak, H. and Silvan, R. (1972). *Linear Optimal Control Systems*. New York: Wiley-Interscience.

Lei, Y., Wu, D. T., and Lin, Y. (2012). A Decentralized Control Algorithm for Large-Scale Building Structures. *Computer-Aided Civil and Infrastructure Engineering*, 27, 2-13. doi:10.1111/j.1467-8667.2010.00707.x

Lewis, F. (1986). *Optimal Estimation: with an Introduction to Stochastic Control Theory*. New York: Wiley-Interscience.

Levis, P., Madden, S., Polastre, J., Szewczyk, R., Woo, A., Gay, D., Hill, J., Welsh, M., Brewer, E., and Culler, D. (2005). "TinyOS : An Operating System for Sensor Networks." *Ambient Intelligence*, ed. Werner Weber, Jan M. Rabaey, and Emile Aarts, 115-147. Springer, Berlin, Heidelberg.

Li, J., Nagayama, T., Mechitov, K. A., and Spencer, Jr., B. F. (2012). Efficient campaign-type structural health monitoring using wireless smart sensors. *Proceedings of SPIE* (Vol. 8345). San Diego, CA, USA. doi:10.1117/12.914860

Loh, C.H., Lynch, J.P., Lu, K.C., Wang, Y., Chang, C.M., Lin, P.Y., and Yeh, T.H. (2007). Experimental verification of a wireless sensing and control system for structural control using MR dampers. *Earthquake Engineering & Structural Dynamics*, 36(3): 1303-1328.

Loh, C.H., and Chang, C.M. (2008). Application of Centralized and Decentralized Control to Building Structure : Analytical Study. *Journal of Engineering* Mechanics, 134(11): 970-982.

Lunze, J. (1992). *Feedback Control of Large-Scale Systems*. New York: Prentice Hall.

Lynch, J.P., and Law, K.H. (2002a). Decentralized Control Techniques for Large-Scale Civil Structural Systems. *Proceedings of the 20th International Modal Analysis Conference (IMAC XX)*, Los Angeles, CA.

Lynch, J. P., & Law, K. H. (2002b). Market-based control of linear structural systems. *Earthquake Engineering & Structural Dynamics*, 31, 1855-1877. doi:10.1002/eqe.193

Lynch, J. P., and Law, K. H. (2004). Decentralized energy market-based structural control. *Structural Engineering and Mechanics*, 17 (3-4): 1-16.

Lynch, J.P., Sundararajan, A., Law, K.H., Sohn, J., and Farrar, C.G. (2004a). Design of a Wireless Active Sensing Unit for Structural Health Monitoring. *Proceedings of SPIE 11th Annual International Symposium on Smart Structures and Materials*, San Diego, CA, USA.

Lynch, J.P., Sundararajan, A., Law, K.H., Kiremidjian, A.S., and Carryer, E. (2004b). Embedding damage detection algorithms in a wireless sensing unit for operational power efficiency. *Smart Materials and Structures*, 13(4), 800-810. DOI:10.1088/0964-1726/13/4/018.

Lynch, J.P. and Loh, K. (2006). A summary review of wireless sensors and sensor networks for structural health monitoring. *Shock and Vibration*, 38(2), 91-128.

Lynch, J. P., Wang, Y., Swartz, R. A., Lu, K. C., and Loh, C. H. (2008). Implementation of a closed-loop structural control system using wireless sensor networks. *Structural Control and Health Monitoring*, 15(4): 518–539.

Ma, T.-W., Xu, N.-S., and Tang, Y. (2008). Decentralized Robust Control of Building Structures Under Seismic Excitations. *Earthquake Engineering and Structural Dynamics*, 37, 121-140. doi:10.1002/eqe

Maróti, M., Kusy, B., Simon, G., and Lédeczi, A. (2004). The Flooding Time Synchronization Protocol. *Proceedings of SenSys* , Baltimore, MD, 39-49.

Maxim Integrated Products. (2001). "Understanding SAR ADCs: Their Architecture and Comparison with Other ADCs." Application Note 1080. www.maxim-ic.com/an1080 (last accessed January 5, 2012).

Miller, T.I., Spencer Jr, B.F., Li, J., and Jo, H. (2010). "Solar Energy Harvesting and Software Enhancements for Autonomous Wireless Smart Sensor Networks." *Newmark Structural Engineering Laboratory Report Series* No. 022, University of Illinois at Urbana-Champaign, Illinois. (Available at http://hdl.handle.net/2142/16300)

Moinzadeh, P., Mechitov, K., Shiftehfar, R., Abdelzaher, T., Agha, G., and Spencer Jr, B.F. (2012). The Time-Keeping Anomaly of Energy-Saving Sensors: Manifestation, Solution, and a Structural Monitoring Case Study. *IEEE Communications Society Conference on Sensor, Mesh and Ad Hoc Communications and Networks (SECON).*

Nagayama, T., Sim, S.-H., Miyamori, Y., and Spencer Jr, B.F. (2007). Issues in Structural Health Monitoring Employing Smart Sensors. *Smart Structures and Systems*, 3(3), 299-320.

Nagayama, T., Spencer Jr., B. F., Mechitov, K. A, and Agha, G. A. (2009). Middleware services for structural health monitoring using smart sensors. *Smart Structures and Systems* 5(2), 119–137.

Niu, J., Deng, Z., Zhou, F., Cao, Z., Lui, Z., and Zhu, F. (2009). A Structural Health Monitoring System Using Wireless Sensor Network. *Wireless Communications, Networking and Mobile Computing; WiCom '09, 5th International Conference*, Beijing, China. doi: 10.1109/WICOM.2009.5302988

Paek, J., Gnawali, O., Jang, K., Nishimura, D., Govindan, R., Caffrey, J., Wahbeh, M., and Masri, S. (2006). A Programmable Wireless Sensing System for Structural Monitoring. *4th World Conference On Structural Control and Monitoring*, San Diego, CA.

PCB Piezotronics, Inc. (2013). Depew, NY. (http://www.pcb.com/)

Pelgrom, M. J. M. (2010). *Analog-to-Digital Conversion*. Dordrecht: Springer Netherlands. doi:10.1007/978-90-481-8888-8

Poplys, N.J., Kawka, P.A., and Alleyne, A.G. (2004). Closed-Loop Control over Wireless Networks. *IEEE Control Systems Magazine*. June, 58-71.

Quickfilter Technologies. (2007). "QF4A512: 4-Channel Programmable Signal Converter (PSC) Datasheet." www.quickfiltertech.com/files/QF4A512%20Data%20Sheet.pdf (last accessed December 19, 2011).

Rice, J.A. and Spencer Jr., B.F. (2009). "Flexible Smart Sensor Framework for Autonomous Full-scale Structural Health Monitoring" *Newmark Structural Engineering Laboratory Report Series*, Vol. 18, University of Illinois at Urbana-Champaign, Illinois. http://hdl.handle.net/2142/13635.

Rice, J. A., Mechitov, K. A., Sim, S. H., Spencer Jr., B. F., and Agha, G. A.. (2010). Enabling framework for structural health monitoring using smart sensors. *Structural Control and Health Monitoring*. doi:10.1002/stc.386.

Sain, P. M., Spencer Jr, B. F., Sain, M. K., and Suhardjo, J. (1992). Structural Control Design in the Presence of Time Delays. *ASCE Engineering Mechanics Conference*; College Station, Texas: 812-815.

Sandell, N., Varaiya, P., Atahns, M., and Safonov, M. (1978). Survey of Decentralized Control Methods for Large Scale Systems. *IEEE Transactions on Automatic Control*. 23(2), 108-128.

Seth, S., Lynch, J.P., and Tilbury, D.M. (2005). Wirelessly networked distributed controllers for real-time control of civil structures. *Proceedings of the 2005 American Control Conference*, 2946-2952. doi:10.1109/ACC.2005.1470422.

Shankar PM. (2002). *Introduction to Wireless Systems*. Wiley and Sons: New York.

Soong, T.T. (1990). *Active Structural Control: Theory and Practice*. Essex, England: Longman Scientific & Technical.

Spectral Dynamics, Inc. (2007). San Jose, CA. (www.spectraldynamics.com)

Spencer, B.F., Jr., and Sain, M.K. (1997). Controlling buildings: a new frontier in feedback. *IEEE Control Systems* 17(6): 19–35.

Spencer, B. F., Jr., and Yang, G. (1998). "Earthquake simulator control by transfer function iteration." Proc. of the 12th ASCE Engineering Mechanics Conference, San Diego, CA.

Spencer, B. F., Dyke, S. J., and Deoskar, H. S. (1998a). Benchmark problems in structural control: part I—Active Mass Driver system. *Earthquake Engineering & Structural Dynamics* 27(11): 1127-1139.

Spencer, B. F., Dyke, S. J., and Deoskar, H. S. (1998b). Benchmark problems in structural control: part I—Active Tendon System. *Earthquake Engineering & Structural Dynamics* 27(11): 1141-1147.

Spencer, B.F, Christenson, R.E., and Dyke, S.J. (1999). Next Generation Control Problem for Seismically Excited Buildings. *Proceedings of the Second World Conference on Structural Control*, Kyoto, Japan. Vol. 2: 1351-1360.

Spencer Jr, B. F., and Nagarajaiah, S. (2003). State of the Art of Structural Control. *Journal of Structural Engineering*, 129 (7): 845-856. doi:0.1061/(ASCE)0733-9445(2003)129:7(845).

ST Microelectronics (2008). "LIS344ALH: MEMS inertial sensor high performance 3-axis ±2/±6g ultracompact linear accelerometer Rev. 3.0" Geneva, Switzerland.

Stengel, R.F. (1986). *Stochastic Optimal Control: Theory and Application*. New York: John Wiley & Sons.

Swartz, A., Jung, D., Lynch, J.P., Wang, Y., Shi, D., and Flynn, M.P. (2005). Design of a wireless sensor for scalable distributed in-network computation in a structural health monitoring system. *Proceedings 5th International Workshop on Structural Health Monitoring*, Stanford, CA.

Swartz, R. A, and Lynch, J. P. (2009). Strategic network utilization in a wireless structural control system for seismically excited structures. *Journal of Structural* Engineering, 135: 597-608.

Texas Instrument Inc. (2007). "DAC8565: 16-Bit, Quad Channel, Ultra-Low Glitch, Voltage Output Digital-to-Analog Converter with 2.5V, 2ppm/°C Internal Reference". Dallas, TX.

TinyOS, http://www.tinyos.net, (2006).

van Hoesel, L.F.W. and Havinga, P.J.M. (2004). A TDMA-based MAC protocol for WSNs. *Proceedings of the 2nd International Conference on Embedded Networked Sensor Systems (SenSys '04)*. ACM, New York, NY, USA.

Wang, Y., Swartz, R.A., Lynch, J.P., Law, K.H., Lu, K.-C., and Loh, C.-H. (2006a). Decentralized Civil Structural Control Using a Real-Time Wireless Sensing and Control System. *Proceedings of 4th World Conference on Structural Control and Monitoring*, San Diego, CA.

Wang, Y., Swartz, A., Lynch, J.P., Law, K.H., Lu, K.-C., and Loh, C.-H. (2006b). Wireless Feedback Structural Control with Embedded Computing. *Proceedings of SPIE 11th International Symposium on Nondestructive Evaluation for Health Monitoring and Diagnostics*, San Diego, CA, USA.

Wang, Y., Swartz, R. A., Lynch, J. P., Law, K. H., Lu, K. C., and Loh, C. H. (2007a). Decentralized civil structural control using real-time wireless sensing and embedded computing. *Smart Structures and Systems*, 3(3), 321-340.

Wang, Y., Lynch, J., and Law, K. A. (2007b). Wireless Structural Health Monitoring System with Multithreaded Sensing Devices: Design and Validation. *Structure & Infrastructure Engineering: Maintenance, Management, Life-Cycle Design & Performance*, 3(2), 103-120. DOI:10.1080/15732470600590820.

Wang, Y., Lynch, J.P., and Law, K.H. (2009). Decentralized H ∞ controller design for large-scale civil structures. *Earthquake Engineering and Structural Dynamics*, 38: 377-401. doi:10.1002/eqe.862

Wang, Y. (2011). Time-delayed dynamic output feedback H infinity controller design for civil structures: A decentralized approach through homotopic transformation. *Structural Control and Health Monitoring*, 18, 121-139. doi:10.1002/stc.344

Wang, Y., and Law, K.H. (2011). Structural Control with Multi-Subnet Wireless Sensing Feedback: Experimental Validation of Time-Delayed Decentralized H ∞ Control Design. *Advances in Structural Engineering*, 14(1): 25-39. doi:10.1260/1369-4332.14.1.25.

Whelan, M.J. and Janoyan, K.D. (2009). Design of a Robust, High-rate Wireless Sensor Network for Static and Dynamic Structural Monitoring. *Journal of Intelligent Material Systems and Structures*, 20(7): 849-863. DOI:10.1177/1045389X08098768.

Xu, B., Wu, Z.S., and Yokoyama, K. (2003). Neural Networks for Decentralized Control of Cable-Stayed Bridge. *Journal of Bridge Engineering*, 8(4), 229-236.

Yao, J.T.P. (1972). Concept of Structural Control. *Journal of Structural Division*, ASCE, 98(7) 1567-1574.

List of Recent NSEL Reports

No.	*Authors*	*Title*	*Date*
017	Borello, D.J., Denavit, M.D., and Hajjar, J.F.	Behavior of Bolted Steel Slip-critical Connections with Fillers	Aug. 2009
018	Rice, J.A. and Spencer, B.F.	Flexible Smart Sensor Framework for Autonomous Full-scale Structural Health Monitoring	Aug. 2009
019	Sim, S.-H. and Spencer, B.F.	Decentralized Strategies for Monitoring Structures using Wireless Smart Sensor Networks	Nov. 2009
020	Kim, J. and LaFave, J.M.	Joint Shear Behavior of Reinforced Concrete Beam-Column Connections subjected to Seismic Lateral Loading	Nov. 2009
021	Linderman, L.E., Rice, J.A., Barot, S., Spencer, B.F., and Bernhard, J.T.	Characterization of Wireless Smart Sensor Performance	Feb. 2010
.			
022	Miller, T.I. and Spencer, B.F.	Solar Energy Harvesting and Software Enhancements for Autonomous Wireless Smart Sensor Networks	March 2010
023	Denavit, M.D. and Hajjar, J.F.	Nonlinear Seismic Analysis of Circular Concrete-Filled Steel Tube Members and Frames	March 2010
024	Spencer, B.F. and Yun, C.-B. (Eds.)	Wireless Sensor Advances and Applications for Civil Infrastructure Monitoring	June 2010
025	Eatherton, M.R.. and Hajjar, J.F.	Large-Scale Cyclic and Hybrid Simulation Testing and Development of a Controlled-Rocking Steel Building System with Replaceable Fuses	Sept. 2010
026	Hall, K., Eatherton, M.R., and Hajjar, J.F.	Nonlinear Behavior of Controlled Rocking Steel-Framed Building Systems with Replaceable Energy Dissipating Fuses	Oct. 2010
027	Yeo, D. and Jones, N.P.	Computational Study on 3-D Aerodynamic Characteristics of Flow around a Yawed, Inclined, Circular Cylinder	Mar. 2011
028	Phillips, B.M. and Spencer, B.F.	Model-Based Servo-Hydraulic Control for Real-Time Hybrid Simulation	June 2011
029	Linderman, L.E., Mechitov, K.A., and Spencer, B.F.	Real-Time Wireless Data Acquisition for Structural Health Monitoring and Control	June 2011
030	Chang, C.-M. and Spencer, B.F.	Multi-axial Active Isolation for Seismic Protection of Buildings	May 2012
031	Phillips, B.M. and Spencer, B.F.	Model-Based Framework for Real-Time Dynamic Structural Performance Evaluation	August 2012
032	Moreu, F. and LaFave, J.M.	Current Research Topics: Railroad Bridges and Structural Engineering	October 2012
033	Linderman, L.E., Spencer, B.F.	Smart Wireless Control of Civil Structures	January 2014